"There are no facts,
only interpretations."
-Nietzche

Dedicated to Luigi and my family.
Love passionately,
Live fully and
Learn courageously!

OXIDATION OF A SEGREGATED MoN LAYER GROWN ON Fe(100)-3.5wt%Mo-N

By

ROCHELLE CONRADIE

This thesis is submitted in accordance with the requirements for the degree

Magister Scientiae

In the Faculty Natural and Agricultural Sciences

Department of Physics

at the

University of the Free State

Bloemfontein

Study leader: Dr. W.D. Roos
Co-study leader: Prof. H.C. Swart

Submitted : 29 June 2001

Acknowledgements

The author wishes to express her gratitude and special thanks to the following people:

- The Creator of all, for science, life and love
- My parents and brother for everlasting love and support. Thank you for giving me the opportunity to study and for encouraging me when things were tough.
- Luigi, for showing me the other side of the coin. Thank you for being real and the man I love.
- Beth, for laughs, tears, and friendship.
- A special word of thanks to my study leaders from whom I have learned so much.
- All my colleagues at the department and especially Koos Terblans for helping me fix the unfixable.
- The department instrumentation and electronics for their assistance.
- Mrs. C.L. Conradie for the proof reading and editing.
- To SAM for behaving.

TABLE OF CONTENTS

Chapter 1

Introduction

1.1. Background 1

1.2. Molybdenum 1

1.3. Literature survey 2

1.4. Motivations and objectives 3

1.5. Layout of the thesis 4

Chapter 2

Oxidation Theory

2.1. Introduction 5

2.2. Definition 6

2.3. Mechanisms of oxidation 6

2.3.1. Adsorption 8

2.3.1.1. Surface reactions 8

2.3.1.2. A simple model of adsorption 10

2.3.1.3. Origin of the binding energy 10

2.3.1.4. Physisorption versus Chemisorption 12

2.3.1.5. Kinetics of adsorption 14

2.3.2. Nucleation 18

2.3.3. Rate of lateral growth 20

2.3.4. Thickening of the oxide layer 22

2.4. Fe oxidation 26

2.5. Mo oxidation 27

2.6. Fe and Mo in catalysts 28

Chapter 3

Experimental set-up and procedure

3.1. Introduction 29

3.2. Apparatus 30

3.2.1. Vacuum chamber 30

3.2.2. AES System 30

3.2.3. Control Unit Settings 33

3.2.4. Heater unit 34

3.2.5. Samples 35

3.3. Experimental procedure 35

3.3.1. Sample preparation in vacuum 35

3.3.2. Preparation of the enriched Mo-N layer 36

3.3.3. A typical oxidation run 37

3.3.4. Depth profiling 38

3.3.5. Partial pressure measurements 38

3.3.6. Desorption studies 39

3.4. Computer Controls 40

3.4.1. Software upgrades 40

Chapter 4

Mathematical Analysis

4.1. Introduction 42

4.2. The Auger yield 42

4.3. The inelastic mean free path, λ 43

4.4. The backscattering term, r_m 44

4.5. Linear Least Squares fit 46

4.6. Determining the thickness 47

4.6.1. Oxide thickness of the Fe based specimen 48

4.6.2. Evaluating the expressions for the oxide thickness 49

4.7. Data processing procedure 51

Chapter 5

Experimental results and discussion

5.1. Introduction 52

5.2. Fe(100) oxygen exposures 52

5.2.1. Room temperature oxygen exposure 52

5.2.2. Oxygen exposure of Fe(100) at various temperatures 57

5.2.3. A summary of the oxidation behaviour of Fe(100) 61

5.3. Mo(100) oxygen exposures 62

5.4. Fe(100)-3.5wt% Mo-N oxygen exposure 64

5.4.1. Room temperature oxygen exposure 64

5.4.2. Oxygen exposure at various temperatures 67

5.4.3. A summary of the Fe(100)-3.5wt% Mo-N oxidation behaviour 71

5.5. The oxygen exposure of the segregated MoN layer 72

5.5.1. LTR segregation of Mo and N 72

5.5.2. Oxygen exposure at various temperatures 74

5.5.3. Room temperature oxygen exposure 78

5.5.4. A summary of the oxidation behaviour of the segregated MoN layer on the Fe(100)-3.5wt% Mo-N sample 85

5.6. Summary of the room temperature exposures 86

Chapter 6

Mathematical analysis of experimental results

6.1. Introduction 87

6.2. Linear Least Squares Method 87

6.2.1. Fe(100) 88

6.2.2. Fe(100)-3.5wt% Mo-N 91

6.2.3. Segregated MoN layer on the Fe(100)-3.5wt% Mo-N 94

6.2.4. Comparison 99

6.3. Thickness calculations 100

6.3.1. Segregated MoN layer on Fe(100)-3.5wt% Mo-N 100

6.3.2. Fe(100)-3.5wt% Mo-N 104

6.3.3. Fe(100) 106

6.4. The sticking coefficient 107
6.5. Summary 108

Chapter 7
Summary and Conclusions
7.1. Summary 110
7.2. Future work 111
7.3. Research presentations 112

Bibliography 114

Summary

The oxidation behaviour of the segregated MoN layer on the Fe(100)-3.5wt% Mo-N substrate was investigated in this study. Previous studies suggested the synergetic segregation of the Mo and N from the Fe(100)-3.5wt% Mo-N specimen. It has also been shown that the segregated Mo and N form a MoN surface compound. As an alloy element in stainless steels, the Mo aids in the inhibition of the oxidation and thus prevents corrosion.

Auger electron spectroscopy (AES) was used to obtain the experimental results. For this study the oxidation of a Fe(100) specimen and a Fe(100)-3.5wt% Mo-N specimen were investigated to establish a point of reference to describe the oxidation behaviour of the segregated MoN layer. Linear temperature ramping was used to segregate the Mo and N from the Fe(100)-3.5wt% Mo-N specimen. The specimens were exposed to an oxygen environment at various temperatures. The partial pressure of the oxygen was monitored with a mass spectrometer and was kept constant at 2×10^{-10} torr. The Auger peak-to-peak heights for the relevant elements in the specimens were measured as a function of the exposure time.

Upon oxidation, the low energy Fe AES peak (47 eV) undergoes shape changes. The iron oxide has a dual peak with 42 eV and 52 eV kinetic energy respectively. The Fe(100) specimen surface reacted rapidly with the oxygen environment at room temperature to form an iron oxide, as depicted by the change in the low energy Fe AES peak. The exposures performed at 100°C and 200°C also resulted in oxide formation although the extent of the oxidation decreased with an increase in the temperature. Above 300°C there was no oxide formation detected and therefore there is only oxygen adsorption at these temperatures. The Fe(100)-3.5wt% Mo-N specimen showed similar oxidation behaviour as was seen for the Fe(100) specimen. At room temperature the surface of the specimen reacted rapidly with the oxygen environment to form an iron oxide. There was no

indication of the Mo and N reacting with the oxygen environment. At 100°C and 200°C less oxide formation was detected and above 300°C there was only oxygen adsorption. The segregated MoN layer had a markedly different response to the oxygen exposure. The oxygen exposure performed at room temperature had a strikingly different course of the O Auger peak-to-peak height increase compared to that of the Fe(100) and Fe(100)-3.5wt% Mo-N specimens exposure at the same temperature. The segregated MoN layer retards the surface reaction. A hypothesis formulated describes the MoN layer as a perforated layer that has some Fe exposed. The oxygen reacts rapidly with the exposed Fe. Longer exposures result in the dissociation of the MoN layer and the desorption of the MoO_3 and N_xO_y compounds from the surface. Once the layer has dissociated completely the Fe will continue to react as for the other specimens. Oxidation occurs up to 300°C and at higher temperatures no oxide formation is detected.

The changes in the low energy Fe AES peak are used to calculate the fraction oxide and metal contributing to the peak by using the Linear Least Squares method. The low energy Fe AES peak cannot be used for thickness calculations as it is subject to the backscattering term. The experimental data suggests that the backscattering term is a function of the exposure time. A first approximation is to assume a linear change with time. This approximation was applied successfully to the room temperature oxidation of the segregated MoN layer, but the same function could not be applied to the other two specimens.

The thickness of the oxide was calculated using the change in the high energy Fe AES peak intensity. The O_2 sticking coefficient for the exposure of the Fe(100) and the exposure of the segregated layer was also calculated and the differences in the values were attributed to the effect of the dissociation of the MoN layer on the adsorption of the O_2 on the specimen surface.

Opsomming

Die oksidasie gedrag van die gesegregeerde MoN laag op die Fe(100)-3.5wt% Mo-N substraat is in hierdie studie bestudeer. Vorige studies het voorgestel dat daar ko-segregasie van die Mo en N in die Fe(100)-3.5wt% Mo-N monster plaasvind. Dit is ook voorgestel dat die gesegregeerde Mo en N 'n MoN oppervlakverbinding vorm. As 'n allooi element in vlekvrye staal help die Mo die vertraging van die oksidasie van die staal en verhoed dus korrosie.

Augerelektronspektroskopie (AES) is aangewend in hierdie studie om die eksperimentele data te verkry. Die oksidasie van 'n Fe(100) monster en 'n Fe(100)-3.5wt% Mo-N monster is bestudeer en aangewend as 'n verwyingspunt om die oksidasie gedrag van die gesegregeerde MoN laag te beskryf. Linêere temperatuur verhoging is gebruik om die Mo en N uit die Fe(100)-3.5wt% Mo-N monster te segregeer. Die monsters is blootgestel aan 'n suurstof atmosfeer by verskeie temperature. Die parsiële druk van die suurstof is met 'n massa spektrometer gemonitor en konstant gehou by 'n druk van 2×10^{-10} torr. Die Auger piek-tot-piek hoogtes van die relevante elemente in die monsters is gemeet as 'n funksie van die blootstellings tyd.

Die vorm van die lae energie Fe AES piek (47 eV) verander wanneer die Fe chemies reageer met die suurstof. Die oksied het 'n duale piek by 42 eV en 52 eV onderskeidelik. Die Fe(100) monster oppervlak reageer vinnig met die suurstof atmosfeer by kamer temperatuur om 'n ysteroksied te vorm soos aangedui in die verandering in die lae energie Fe AES piekvorm. Alhoewel daar oksied vormasie by 100°C en 200°C is neem die graad van oksidasie af met 'n toename in die temperatuur. Bo 300°C is daar geen oksied vormasie waargeneem nie en by hierdie temperature is daar slegs suurstof adsorpsie. Die Fe(100)-3.5wt% Mo-N monster het soortgelyke oksidasie gedrag getoon as die Fe(100) monster. By kamer temperatuur reageer die oppervlak vinnig met die

suurstof atmosfeer om 'n ysteroksied te vorm. Daar was geen teken dat die Mo an N met die suusrtof atmosfeer reageer nie. By 100°C en 200°C is daar minder oksied vormasie waargeneem en bo 300°C was daar slegs suurstof adsorpsie. Die gesegregeerde MoN laag het 'n wesenlike verskil in oksidasie gedrag getoon. By kamertemperatuur het die O Auger piek-tot-piek hoogte 'n merkwaardige verskil in verloop getoon i.v.m. die Fe(100) en Fe(100)-3.5wt% Mo-N monsters se O verloop by dieselfde temperatuur. Die gesegregeerde laag vertraag die oppervlak reaksie. 'n Hipotese is geformuleer om die gedrag te beskryf. Die hipotese lees dat die gesegregeerde MoN laag geperforeer is en dat daar steeds 'n bietjie Fe blootgestel is. Die suurstof reageer vinnig met die blootgestelde Fe. Verdere blootstelling lei tot die dissosiasie van die MoN laag en die desorpsie van N_xO_y en MoO_3 verbindings vanaf die oppervlak. Wanneer die gesegregeerde laag heeltemal gedissosieer en gedesorbeer het reageer die Fe in die monster met die suurstof atmosfeer soos vir die ander monsters. Oksidasie is waargeneem tot by 300°C en geen oksied vormasie is waargeneem by hoër temperature nie.

Die verandering in die lae energie Fe AES piek word aangewend om die fraksie oksied en metaal te bereken wat bydrae tot die gemete AES piek d.m.v. kleinste kwadraat passings. Die lae energie Fe AES piek kan nie suksesvol aangewend word vir die berekening van die oksiedlaag dikte nie aangesien dit afhanklik is van die terugverstrooiingsfaktor. Die eksperimentele data dui aan dat die terugverstrooiingsfaktor 'n funksie is van die blootstellings tyd. As 'n eerste benadering word aangeneem dat die verandering in die terugverstrooiingsfaktor lineêr is met tyd. Die korreksie kan suksesvol aangewend word vir die kamertemperatuur oksidasie van die gesegregeerde MoN laag, maar dieselfde redenasie is nie geldig vir die oksiedasie van die ander monsters nie.

Die dikte van die oksied is bereken deur die verandering in die piek intensiteit van die hoë energie Fe AES piek. Die O_2 kleefkoeffiënt vir die suurstof blootstelling van die Fe(!00) monster en die gesegregeerde laag is bereken en die verskille in die waardes is toegeskryf aan die invloed van die dissosiasie van die MoN laag op die adsorpsie van die O_2 op die oppervlak van die monsters.

Chapter 1
Introduction

1.1. Background

The new millennium is presenting many challenges for researchers. The world's quest for bigger, better and more affordable materials has opened many doorways to exciting research opportunities. The experimental techniques used in surface science studies have undergone continuous upgrading and, with more precise experimental data, scientists are able to see surface reactions in a new light. The importance of alloying in material design is undeniable and the far-reaching effect of segregation on the material's properties is still an ever-growing field of research.

Iron (Fe) alloys are the most popular alloys in use today. The relative low cost of Fe and the availability of the ore have added to the popularity of the materials. Many different elements are used as alloy elements in the Fe based alloys such as chromium (Cr), nickel (Ni), phosphor (P), molybdenum (Mo) and many more. Although much is known about Fe, the element Mo is relatively unfamiliar.

1.2. Molybdenum

Carl Wilhelm Scheele first positively identified molybdenum in 1778. In the 19^{th} century, the element was mainly used in laboratory research. In 1891, the French company Schneider & Co. used Mo as an alloy element in the manufacturing of armour plate. The scientists quickly noted the similarities between tungsten and Mo.

During World War I the demand for tungsten rose and the supply of the element became depleted. Mo was successfully used as a substitute for the tungsten. An intensive search for Mo deposits was initiated. By the end of the war, research began to find civilian

applications for Mo. It was widely used in automotive and structural steels. The research in Mo was continued and the diversity of the metal has made it invaluable. Today Mo is used in a number of applications ranging from use in stainless steels, superalloys, nickel based alloys, lubricants, chemicals and even electronics.

1.3. Literature survey

The segregation of Mo and the effect of N on this segregation in Fe-3.5wt%Mo was the subject of a study done by E. C. Viljoen and C. Uebing [1]. It was reported that there was strong synergetic segregation of the Mo and N. The segregation was more prominent for the (100) crystal orientation and the segregated layer was a stable epitaxially grown MoN surface compound.

A closer investigation of the segregation of Mo and N in the Fe(100)-3.5wt% Mo-N system was performed by B. Eltester and C. Uebing [2]. This study supported the synergetic effect between the Mo and N for segregation between 500 and 790 °C. Ar^+ depth profiling was used to determine the thickness of the MoN surface layer. According to the researchers the surface compound consisted of approximately two compound layers. It was also reported that the layer was a two-dimensional MoN surface compound and the formation of three-dimensional precipitates had been ruled out.

Baraldi et al [3] determined the structure of the two-dimensional MoN surface compound formed via the synergetic segregation of Mo and N from the Fe(100)-3.5wt% Mo-N single crystal using X-ray photoelectron diffraction. This study confirmed the formation of the two-dimensional epitaxially grown MoN surface compound. The compound was reported to consist of two Mo layers and a single N layer.

The effect of the N on the segregation of the Mo in the Fe(100)-3.5wt% Mo-N single crystal was re-evaluated by Viljoen et al [4]. This study reported that the presence of N only slightly enhanced the segregation of the Mo. The study also revealed that the presence of N on the sample surface is not a prerequisite for Mo segregation.

The oxygen adsorption on a MoN pre-covered Fe(100)-3.5wt% Mo-N single crystal in a temperature range of 400°C to 550°C was investigated by Hille et al [5]. It was suggested that the O atoms replace the N atoms on the sample surface. After the initial exchange process had been completed the surface phase consisted of $(Mo_xFe_{1-x})(O_yN_{1-y})$.

Apart from the segregation of Mo and N, Mo_xN_y compounds have also successfully been formed using chemical vapour deposition [6], ion beam assisted deposition [7] and through the chemical reduction of Mo-oxides [8].

The influence of Mo on the oxidation behaviour of Fe-24Cr-11Mo was the subject of a study performed by Mathieu et al [9]. The study involved the in situ oxidation of the sample at 384°C. It was found that the Mo decreased the rate of oxidation through barrier formation. A Mo rich layer formed at the metal-oxide interface, which acted as the barrier.

1.4. Motivations and objectives

It is a well-known fact amongst surface scientists that even small changes on the surfaces of single crystals can alter the properties of the sample.

The aim of this study was to investigate the oxidation behaviour of the segregated Mo-N layer on a Fe(100)-3.5wt% Mo-N single crystal.

The influence of the segregated Mo-N is described by comparison of the oxidation of a clean Fe(100) single crystal and the oxidation of a Fe(100)-3.5wt% Mo-N alloy single crystal. These comparisons will also give an indication of the influence of the alloy elements on the sample's oxidation behaviour.

Mathematical analysis of the oxidation of the samples is done to determine the thickness of the oxide layer formation on the samples. These values in turn are used to determine the diffusion coefficient involved in the formation of the surface oxide.

1.5. Layout of the thesis

Chapter 2 of the thesis focuses on the theory involved in this study. The fundamental concepts of oxidation are discussed in detail. The role of adsorption as a key step in the oxidation process is specifically addressed.

The experimental set-up and procedures is discussed in Chapter 3. The specific experimental conditions used in this study determine the data obtained, the processing of the information and the interpretations.

The formulae used in the data processing are discussed in Chapter 4. The assumptions made in the derivations of the formulae influence the conclusions made and may in some cases lead to deceptive results that could be misinterpreted.

The results are shown and discussed in Chapter 5. The influence of temperature, alloying and the segregation of MoN on the oxidation behaviour of Fe(100) are also shown.

Chapter 6 contains the calculated data from the formulae given in chapter 4. These results are used in the conclusions summarised in chapter 7.

Chapter 2

Oxidation Theory

2.1. Introduction

During the course of the past few decades surface science has grown to a large and very important field of study. Through specialization and the advancement in experimental techniques different fields under the umbrella of surface science have been established. One topic found in most of the sub-fields of surface science is the study of adsorption on metals. Adsorption is the first step in the growth of oriented thin films and also the first step in oxidation. The presence of adsorbed species can strongly influence many physical properties of surfaces. It is thus important to understand this process in order to better understand the mechanism and rate of oxidation.

Oxidation has a significant effect on the world of science and engineering. It is the cause of extensive deterioration and corrosion in many materials. Industries have invested considerably in research on protective coatings and alloy developments in order to increase the life span of many pipes and other components. The effects of oxidation are also felt in other areas such as microelectronics, chemistry and even in pharmacology. Most metals undergo oxidation although the degree of corrosion varies greatly. The rate at which different metals oxidise and the properties of the oxide that forms also varies tremendously. These differences have been applied with great success to the development of alloys with specific resistance to corrosion through oxidation, for example the wide range of stainless steels currently available. Oxidation, however, also has positive applications. In many processes, it is necessary to pacify a surface; oxidation of the surface renders it less reactive, i.e. it has been pacified.

This study focuses on the oxidation of different samples. It is thus important to understand the fundamental concepts involved in oxidation and also the difference between adsorption and oxidation. In this chapter the fundamental principles of adsorption as the first step in oxidation and the theory of oxidation will be discussed.

2.2. Definition

Oxidation can simply be defined as the combination of any substance with oxygen [10]. However, the term oxidation is also used to describe the reactions between metals and an atom or a molecular group where the metal loses electrons. A metal is also oxidised and loses electrons when it goes from one valency to a higher one. The term oxidation therefore describes the transfer of electrons and thus the reactions involving oxygen combining with metals form only a small section under the term oxidation. The primary driving force for a metal or alloy to oxidise arises from the fundamental principle of nature to be in the state of lowest energy as allowed by the boundary conditions of the prevailing system. This study focuses on the reactions of different metals with oxygen, therefore when referring to oxidation the reaction with oxygen is implied. Before the rate of oxidation can be described, it is necessary to consider the mechanism by which oxidation takes place.

2.3. Mechanisms of oxidation

The reaction of a metal with oxygen can be broken down to *four main* stages illustrated in Figure 2.1 [11]:

a) There is a relatively fast *physisorption* of oxygen molecules on the surface of the sample. This is followed by the dissociation of the molecule and subsequent chemisorption will follow. These reactions are relatively fast.

b) The reactivity of the oxygen decreases, as there is a saturation of chemisorbed oxygen on the surface. For heterogeneous oxidation this stage is characterised by the formation of nuclei or oxide islands.

c) The nuclei or islands continue to grow with an almost steady increase in oxygen. This stage is therefore characterised by the lateral growth in the oxide islands.

d) Once the islands have grown so that they completely cover the surface, the oxide will slowly increase in thickness. The characteristics of the metal and of the oxide layer will determine the rate at which the oxide layer thickness will increase.

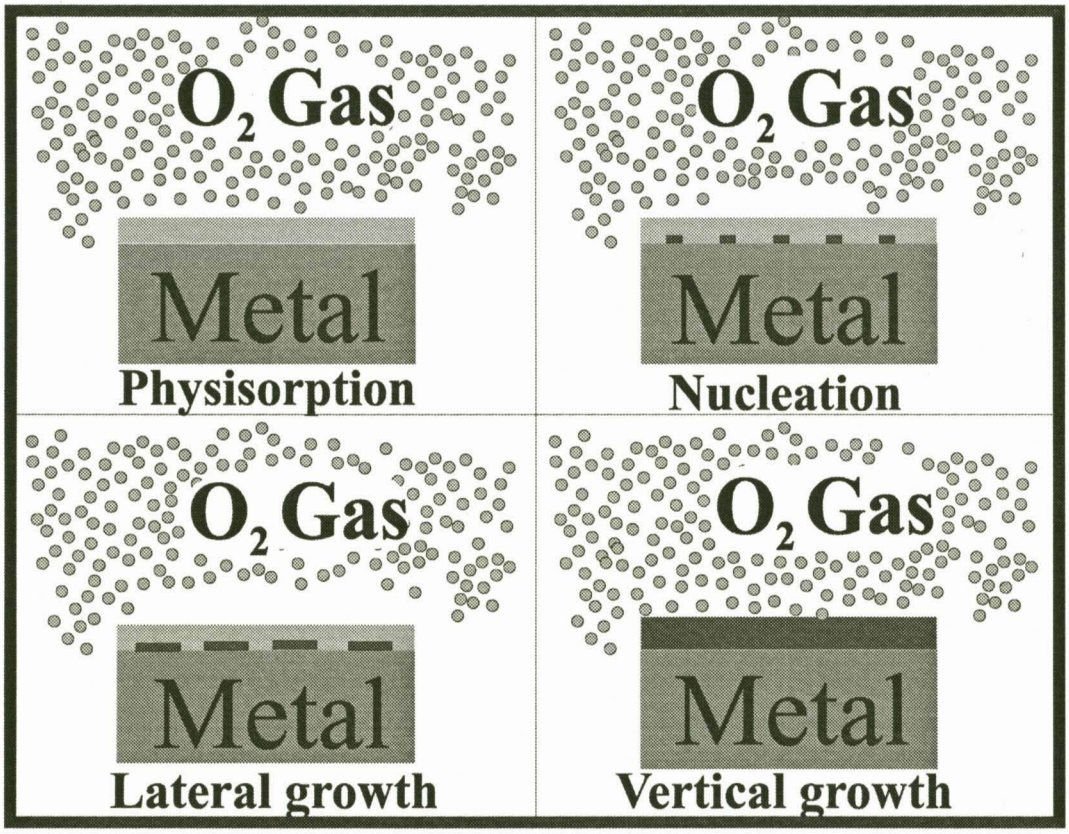

Figure 2.1: The four main stages of oxidation [12]

A distinction between these different stages is only possible when working with metals with low reactivity. For metals with higher reactivity, the first three stages occur too rapidly to resolve.

Each of the four stages contributes to the rate at which the oxidation takes place and must therefore be considered individually in order to determine the overall rate of the oxidation.

2.3.1. Adsorption

Adsorption is the first step in oxidation and therefore the mechanism by which the adsorption takes place and the rate of adsorption will influence the initial rate and mechanism of oxidation. Adsorption is closely related to the surface properties of the sample and the temperature.

2.3.1.1. Surface reactions

Adsorption can simply be defined as the accumulation or condensation of gas molecules on the surface of a material [13]. Another author defines adsorption as the process in which a substance (gas, liquid, or solid) is held on the surface of a solid [14].

When a metal surface is exposed to a gas, there are several processes involved. The various processes are illustrated in Figure 2.2. The gas molecules collide with the surface and these collisions have a number of possible outcomes [15]:

1. The molecule rebounds from the surface after an elastic collision where there is no exchange of energy or after an inelastic collision where there is some exchange of energy
2. Adsorption of the molecule could take place. Dependent upon the binding energy involved two types of adsorption are defined
    a) Physical adsorption (Physisorption): Physisorption is used to describe situations where the bonding between the adsorbed specie and the surface is principally due to dispersive interactions – the term Van der Waals adsorption is also frequently used in these cases. The heat of physisorption is less than 25 kJ/mole.

b) Chemical adsorption (Chemisorption): The energy associated with chemisorption is higher than 209 kJ/mole [10]. The heat of chemisorption is comparable to the energies involved in the formation of normal chemical bonds. Chemisorption is thus used to describe cases where there is strong ionic or covalent bonding between the adsorbate and the surface.

3. There could be a reaction on the surface. The incoming adsorbent specie could simply decompose or may interact with molecules already adsorbed on the surface.
4. The adsorbed species may desorb from the surface or may induce the desorption of other species on the surface. The chemical reaction that takes place on the surface may also result in the formation of a volatile substance that also desorbs from the surface.

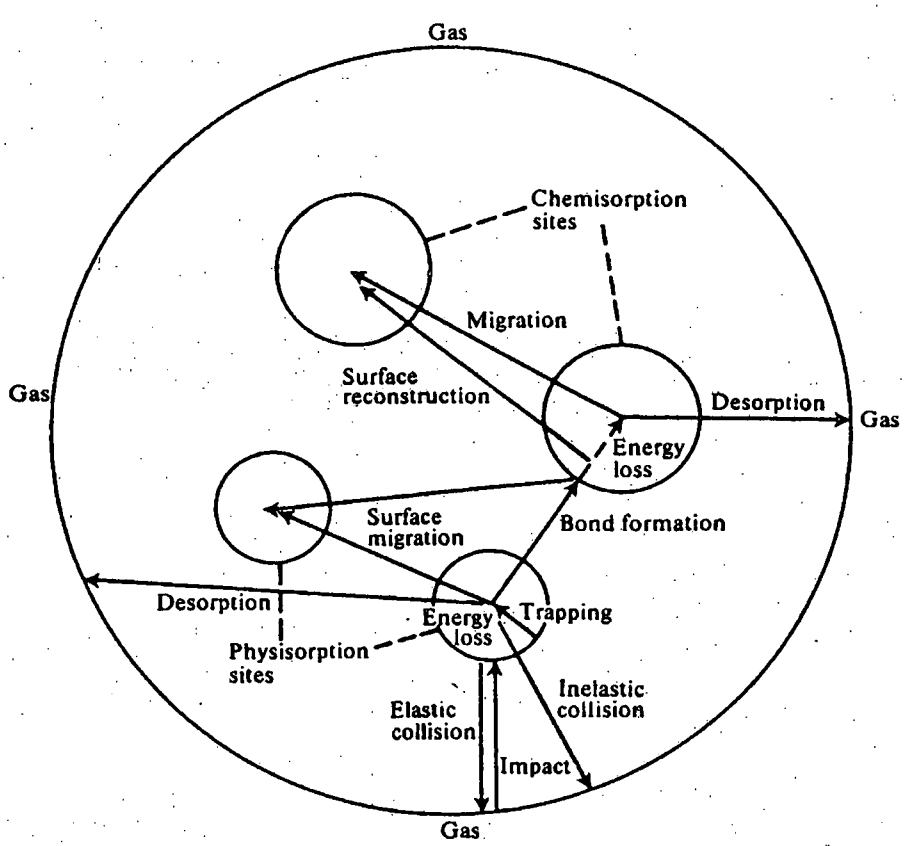

Figure 2.2: A schematic representation of surface processes. The circles represent potential energy wells. The well for the chemisorption is much deeper than the well for the physisorption.

2.3.1.2. A simple model of adsorption

The simplest situation in adsorption is that of a single atom interaction with a crystal surface [16]. As the adsorbate atom approaches the surface the electronic distribution of the atom and of the crystal surface will change. This may result in binding of the atom to the crystal and the creation of an additional surface dipole. A new set of electron energy levels can be defined for this system. This information can be used to determine the binding energy involved and the new wave functions to describe the charge distribution and the change in dipole of the surface. As the coverage increases there may be significant interactions within the adsorbed layer. These interactions will lead to changes with coverage of the average binding energy and dipole moment associated with each adsorbed atom. The nature of the interactions and the mobility of the adsorbate on the surface will determine whether the adsorption takes place heterogeneously with the formation of islands (or nuclei) with well-defined structure or simply occur uniformly over the entire surface.

The more active sites on the surface of the transition metals, the higher the electric field associated with the surface [17]. When a molecule is physically adsorbed in the vicinity of an active site, the electric field causes polarisation of the adsorbed molecule. The molecule undergoes reorientation in the field in such a way as to favour dissociation of the molecule. The molecule dissociates into individual atoms, ions, or radicals that have higher reactivity at the surfaces. The bonds formed in this case are much stronger and this process is defined as chemisorption.

2.3.1.3. Origin of the binding energy

A diatomic molecule free from constraints has six degrees of freedom, three vibrational, two rotational and one from the vibration of the nuclei [18]. When in the adsorbed state the molecules will execute only vibrational motion. Thus, the molecular rotations will be

quenched to some extent. The molar entropy associated with the adsorbed state will be less than that of the gaseous state. For adsorption to occur spontaneously there must be a reduction of internal energy or there must be a binding energy associated with the adsorbed state.

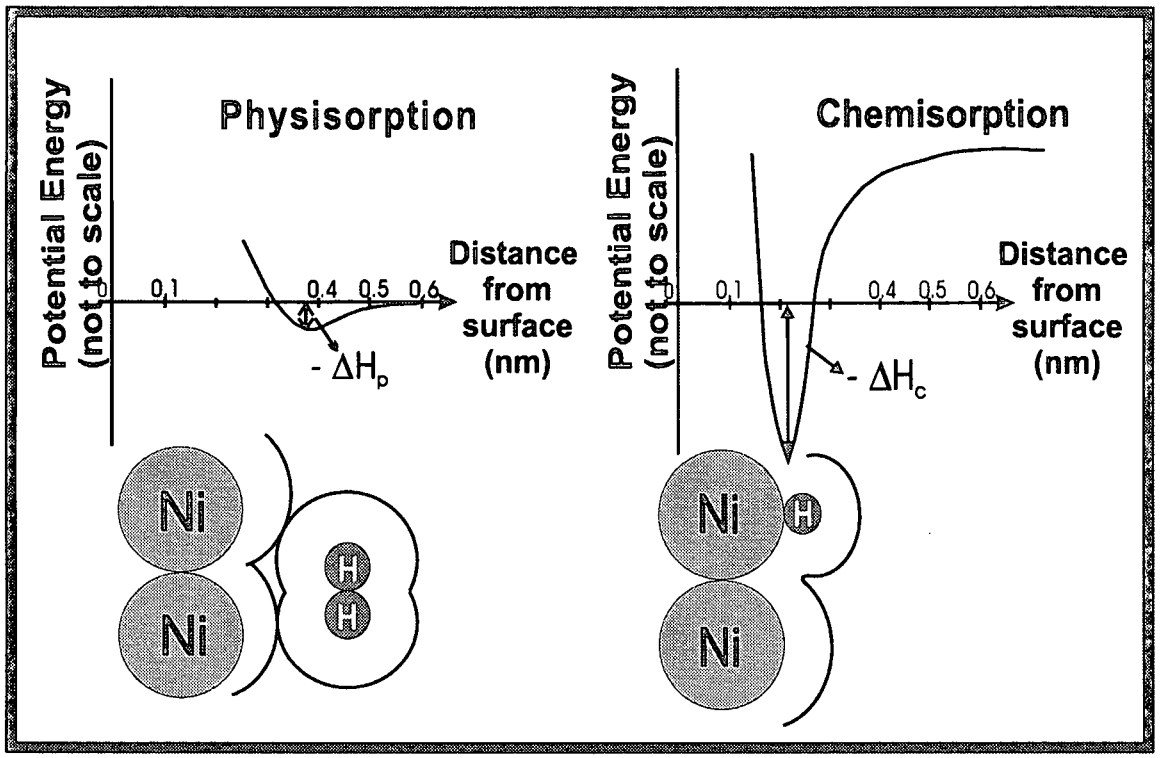

Figure 2.3: The potential energy curves for the adsorption of hydrogen on nickel, and the pictorial representation of the adsorbed states [20].

When a gas molecule approaches the surface, it will experience an initial attractive force. As the distance from the surface decreases, the magnitude of the attractive force at first increases. The force will pass through a maximum and if the molecule continues to move, closer to the surface the attraction will become a repulsive force [19]. Consider the adsorption of hydrogen on nickel, illustrated in Figure 2.3. As the hydrogen molecule approaches the Ni surface the attractive force that exists between the species leads to a decrease in the potential energy. At a certain distance the potential energy reaches a minimum and the molecule becomes physisorbed to the surface. Any decrease in the distance between the two species will result in a repulsive force and a sharp increase in

the potential energy. The heat of physisorption is indicated on the graph by ΔH_p. Physisorption serves as a precursor state for chemisorption. Without physisorption a considerable amount of energy must be added to the system in order to atomise the hydrogen. The hydrogen atoms are more reactive and will chemically react with the Ni surface. If the hydrogen molecule is physisorbed to the surface the transition to the chemisorbed state will require less energy. The molecule, in the physisorbed state, dissociates on the surface and the change in chemistry results in a stronger attraction between the hydrogen and the Ni. The hydrogen chemically reacts with the Ni and becomes chemisorbed. The heat of chemisorption, ΔH_c, is much greater than the heat of physisorption and the distance between the H and Ni much smaller.

2.3.1.4. Physisorption versus Chemisorption

The physisorption system is one where the attractive forces between the adsorbed specie and the surface are relatively non-specific Van der Waals or dispersion forces. The lateral interactions between adsorbed species are of particular interest and due to the small force between the adsorbed specie and the surface there is a high possibility for mobility on the surface. The binding energy between the adsorbed specie and the surface may vary at different sites on the surface due to heterogeneities on the surface. Consequently, three possible situations can be considered. Mobile adsorption occurs where the binding energy is small compared to the value of kT for the adsorbed specie, where k is Boltzman's constant and T the temperature. Localized adsorption is found where the binding energy is slightly larger than kT, but not large enough to prohibit diffusion. Immobile adsorption occurs when the binding energy is so large that it prohibits surface diffusion [19].

Surface heterogeneity is where the binding energy of the various adsorption sites differs. It arises from the fact that the interaction energy between an adsorbed atom or molecule and the surface will depend on the details of the atomic arrangement at the surface site where the adsorbed specie is held. For some sites, the binding energy will be higher than

for other sites. The net effect of the heterogeneity on physical adsorption is an increase in the coverage for any given value of pressure.

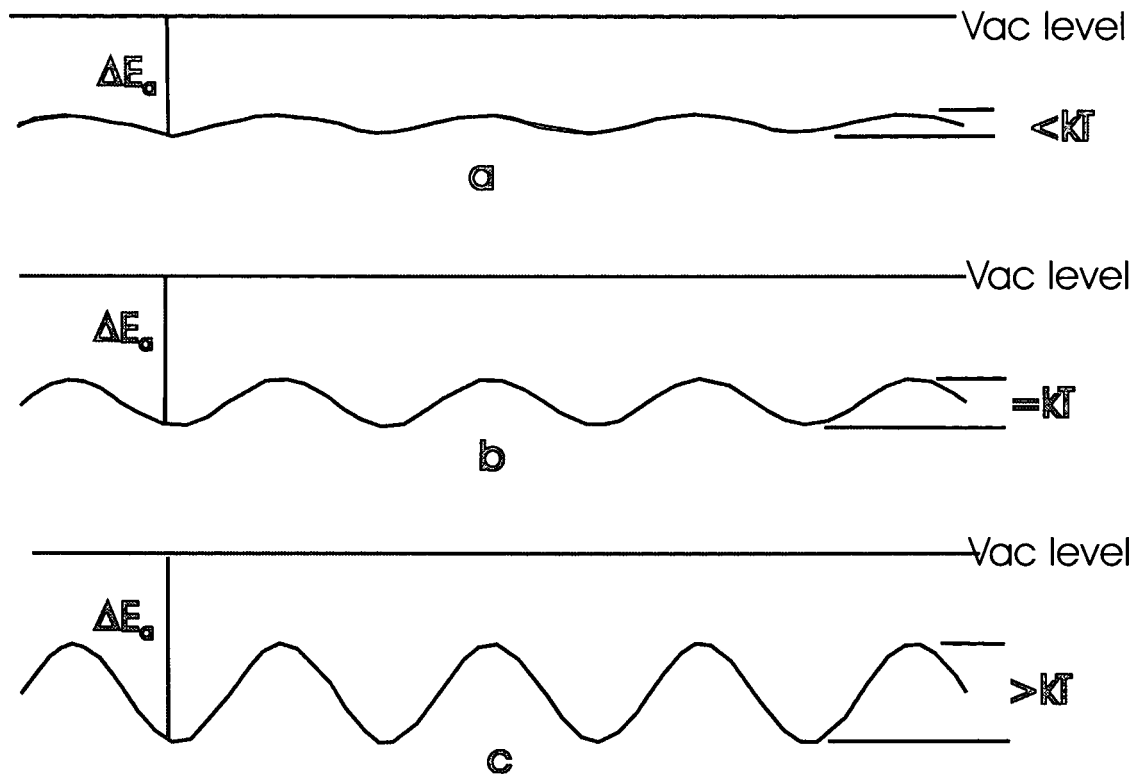

Figure 2.4: The potential energy for a physisorbed atom on a surface for the three different classes of physisorption. (a) Mobile adsorption, (b) localized adsorption and (c) immobile adsorption [19].

With chemisorption, the binding energy between the adsorbed specie and the surface is much larger than for physical adsorption. There are two general types of chemisorption processes, namely molecular adsorption and dissociative chemisorption. Molecular chemisorption occurs when the molecule that adsorbs on the surface remains intact. Molecules with multiple bonds normally undergo this type of chemisorption. In dissociative chemisorption, the molecule, generally those with single bonds, gives rise to separate adsorbed fragments on the surface [21].

2.3.1.5. Kinetics of adsorption

There is a certain equilibrium coverage of gas molecules on the surface of a material associated to each temperature and pressure. This coverage will assume some stable structure and morphology on the surface [16]. The equilibrium condition is uniquely defined and is independent of how the adsorption takes place.

The adsorption of diatomic molecules, on a surface, to form an ordered atomic array occurs in a number of consecutive steps [16]:

1. The collision of the molecules with the surface and the transfer of the momentum of the molecule to the crystalline lattice
2. Migration of the molecule across the lattice surface
3. Dissociation and incorporation into the equilibrium structure.

The rate of each of these processes is temperature dependent and each may be the step that limits the rate of the overall reaction. The rate of adsorption is usually expressed in terms of a quantity called the sticking coefficient *S*. *S* is, in general, a function of temperature and coverage (θ) for any given combination of gas and crystalline surface. The kinetic theory of gases gives an expression for the number of molecules *I* striking a surface which is in contact with a gas at pressure *p*, per unit area per unit time as:

$$I = \frac{p}{(2\pi mkT)^{\frac{1}{2}}} \tag{2.1}$$

where *m* is the mass of a gas molecule, *k* is Boltzman's constant and *T* is the temperature. The total number of molecules incident in time *t* is the exposure *E*. And thus

$$E = \int I dt \tag{2.2}$$

The sticking coefficient S at any fractional coverage θ is then defined as

$$S(\theta,T)=N`\left(\frac{\partial\theta}{\partial E}\right) \tag{2.3}$$

where $N`$ is the number of molecules in one monolayer.

Often the quantity determined from experiment is the mean sticking coefficient relating to the total exposure i.e.

$$\overline{S}=N`\left(\frac{\theta}{E}\right) \tag{2.4}$$

There are three possible relations between S and θ for a maximum coverage of a single monolayer illustrated in Figure 2.5:

1. If the adsorbate has essentially no mobility on the surface but is chemisorbed only if it impinges directly on a suitable unoccupied site the sticking probability will vary with $(1-\theta)$ for monolayer adsorption, this being the probability that any particular adsorption site is available. See graph (a) in Figure 2.5.
2. In cases where the adsorbate is capable of diffusive motion on the surface, the dependence of S on θ may depend appreciably on the morphology of the adsorbate layer. We may consider that the molecule adsorbs in an intermediate weakly bound physisorbed state (also known as the precursor state) and can migrate over the surface with diffusivity D. There will be some reasonable probability of re-evaporation, the root mean square displacement x before desorption is given by:

$$x=\sqrt{2D\tau_e} \tag{2.5}$$

where τ_e is the time from adsorption until re-evaporation. It could also refer to the mean lifetime of the molecule on the surface.

The surface diffusivity appropriate to the precursor state increases exponentially with temperature. The surface diffusivity can be described by the following equation:

$$D = D_0 \exp\left(\frac{-Q_s}{RT}\right) \tag{2.6}$$

where Q_s is the activation energy for surface diffusion of the adsorbed molecule and D_0 is a temperature independent constant. The mean lifetime on the surface will decrease with increasing temperature, thus:

$$\tau_e \propto \exp\left(\frac{\Delta\overline{H}_{ads}}{RT}\right) \tag{2.7}$$

where $\Delta\overline{H}_{ads}$ is the heat of desorption. The heat of desorption is equal in magnitude but opposite in direction from the heat of adsorption, thus if $-\Delta\overline{H}_{ads}$ is the heat of adsorption then $\Delta\overline{H}_{ads}$ is the heat of desorption.

Substitution of equation 2.7 for τ_e into equation 2.5 for the root mean square displacement x will give:

$$x \propto \exp\left\{\frac{\left(\Delta\overline{H}_{ads} - Q_s\right)}{RT}\right\} \tag{2.8}$$

Subsequently x will decrease with increasing temperature since the energy of desorption, $\Delta\overline{H}_{ads}$ is expected to be greater than the energy variation encountered during diffusion over the surface, Q_s. Described by curve (b) in Figure 2.5.

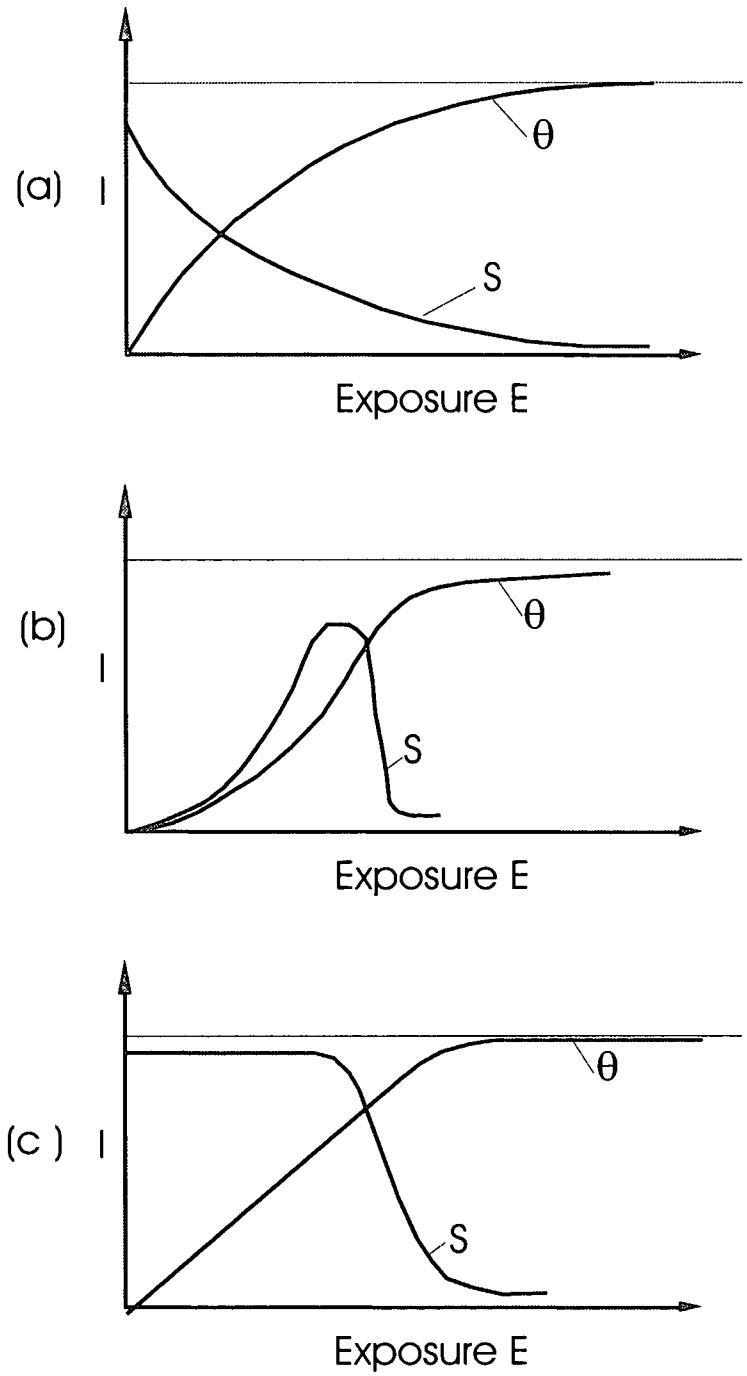

Figure 2.5: Possible variations of coverage (θ), and sticking coefficient (S), with exposure (E).

a) The sticking coefficient varies with ($1-\theta$).
b) In this case, the adsorption occurs by a process of nucleation and growth.
c) The adsorbed species are very mobile on the surface and all physisorbed atoms or molecules will become chemisorbed.

3. If the diffusion length x is *longer* compared to the average separation of sites on the surface at which chemisorption occurs then nearly all molecules that enter the precursor state will become chemisorbed. Under these conditions, the chemisorption rate is determined by the rate of physisorption, which may be essentially coverage independent. If the diffusion length is *smaller* than the separation of potential chemisorption sites, the sticking coefficient or chemisorption rate may be very dependent on coverage. In this case, if the chemisorbed atoms are arranged in islands on the surface only those molecules initially physisorbed within distance x from the edge of an island will be chemisorbed before desorption. This leads to the idea of an active zone surrounding each nucleus or island. If we assume the initial nuclei to be circular in shape, the coverage θ will be proportional to r^2 with r the radius of the nuclei. The perimeter of the island is proportional to r and thus also to $\sqrt{\theta}$. The total area within the active zones will vary approximately as $\sqrt{\theta}$, the dimension of the total island perimeter, until the islands impinge one another. Thus, the chemisorption rate will vary as $\sqrt{\theta}$ following nucleation and then will tend to zero as the coverage approaches unity. Depicted by (c) in Figure 2.5.

2.3.2 Nucleation

The rate of nucleation can be described using the classical nucleation theory for the formation of a spherical nucleus [22].

The free energy change for the formation of a nucleus of radius r is:

$$\Delta G = 4\pi r^2 \sigma + \frac{4}{3}\pi r^3 \Delta G_v \qquad (2.9)$$

where σ is the interfacial free energy and ΔG_v is the free energy per unit volume of the precipitate formed during the reaction. The surface and volume components are plotted along with the ΔG values in Figure 2.6.

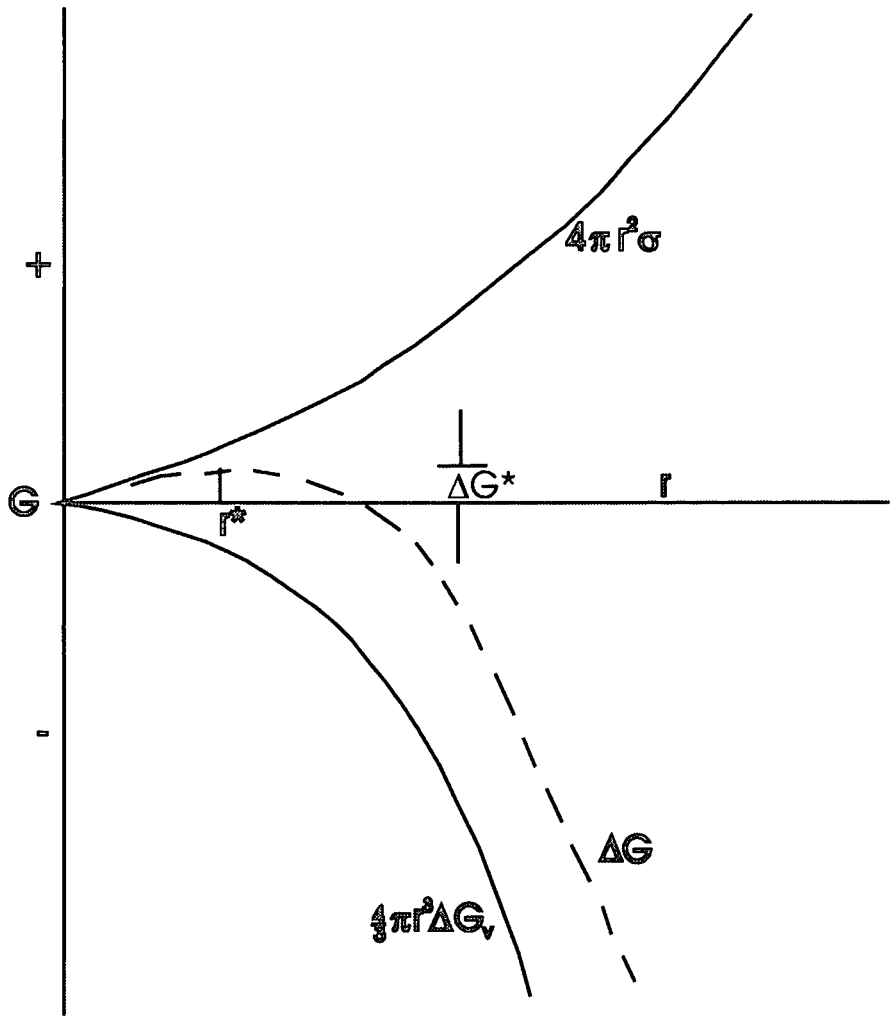

Figure 2.6: The schematic plot of the free energy versus radius of a nucleating particle

Nuclei with radii greater than r* will grow spontaneously.

At r*:

$$\frac{d\Delta G}{dr} = 8\pi r^* + 4\pi r^{*2}\,\Delta G_v = 0 \qquad (2.10)$$

Now r* can be resolved:

$$r^* = \frac{-2\sigma}{\Delta G_v} \qquad (2.11)$$

The statistical probability of finding a nucleus with radius r* is given by the Boltzman factor.

The rate of nucleation can therefore be described by:

$$\text{Rate of nucleation} \propto \exp\left(\frac{-\Delta G^*}{RT}\right) \tag{2.12}$$

ΔG^* is simply the free energy at r*.

2.3.3 Rate of lateral growth

The lateral growth is dependent upon the migration or surface diffusion of the adsorbent specie towards the nuclei. Thus, the classical description of diffusion can be used to determine the rate of lateral growth [23].
The diffusion coefficient, D is dependent on temperature and can be described by the equation:

$$D = D_0 \exp\left(\frac{-Q}{kT}\right) \tag{2.13}$$

D_0 is a constant that is independent of temperature; Q is the activation energy needed for diffusion to take place and T is the temperature.

For an atom adsorbed on the surface of a crystal to move, it requires an energy value E_m. When an atom moves on the surface it pushes other atoms sideways causing the lattice to strain in that region. E_m represents the maximum strain energy as a result of the atom movement. For the movement to continue the atom must have a minimum energy value of E_m. E_m is also referred to as the activation energy for the transition.

The atom vibrates around its own equilibrium position with a frequency v_0. At an oscillatory frequency, v_0 the atom will hit the potential barrier v_0 times per second. The probability to overcome the barrier is given by the Boltzman's factor.

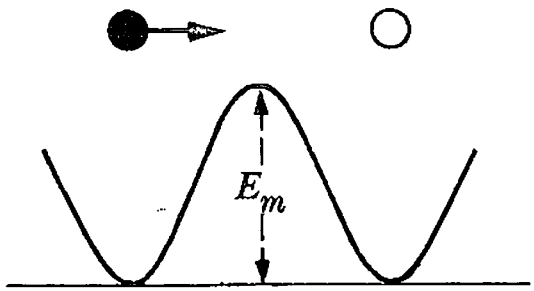

Figure 2.7: The energy barrier E_m seen by the diffusing atom. The solid circle represents an atom and the open circle represents a vacancy.

The jump or transition frequency is therefore given by:

$$\nu = \nu_0 \exp\left(\frac{-E_m}{kT}\right) \tag{2.14}$$

The jumps can occur in three dimensions and can only be made to a vacant site. The probability of finding a vacant site is $\exp\left(\frac{-E_v}{kT}\right)$.

The frequency may now be written as:

$$\nu = z\nu_0 \exp\left(\frac{-Q}{kT}\right) \tag{2.15}$$

where $Q = E_v + E_m$ and z is the number of neighbouring sites to which the atom can jump. The diffusion coefficient for the migration of an adsorbed atom on the surface of a crystal is thus given by:

$$D = \frac{1}{6} z\nu_0 a^2 \exp\left(\frac{-Q}{kT}\right) = D_0 \exp\left(\frac{-Q}{kT}\right) \tag{2.16}$$

The adsorbed specie on the surface of the metal, when in the physisorbed state can migrate over the surface of the metal with diffusivity D. The root mean square displacement x is proportional to D.

2.3.4. Thickening of the oxide layer

Generally, the oxidation of a solid metal (M) by exposure to gaseous oxygen (O) can be described with the following equation [22]:

$$M(s) + \frac{1}{2} O_2 (g) = MO(s)$$

The reaction product MO is the metal oxide. As illustrated in Figure 2.8 the oxide forms a barrier between the metal and the gas.

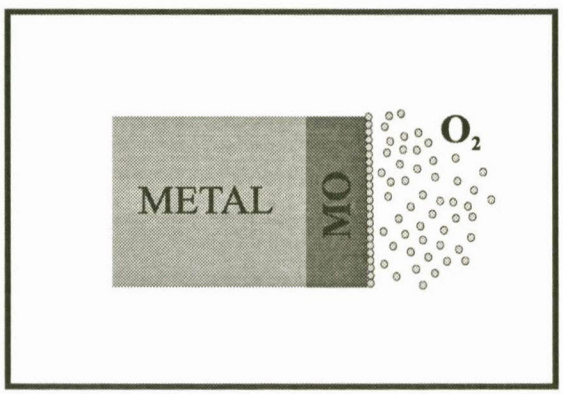

Figure 2.8: The formation of the metal oxide MO that acts as a barrier between the metal and the oxygen and slows down the oxidation process.

Once the barrier has been formed, one or both of the reactants must penetrate the barrier in order for the reaction to continue. Either the metal must diffuse through the oxide to the oxide-oxygen interface where it can react with the oxygen, or the oxygen must diffuse through the oxide to the metal-oxide interface where it can react with the metal. The different mechanisms with which the reactants penetrate the oxide layer forms an important part of the mechanism by which the oxidation occurs.

Wagner's theory of oxidation gives a good approximation of the oxidation process at high temperatures. Wagner's theory is based on the assumption that the growth of the oxide layer is diffusion controlled. Thus, it is the transport of ions across the oxide layer

that controls the rate of scaling. He also assumed that thermodynamic equilibrium is established at each interface.

The flux of metal ions, $j_{M^{2+}}$ is equal in value but opposite in direction to the flux of cation defects (in this case defined as vacancies). Thus, the flux of metal ions can be described with the following equation

$$j_{M^{2+}} = -j_{V_M} = D_{V_M} \frac{C^g{}_{V_M} - C^m{}_{V_M}}{x} \tag{2.16}$$

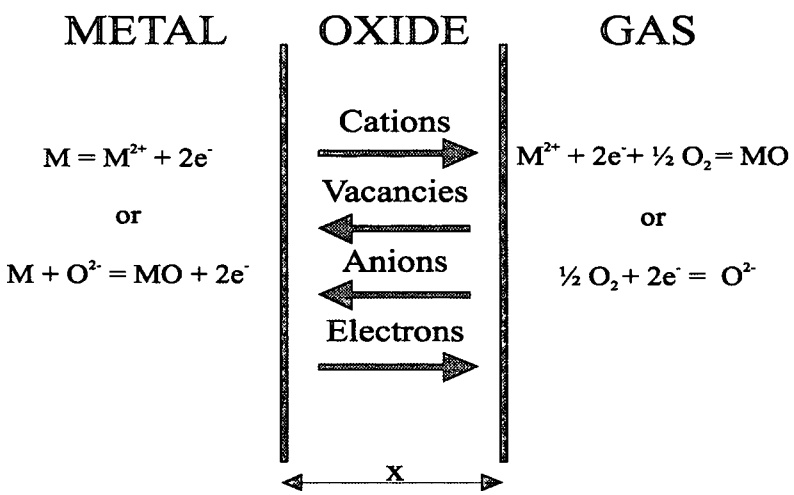

Figure 2.9: Simplified model of diffusion controlled oxidation.

where x is the oxide thickness, D_{V_M} is the diffusion coefficient for the cation vacancies and $C^g_{V_M}$ & $C^m_{V_M}$ are the vacancy concentrations at the scale-gas and scale-metal interfaces.

Since there is equilibrium at the interfaces, the concentration difference is constant. The flux can now be described by:

$$j_{V_M} = const.\frac{dx}{dt} = D_{V_M} \frac{C^g{}_{V_M} - C^m{}_{V_M}}{x} \tag{2.17}$$

and

$$\frac{dx}{dt} = \frac{k`}{x} \tag{2.18}$$

with $k` = D_{V_M}\left(C^{g}{}_{V_M} - C^{m}{}_{V_M}\right)$.

Taking x=0 at t=0 and integrating the equation above will give:

$$x^2 = 2k`t \tag{2.19}$$

This is the parabolic rate law.

The cation vacancy concentration can be described as a function of the oxygen partial pressure, p:

$$C_{V_M} = const.\left(p_{O_2}\right)^{\frac{1}{n}} \tag{2.20}$$

If

$$k` \propto \left[\left(p^{g}_{O_2}\right)^{\frac{1}{n}} - \left(p^{m}_{O_2}\right)^{\frac{1}{n}}\right] \tag{2.21}$$

$p^{m}_{O_2}$ is usually negligible compared to $p^{g}_{O_2}$ thus:

$$k` \propto \left[\left(p^{g}_{O_2}\right)^{\frac{1}{n}}\right] \tag{2.22}$$

The rate at which the oxide layer will grow is therefore dependent on both the temperature, from the relation between D, the diffusion coefficient, and the partial pressure of oxygen.

Wagner's theory is valid for oxidations at high temperatures and where the growth of the oxide layer is diffusion controlled. Many metals oxidise according to the parabolic rate law and are associated with thick coherent oxides.

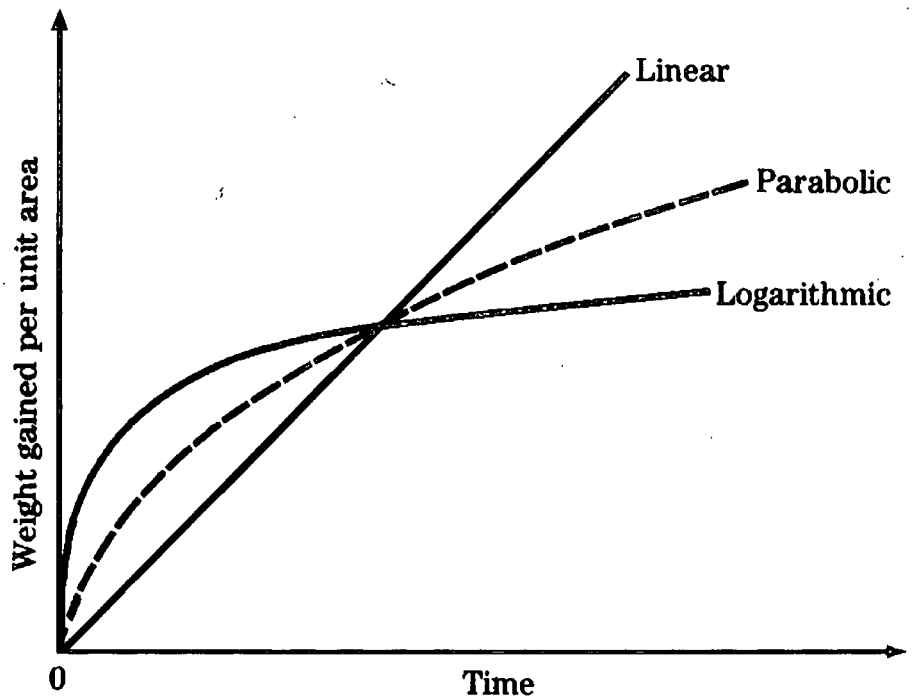

Figure 2.10: The three rate laws for oxidation [24].

The rate of oxidation varies for different metals because of the difference in the mechanism by which the oxidation occurs [24].

The simplest oxidation rate is the linear law:

$$y = k_L t \tag{2.23}$$

where y is the thickness of the oxide, k_L is the linear rate constant and t the time of oxidation. Metals that have cracked or porous oxide films show linear oxidation behaviour since the diffusion of the reactant ions can occur more rapidly.

There are metals that oxidise at ambient or slightly ambient temperatures that follow the logarithmic rate law:

$$y = k_e \log(Ct + A) \tag{2.24}$$

where C and A are constants and k_e is the logarithmic rate constant. These metals, when exposed to oxygen at room temperature initially oxidise very rapidly but the rate decreases with exposure time. Figure 2.10 illustrates the different rate laws.

The mechanism and rate of oxidation varies between different metals and, of course, different alloys. This study focuses on the oxidation of Fe and Fe-Mo alloys. It is therefore necessary to refer to the individual oxidation behaviour of the Fe and the Mo.

2.4. Fe oxidation

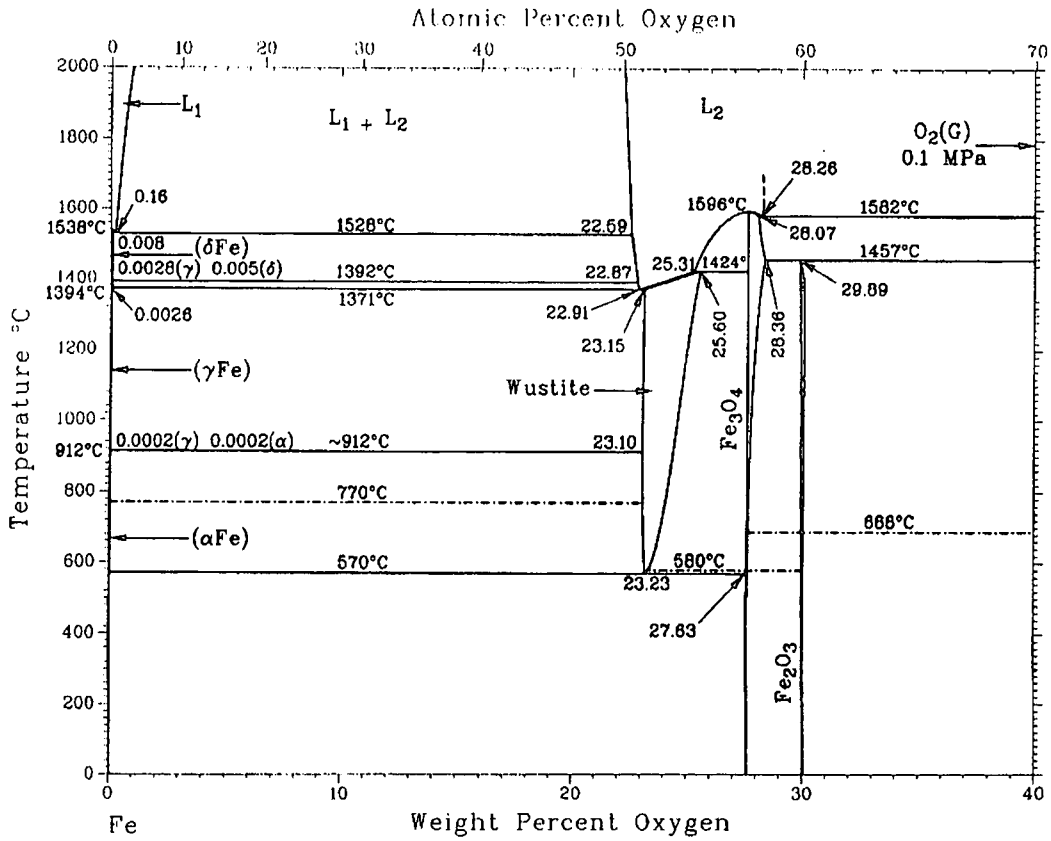

Figure 2.11: Phase diagram for iron oxides [25].

Iron and iron alloys account for 90% of the world's production of metals [24]. The good combination of properties and low cost has led to a wide range of applications for Fe alloys. Under equilibrium conditions, iron can form three oxides, namely Wustite (FeO), Magnetite (Fe_3O_4) and Haematite (Fe_2O_3) [25]. The oxides form in layers as the concentration of Fe and O varies within the oxide layer. The differences in concentrations are related to the diffusion of the Fe and O ions within the oxide layer.

Between 250°C and 1000°C, iron oxidizes according to the parabolic rate law. At low temperatures, oxidation follows the logarithmic rate law.

The most commonly used Fe alloys are the stainless steels, that contain alloy elements such as Cr, Ni and Mo. Cr is added to the Fe to create a protective layer on the surface of the component thus prohibiting the Fe to oxidise.

2.5. Mo oxidation

Molybdenum forms two stable oxide phases namely MoO_3 and MoO_2. With an increase in oxygen concentration or an increase in temperature there is a phase transition and the formation of volatile species. The formation of the volatile MoO_3 is generally referred to as catastrophic oxidation [25] [22].

Molybdenum is commonly used as an alloy element and is particularly good in contributing to creep-resistance. Steels that contain 0,5 % Mo are widely used for steam pipes and super-heaters [25]. Steels that contain between 2% and 3% Mo become dangerous when used in temperatures where MoO_3 becomes volatile. The formation of volatile MoO_3 compounds leads to cracking of the protective oxide scale formed on the surface of the steel. The cracking of the oxide scale could lead to an accelerated corrosion of the component.

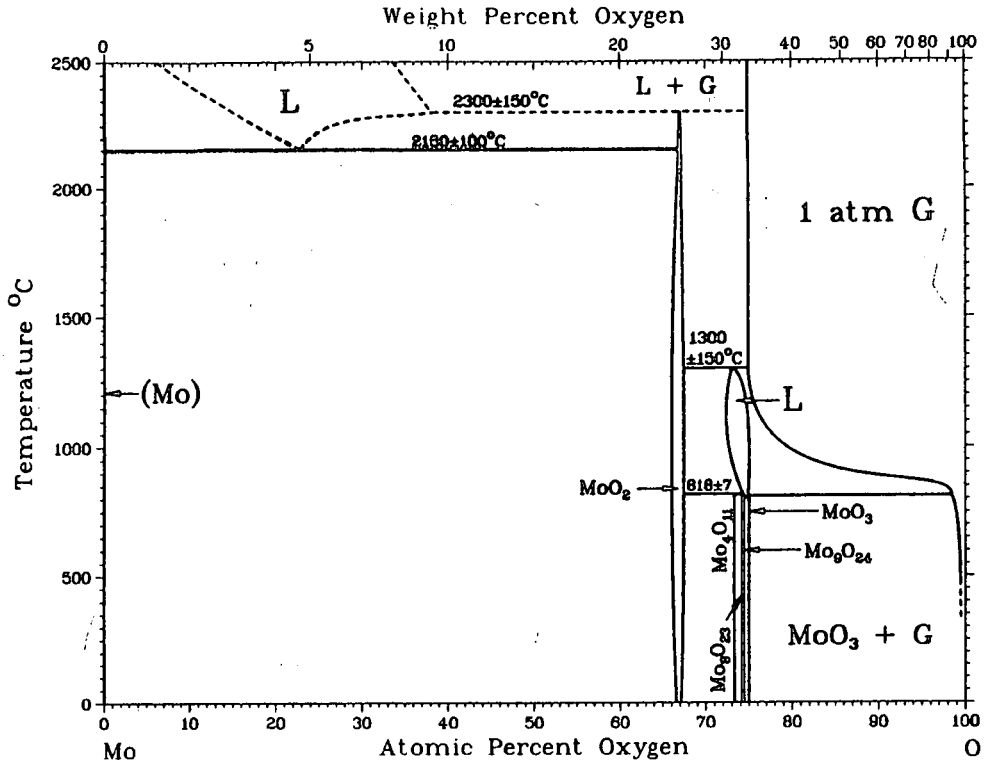

Figure 2.11: Phase diagram for Mo-O [26]

2.6. Fe and Mo in catalysts

Fe based catalysts are used in a number of chemical processes, for example in the synthesis of ammonia and also in the hydrogenation of carbon monoxide [21].

Molybdenum based catalysts are used in the petrochemical industry to remove Sulphur from the organic sulphur compounds found in crude oil. In the presence of sulphur the Mo based catalysts are also used to convert carbon monoxides and hydrogen to alcohols.

Chapter 3

Experimental set-up and procedure

3.1. Introduction

Auger electron spectroscopy (AES) is a surface sensitive technique that is used to study the topmost surface layers of a sample. The AES analysis can be applied to give, for instance, information regarding:

- The elemental and chemical composition in the topmost layers,
- Depth profiling,
- Contamination present at surfaces and interfaces
- Interfacial chemistry
- Thin film layer thickness and identity
- Oxidation and effects of surface modification, and
- Possible causes of adhesion failures.

AES was applied in this study because of the surface sensitivity of the technique. The AES analysis gives information regarding the chemical composition and state of the atoms in the first 4-5 atomic layers. Auger peak changes can be measured against time to give an indication of the rates of surface reactions. Auger peak-to-peak height (APPH) profiles were also obtained whilst sputtering for depth profiling.

The apparatus and specific procedures used in this study will be explained in more detail in this chapter.

3.2. Apparatus

3.2.1. Vacuum chamber

A PHI 590 SAM unit was used in this study. The vacuum chamber is equipped with a 250 l/s turbo molecular pump and a rotary vain pump to attain pressures down to 10^{-6} torr. A 250 l/s ion pump and a Titanium sublimation pump (TSP) are also attached to the system and are used to attain ultra high vacuum $< 10^{-9}$ torr in the chamber. The AES apparatus is housed inside the vacuum chamber and all experiments are performed under ultra-high vacuum conditions. The base pressure in the chamber, for this study, was less than $2x10^{-9}$ torr. The vacuum chamber is divided into an upper and a lower chamber.
The upper chamber contains the AES apparatus, the ionisation pressure gauge, the gas analyser, a differentially pumped ion gun, and the sample carousel. The lower chamber houses the ion pump and the TSP. The upper and lower chambers are separated with a pop-up valve. A leak valve is attached to the lower chamber via a bellows enabling the inlet of gases such as O_2 or N_2.

3.2.2. AES system

The AES system is illustrated in Figure 3.2. The AES system includes a co-axial electron gun and a single pass cylindrical mirror analyser (CMA). The electron gun uses an LaB_6 crystal instead of a tungsten filament. The crystal has a longer lifetime and is more stable than a tungsten filament. The electron gun emits electrons that are accelerated towards the sample. The primary energy is adjustable up to 10 keV. The objective lens is used to focus the electron beam on the sample. The incident beam of high-energy electrons causes Auger transitions within the sample and the consequent emission of Auger electrons.

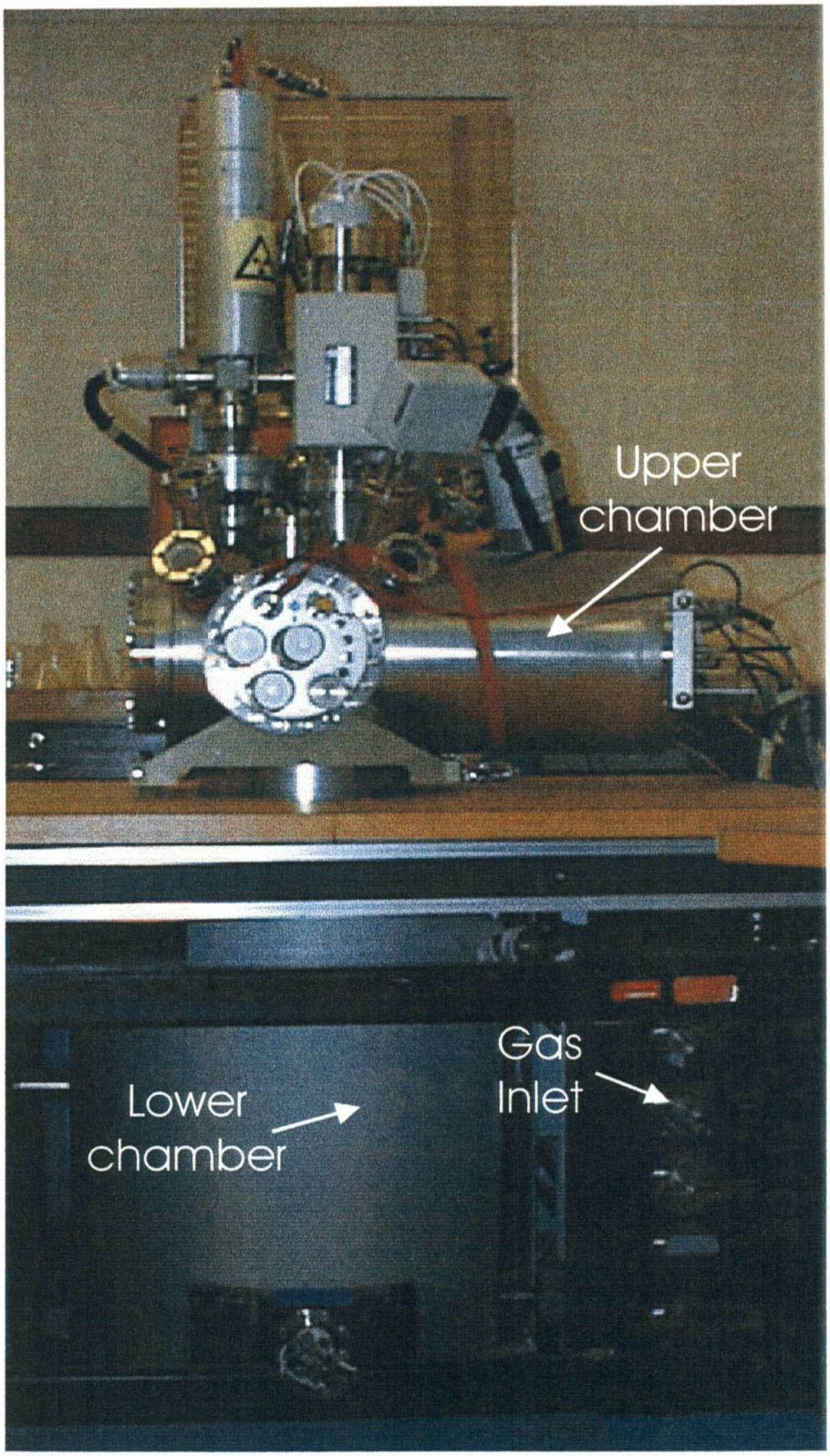

Figure 3.1: A photo of the PHY 590 SAM.

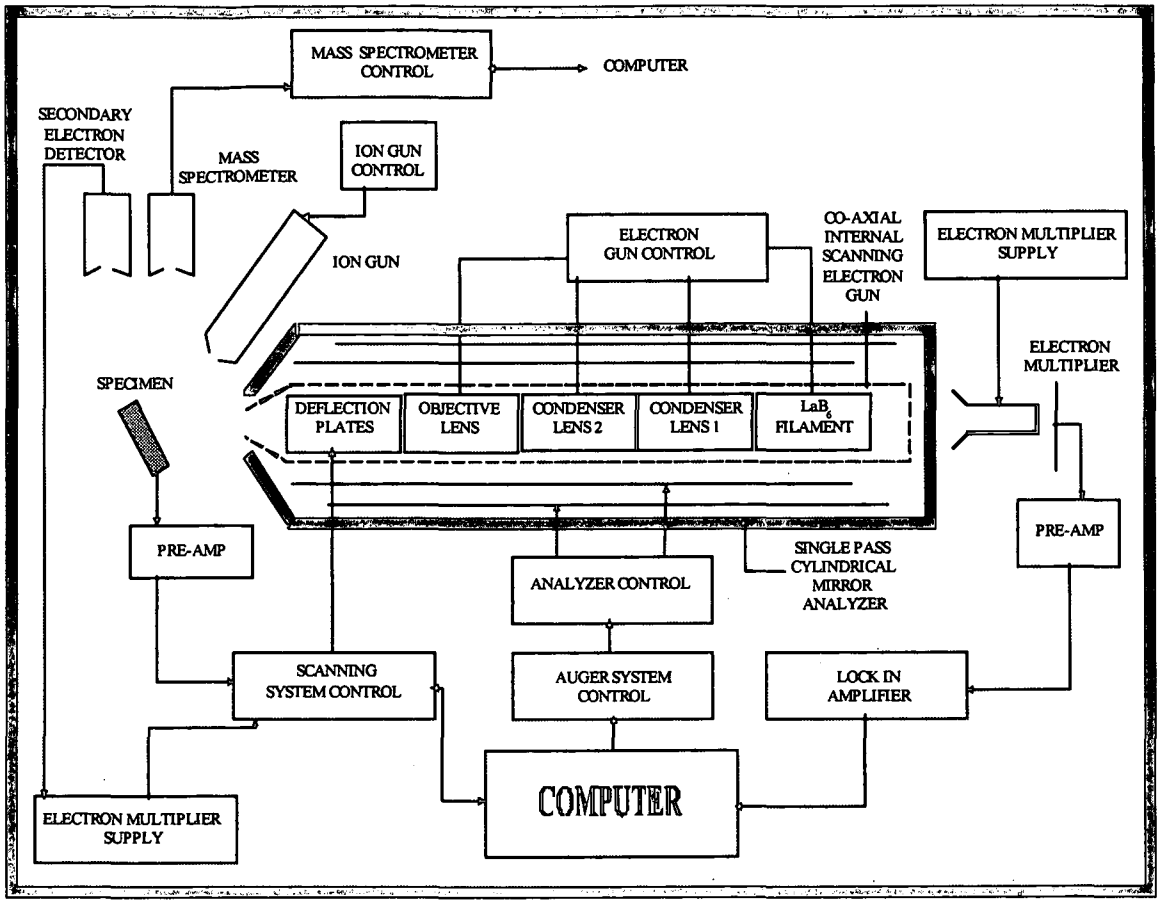

Figure 3.2: Block diagram of the Scanning Auger Microscopy System

The sample carousel forms a 42° angle with the CMA. The Auger process is a well-known phenomenon and the subject is extensively discussed in other sources [27][28]. The energies of the Auger electrons are analysed with the CMA. The emission of secondary electrons is studied with a Secondary electron detector (SED). These emissions are a reflection of the topography of the sample surface and can be used to generate an image of the sample.

A differentially pumped ion gun is used to sputter clean the surface of the sample and to obtain depth profiles.

A mass spectrometer or gas analyser is also attached to the system for the determination of specific gas partial pressures. The gas analyser can also be used to detect the desorption of volatile compounds from the sample surface.

3.2.3. Control Unit Settings

There are several control units attached to the AES system. The settings on the different units are tabulated in Table 3.1.

Electron gun	
V_P	4 kV
I_B	5 μA
Ion gun	
V_{ION}	3 kV
I_{ION}	90 nA
Gas	Ar
Raster (cleaning)	3x3 mm
Raster (depth profiling)	6x6 mm
Spectrometer	
Scan rate	2 eV/s
Modulation energy (peak to peak)	2 eV
Time constant	0.3 s
$V_{MULTIPLIER}$	1400 V
Gas analyser	
I_{GAS}	2 mA
V_{GAS}	2000 V

Table 3.1 AES settings

A multiplexer is used to measure the peak shapes in pre-selected energy intervals with time. The energy intervals used for each element in this study are tabulated in Table 3.2.

The low energy Fe peak is measured to determine the chemical environment of the Fe. The shape of the peak changes if the Fe and O react to form an iron oxide. The Mo has a number of peaks between 96 eV and 220 eV. Many of these peaks overlap with the peaks of other elements such as S, P and Ar. The peak chosen for the multiplexing did not overlap with any of the possible contaminants in the system and was therefore a true reflection of the Mo.

Element	Lower limit	Upper limit	Auger transitions
Fe	686	722	$L_{III}M_{45}M_{45}$
Fe	17	75	$M_{23}M_{45}M_{45}$
Mo	168	197	$M_VN_{23}N_{45+1}$
C	253	282	$KL_{23}L_{23}$
N	360	396	$KL_{23}L_{23}$
O	495	528	$KL_{23}L_{23}$

Table 3.2 Multiplexer energy intervals

3.2.4. Heater unit

The sample holder used in this study contains a filament, which is isolated from the sample with a ceramic disk, and a chromel-alumel thermocouple. The heater control unit regulates the current through the filament and thus controls the temperature of the sample. Figure 3.3 contains photographs of the sample holder used in this study.

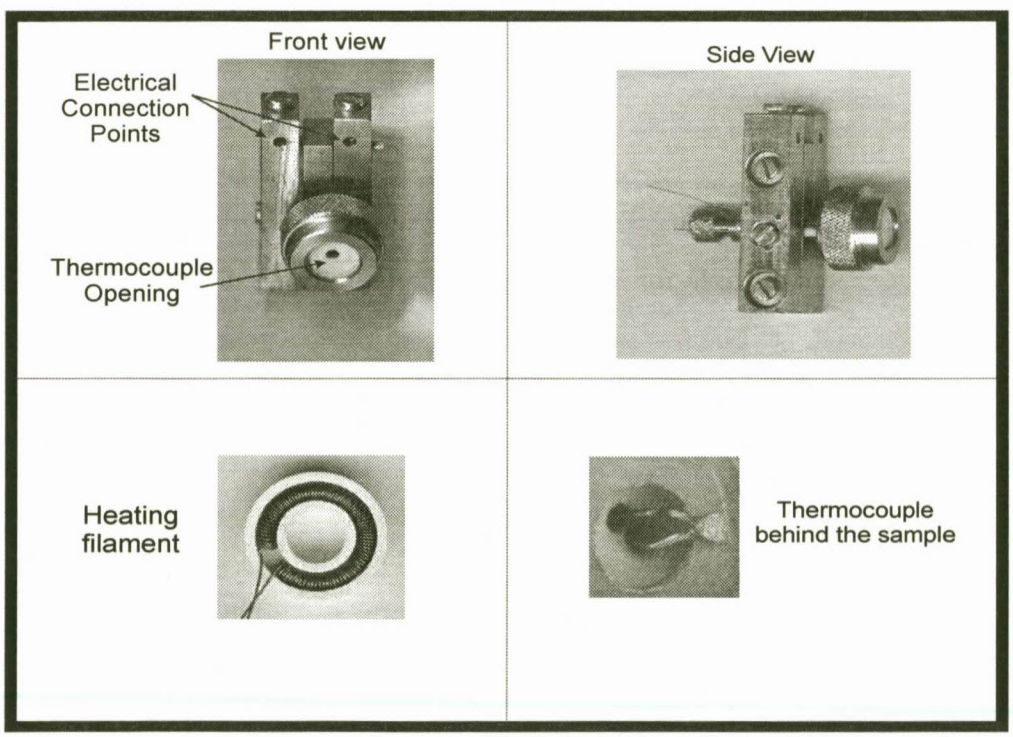

Figure 3.3: The sample holder and heating unit used in this study.

3.2.5. Samples

Four different samples were used in this study, namely:

1. Fe(100) single crystal
2. Mo(100) single crystal
3. Fe(100)-3.5 wt% Mo-N single crystal
4. Mo_2N powder

The Fe (100)-3.5 wt% Mo-N single crystal was obtained from the Max-Planck Institute in Düsseldorf, Germany.

The single crystals were polished to a mirror-like finish with a roughness < 0.1 □m, to remove scratches from the surface. The polishing was done using diamond paste. After polishing, the samples were rinsed thoroughly with distilled water.

The Mo_2N powder was purchased from Goodfellow in Huntingdon, England. The maximum particle size of the powder is 45 μm. The Mo_2N has a density of 9.06 gcm^{-3} and has a 99.5% purity.

3.3. Experimental procedure

3.3.1. Sample preparation in vacuum

Most Fe and Fe-alloy samples contain small quantities of contaminants. The contamination is due to exposure to atmosphere or present during the manufacturing of the sample. Typical contaminants are P, S, N, and O.

The Fe(100)-3.5 wt% Mo-N single crystal was contaminated with C and S. The contaminants were depleted from the surface layer by sputtering the sample at 450°C. As the C and S segregated to the surface, it was sputtered and thus removed from the surface.

Due to the extended sputtering, it was necessary to restore the surface by annealing the sample.

The Fe(100) single crystal was contaminated with N. The sample was annealed at 400°C and continuously sputtered until the N Auger peak could not be detected. Again, it was necessary to anneal the sample to restore the surface.

The Mo_2N powder was pressed into an Indium foil in order to be mounted onto the sample carousel.

The samples were mounted on the sample carousel in the vacuum chamber. The samples on which measurements at various temperatures were performed were mounted in a sample holder. The specific properties of the sample holder are discussed elsewhere [29].

3.3.2. Preparation of the enriched Mo-N layer

The segregation of the Mo and N from the bulk of the sample can be induced through two processes. The first method is simple annealing of the sample for an extended time at a constant temperature and the second method is with linear increase of temperature with time at a constant rate (LTR). The annealing of the sample for an extended time resulted in the segregation of S, thus LTR segregation was done to induce the surface enrichment of Mo and N. As mentioned before there was C contamination in the sample and this also segregated to the surface. The segregation of the C did not inhibit the segregation of the Mo and the N.

Before the LTR was started the sample was sputter cleaned and the temperature increased to 200°. The sputtering was stopped, the Ar gas pumped out and the LTR run started. The computer, connected to the temperature control unit, controls the increase of the temperature from 200°C to 550°C at a rate of 0.15 K/s. The APPH of the Mo, C, and N

were calculated and monitored while segregating. The energy intervals used for these elements are tabulated in Table 3.2.

The LTR segregation resulted in a stable surface composition that remained stable with temperature decrease to room temperature and increase to 550°C.

3.3.3. A typical oxidation run

Great care was taken in this study to keep the experimental conditions constant for the oxidation of the various samples. The filaments were switched on an hour before measurements commenced to allow them to stabilise. Similar procedures were followed for the oxidation of the Fe (100) and the Fe (100)-3.5-wt% Mo-N samples.

The oxidation procedure can be broken down to consecutive steps:

1. The sample was sputter cleaned using the parameters in Table 3.1.
2. An Auger spectrum was taken of the sputter cleaned sample.
3. Whilst sputtering the temperature was increased to the temperature at which the oxidation was to be performed.
4. The valve between the upper and lower vacuum chambers was closed partially to decrease the pump rate and ensure a constant gas flow.
5. The partial pressure of the oxygen was increased to $p(O_2) = 2x10^{-10}$ torr as measured with the gas analyser.
6. As soon as the partial pressure and temperature were stable, usually well within a minute, the measurements were started and the sputtering stopped. Once the sputtering was stopped, the leak valve through which the Ar gas was let into the system was closed and the Ar gas was pumped out of the chamber.
7. Another Auger spectrum was taken after oxidation.

The oxidation for the segregated layer differed slightly from the above procedure. The sample was sputter cleaned and using linear temperature ramping (LTR) the N, C and Mo were segregated to the surface to form a stable surface coverage. The LTR stopped at

550°C after which the sample was cooled to the required temperature. Following the cooling steps 3,4 and 5 from the procedure above was followed.

3.3.4. Depth profiling

Depth profiling was performed after the oxidation of the Fe (100)-3.5 wt% Mo-MoN to determine whether the segregated layer remained intact during oxidation. Since the surface enrichment of the Mo, N, and C was 1-2 mono-layers [2], it was necessary to decrease the sputter rate significantly by increasing the raster area and decreasing the ion current with a factor of 10.

3.3.5. Partial pressure measurements

Before the gas analyser could be used to measure the partial pressure of any gases it had to be set up correctly. The gas analyser can be set to give the total pressure in the system. If it is assumed that the ionisation pressure gauge is correct, the output value for the total pressure from the gas analyser can be adjusted to match the value given by the ionisation pressure gauge. The settings were tested for various pressures. To increase the pressure in the system N_2 was leaked into the system. The N_2 that was used for this purpose was 99.999995% pure. N_2 gas was used since the ionisation pressure gauge was factory calibrated with N_2. The condenser on the ionisation pressure gauge becomes saturated at pressures above $1x10^{-6}$ torr and the measurements at and above this pressure value become subject to error.

Once the gas analyser was set-up correctly the output for a given amu (atomic mass unit) value was a direct indication of the partial pressure of that specific gas.

The gas analyser has a default DC Offset value that must be corrected before measuring the partial pressures. The correction was done within the software program. The DC

Offset is measured at 200 amu and this value is deducted from the spectrum and the partial pressures measured.

While performing an oxidation, the partial pressure of the oxygen must be kept constant. The software was upgraded to measure and display the partial pressure of the oxygen after measuring an energy region set in the multiplexer. The software upgrading will be discussed in section 3.4.1.

3.3.6. Desorption studies

In many studies it is necessary to investigate the formation of volatile compounds that desorb from the sample surface. The software program, VisiScan 2.6, was upgraded to allow the measurement of the partial pressures of five gases with time. The peaks are measured with a 0.5 amu width and the peak height noted versus time.

The user can enter the required amu values to be monitored in the fields provided. The program will measure the peak shape within a 0.5 amu width of the value entered. The peak height is calculated and plotted on the screen against time. The values are also saved into data files for further use.

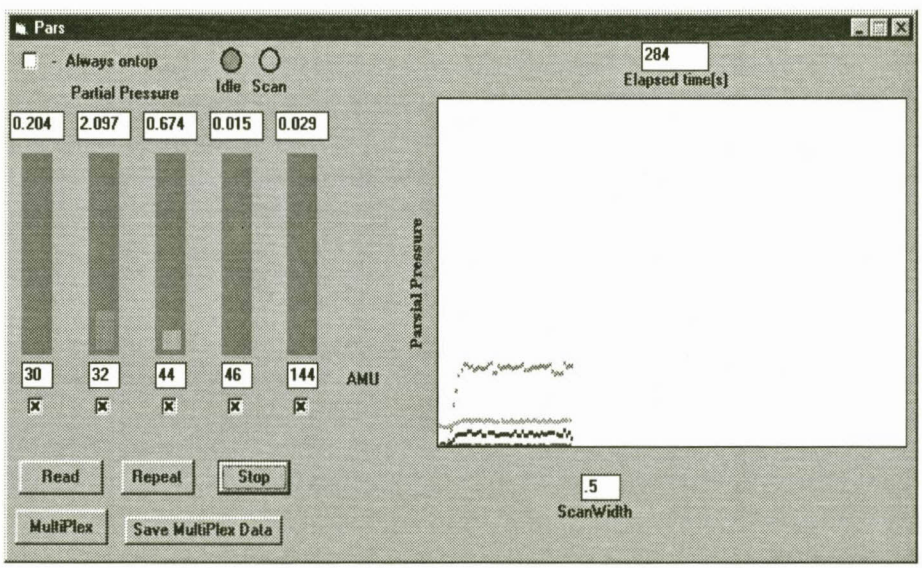

Figure 3.4: The Partial Pressure Multiplexer window.

3.4. Computer controls

A computer has been incorporated into the AES system to simplify data acquisition and processing. The VisiScan version 2.6 software package was used in this study. The package description and manual is presented elsewhere [30].

The computer performs a number of important functions, which include the following:

1. The computer controls the voltage on the CMA via the Auger system control unit and can thus determine the energy to be analysed.
2. The output from the lock-in amplifier is read, saved, and plotted against the energy value.
3. The software package has a multiplexer that facilitates the measurement of peak shapes as a function of time. The APPH values can be calculated and saved along with the peak shapes of the relevant elements.
4. Whilst the multiplexer is in use, the computer can measure the partial pressure for a given gas via the gas analyser after each APPH measurement and display the value in the partial pressure window.
5. The computer is also connected to the temperature control unit, thus it can be used to control the heater filament current. This enables the user to keep the temperature constant or ramp the temperature at a set rate via the computer versus manual control.
6. When connected to the electron gun control unit, the computer can control the position of the electron beam. In combination with the SED output this function is used to obtain images of the sample and elemental maps.

3.4.1. Software upgrades

As mentioned in previous paragraphs the software package was upgraded and adapted for this specific study. The incorporation of the partial pressure measurements in the

multiplexer, the mass spectrometer multiplexer for desorption studies and the upgrading of the gas analyser were necessary modifications that were made to the software package. Figure 3.5 is a flow diagram of the computer routine used for the AES multiplexer and the partial pressure monitoring. This subroutine is available on request.

At point A, in Figure 3.5, the program will determine whether the partial pressure measurements are required. If the measurements are not needed the program will bypass this subroutine. The subroutine in the grey shaded box illustrates the software upgrading done for this study.

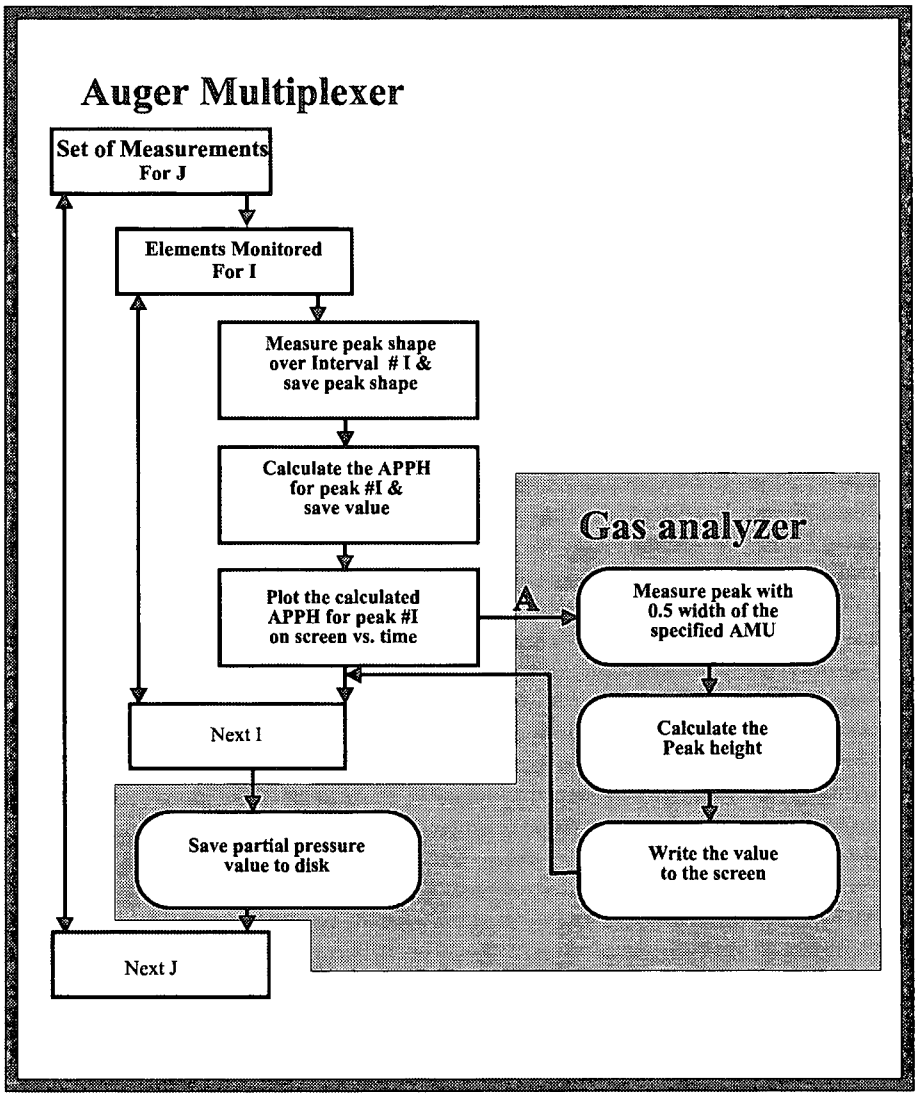

Figure 3.5: The Auger and partial pressure multiplexer computer routines illustrated as flow diagrams

Chapter 4

Mathematical Analysis

4.1. Introduction

In order for a scientist to interpret data correctly it is sometimes necessary to change the format in which the data is presented. In this study the thickness of an over-layer was calculated. This chapter focuses on the methods applied to the AES data to give the thickness of the oxide over-layer.

To determine the thickness of an over-layer it is necessary to evaluate the expression for the Auger yield of an element. It is important to consider the most important variables in the expression as well as the assumptions made in the derivation of the expression. It will be shown that there is more than one expression that is used to determine the thickness of the over-layer, especially for elements in the substrate having Auger peaks that differ in energy.

4.2. The Auger yield

The following expression is generally used for the Auger yield of an element **A** [27]:

$$I_A = I_0 \gamma \sigma_A(E_0) \sec\alpha R_m(E_A) T(E_A) D(E_A) \int_0^\infty N_A(z) \times \exp\left[-\frac{z}{\lambda_m(E_A)\cos\theta}\right] dz \qquad (4.1)$$

$$I_A = K R_m(E_A) \int_0^\infty N_A(z) \times \exp\left[-\frac{z}{\lambda_m(E_A)\cos\theta}\right] dz \qquad (4.2)$$

with $$K = I_0 \gamma \sigma_A(E_0) \sec\alpha(E_A) T(E_A) D(E_A) \qquad (4.3)$$

where I_o is the primary electron current, $\sigma_A(E_o)$ is the ionisation cross section of atom ***A*** by electrons with energy E_o, α is the angle of incidence of the primary electrons, and $R_m(E_A)$ is the backscattering term. $R_m(E_A)$ is dependent on both the matrix m and the

binding energy of the core level electron involved in the transition leading to an Auger electron with energy E_A. $T(E_A)$ is the transmission efficiency of the spectrometer, $D(E_A)$ is the efficiency of the electron detector, $\lambda_m(E_A)$ is the inelastic mean free path in the matrix m and θ is the angle of emission.

It is necessary to consider the inelastic mean free path and the backscattering more closely. This will be done in the following sections.

4.3. The inelastic mean free path, λ

The created Auger electron has a probability e^{-1} of travelling a distance, characterized as the inelastic mean free path in the matrix (λ_m), before being in-elastically scattered and no longer contributing to the Auger electron peak. The characteristic depth from which Auger electrons can be emitted is $\lambda_m \cos\theta$, where θ is the angle of emission to the surface normal. This combined term is known as the escape depth.

From Powell [31], the inelastic mean free path (IMFP), λ in $\mathring{A}$ is given by:

$$\lambda = E / \left\{ E_p^2 \left[\beta \ln(\gamma E) - (C/E) + (D/E^2) \right] \right\} \tag{4.4}$$

where E is the electron energy in eV, $E_p = 28.8(N_v \rho / M)^{1/2}$ is the free-electron plasmon energy in eV, ρ is the density in gcm^{-3}, N_v is the number of valence electrons per atom (for elements) or molecule (for compounds) and M is the atomic or molecular weight.

The terms β, γ, C and D are adjustable parameters that can be determined to fit the calculated IMFP values. Tanuma [32] equate them to the following expressions:

$$\beta = -0.10 + 0.944/(E_p^2 + E_g^2)^{1/2} + 0.069\rho^{0.1} \tag{4.5}$$

$$\gamma = 0.191\rho^{-0.50} \tag{4.6}$$

$$C = 1.97 - 0.91U \tag{4.7}$$

$$D = 53.4 - 20.8U \tag{4.8}$$

$$U = N_v \rho / M = E_p^2 / 829.4 \tag{4.9}$$

where E_g is the band-gap energy in eV for non-conductors.

The calculated IMFP for Fe (Auger electron with energy 47 eV) in pure Fe is

$\lambda_{Fe}(E_{Fe}) = 4.295$ Å

The calculated IMFP for Fe (Auger electron with energy 52 eV) in iron oxide is

$\lambda_{ox}(E_{Fe}) = 4.847$ Å

The calculated IMFP for Fe (Auger electron with energy 47 eV) in Fe-3.5wt% Mo-N is

$\lambda_{Fe}(E_{Fe\text{-}Mo\text{-}N}) = 4.264$ Å

4.4. The backscattering term, r_m

The ionisation of level X in atoms is due to the primary electron beam. There is additional ionisation of the level due to the backscattered energetic electrons. The calculations by Shimizu and Ichimura [32] are most complete and their semi empirical expressions are presented.

The total contribution to the ionisation is given by $(1 + r_m)$, where the term presents the ionisation of the primary beam plus the backscattering term (r_m).

The backscattering term r_m, according to Shimizu [32]-[34], depends on the atomic number Z and the binding energy E_b of a particular element on the surface, as well as the primary electron energy E_o.

The backscattering term, r_m, is given by:

$$r_m = (2.34 - 2.10\ Z^{0.14})\left(\frac{E_o}{E_b}\right)^{-0.35} + (2.58\ Z^{0.14} - 2.98) \qquad (4.10)$$

where Z is the mean atomic number of the matrix, E_0 the energy of the primary electron beam and E_b the binding energy of the core level involved in the Auger transition.

The following numerical values are used for a pure Fe substrate and an iron oxide substrate

$Z_{Fe} = 26$, $Z_{oxide} = 14$

$E_0 = 4000$ eV

$E_{b1} = 56$ eV is the binding energy resulting in an Auger electron with energy 47 eV.

$E_{b2} = 710$ eV is the binding energy resulting in an Auger electron with energy 703 eV.

Using the above numerical values gives the backscattering in:

- a pure iron matrix contributing to the low energy Fe Auger peak
  $r_{Fe}(56eV) = 0.873$
- a pure iron matrix contributing to the high energy Fe Auger peak
  $r_{Fe}(710eV)) = 0.559$
- an iron oxide (Fe_2O_3) matrix contributing to the low energy Fe Auger peak
  $r_{Fe}(56eV) = 0.627$
- an Fe-3.5wt% Mo-N matrix contributing to the low energy Fe Auger peak
  $r_{Fe\text{-}Mo\text{-}N}(56eV) = 0.878$

The overlapping of Auger peaks and the changes in peak shapes with changes in the element's chemical environment has led to the development of the linear least squares method. The following section will expand on this subject.

4.5. Linear Least Squares fit

The superposition of two or more standard spectra is often used to fit and explain features in a measured Auger spectrum. In this approach the measured spectrum, b, of N channels is represented by a linear combination of the K standard spectra [35].

$$Ax = b \tag{4.11}$$

Here A is an N x K matrix with the standard spectra as columns and x a vector with length K containing the fractions and is given by:

$$\boldsymbol{x} = \left(A^T A\right)^{-1} A^T \boldsymbol{b} \tag{4.12}$$

This gives the least squares solution to the over determined system.

In practice the function that will be minimized is the sum of the squares of the difference between the measured intensity $I(E)$ at energy E and the calculated intensity $I_C(E)$

$$f = \sum_E \left[I(E) - I_C(E)\right]^2 = \sum_E s_E^2 \tag{4.13}$$

The parameters can be easily determined by a computer subroutine. The fractions, that give the lowest f value, are considered the best fit.

In this investigation the linear least squares method is used to extract the contributions of an element in different chemical states to the measured Auger peak.

4.6. Determining the thickness

Consider a substrate **A** covered with a thin layer **B** of thickness d_B (see Figure 4.1.). The intensity of the Auger signal from **A** without any layer on top is I_A^∞. The layer on top of **A** is responsible for the attenuation of the signal from **A**. For this specimen the signal of **A** is given by:

$$I_A = I_A^\infty \exp\left[-\frac{d_B}{\lambda_B(E_A)\cos\theta}\right] \tag{4.14}$$

Here $\lambda_B(E_A)$ is the inelastic mean free path (in the overlayer **B**) of Auger electrons coming from **A** with energy E_A.

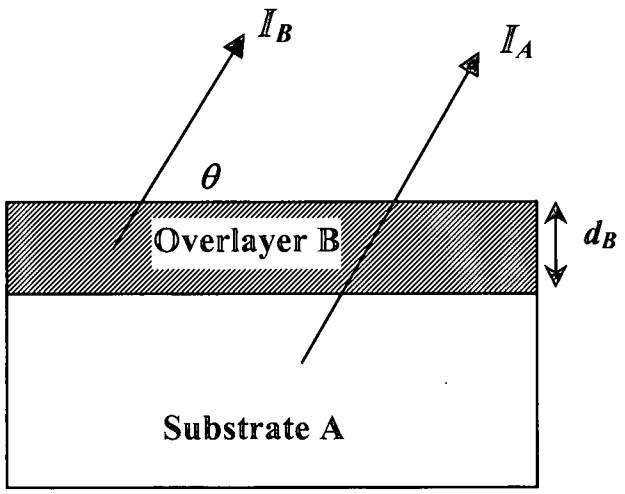

Figure 4.1 Illustrating the Auger signals from different sections in the specimen.

The Auger signal for pure element **B** (using equation 4.2) is:

$$I_B^\infty = KR_B(E_B)[\lambda_B(E_B)\cos\theta] \tag{4.15}$$

From equation (4.15) an expression for K can be obtained.

$$K = \frac{I_B^{\infty}}{R_B(E_B)\lambda_B(E_B)\cos\theta} \tag{4.16}$$

For a thin layer, the assumption is made that the only contribution to the backscattering is from the substrate *($R_A(E)$)* [27]. The signal from the overlayer is now:

$$I_B = KR_A(E_B)\int_0^{d_B} N_B(z)\times\exp\left[-\frac{z}{\lambda_B(E_B)\cos\theta}\right]dz \tag{4.17}$$

and

$$I_B = KR_A(E_B)\lambda_B(E_B)\cos\theta\left\{1-\exp\left[-\frac{d_B}{\lambda_B(E_B)\cos\theta}\right]\right\} \tag{4.18}$$

If the experimental conditions for the standard and the measured signals are the same it is possible to assume the variable K as constant and substituting equation (4.16) into equation (4.18) gives:

$$I_B = I_B^{\infty}\frac{R_A(E_B)}{R_B(E_B)}\left\{1-\exp\left[-\frac{d_B}{\lambda_B(E_B)\cos\theta}\right]\right\} \tag{4.19}$$

It is clear that the thickness of the overlayer can be determined by using either equation (4.14) or equation (4.19).

4.6.1. Oxide thickness of the Fe based specimen

When using AES to study the oxidation of Fe, the low energy region (20 –70 eV) is monitored and the change in peak shape of the Fe is used to determine the fraction of iron oxide. The thickness of the oxide layer formed on an Fe sample can be

determined from equation (4.14) and equation (4.19). For this application these equations can be written as:

$$I_{Fe} = I_{Fe}^{\infty} \exp\left[-\frac{d_{ox}}{\lambda_{ox}(E_{Fe})\cos\theta}\right] \tag{4.20}$$

and

$$d_{ox} = -\lambda_{ox}(E_{Fe})\cos\theta \quad \ln\left[\frac{I_{Fe}}{I_{Fe}^{\infty}}\right] \tag{4.21}$$

$$I_{ox} = I_{ox}^{\infty}\frac{R_{Fe}}{R_{ox}}\left\{1-\exp\left[-\frac{d_{ox}}{\lambda_{ox}(E_{ox})\cos\theta}\right]\right\} \tag{4.22}$$

and

$$d_{ox} = -\lambda_{ox}(E_{ox})\cos\theta \quad \ln\left[1-\frac{I_{ox}R_{ox}}{I_{ox}^{\infty}R_{Fe}}\right] \tag{4.23}$$

4.6.2. Evaluating the expressions for the oxide thickness

Equations (4.20) and (4.22) give the sum of the fractions of pure Fe and Fe oxide contributing to the low energy AES Fe peak. It is clear that the sum of the fractions is not necessarily equal to 1, but depends on the backscattering ratios and the oxide thickness d_{ox} (from equation 4.23).

$$\frac{I_{Fe}}{I_{Fe}^{\infty}} + \frac{I_{ox}}{I_{ox}^{\infty}} = \frac{R_{Fe}(E_{Fe})}{R_{ox}(E_{Fe})}\left\{1-\exp\left[-\frac{d_{ox}}{\lambda_{ox}(E_{ox})\cos\theta}\right]\right\} + \exp\left[-\frac{d_{ox}}{\lambda_{ox}(E_{Fe})\cos\theta}\right] \tag{4.24}$$

For very low oxide coverage the sum is 1 and at high oxide coverage the sum is $\frac{R_{Fe}}{R_{ox}}$.

This is illustrated in Figure 4.2. This observation is an important factor, since the sum of the fractions is used to test the accuracy of the measurements. It is thus not valid to determine the contribution of one element and then determine the fraction of element 2 by assuming the sum of the fractions is equal to 1.

One can extract the contributions of pure Fe and Fe in the oxide from the measured peak by using standards of pure Fe and Fe oxide in combination with a linear least squares method (from section 4.5).

The conclusion must therefore be made that equation (4.23) is only applicable for a low oxide coverage and that it is not valid for an infinitely thick oxide layer. The assumption made in equation (4.18) that the backscattering is only from the substrate changes when the oxide layer becomes sufficiently thick. This led to the uncertainty of using equation (4.23). The validity of equation (4.23) for different over-layer thicknesses remains questionable. Is the equation valid for less than a mono-layer, for 1 mono-layer or for 100 mono-layers? This question will be addressed again in chapter 6 and 7.

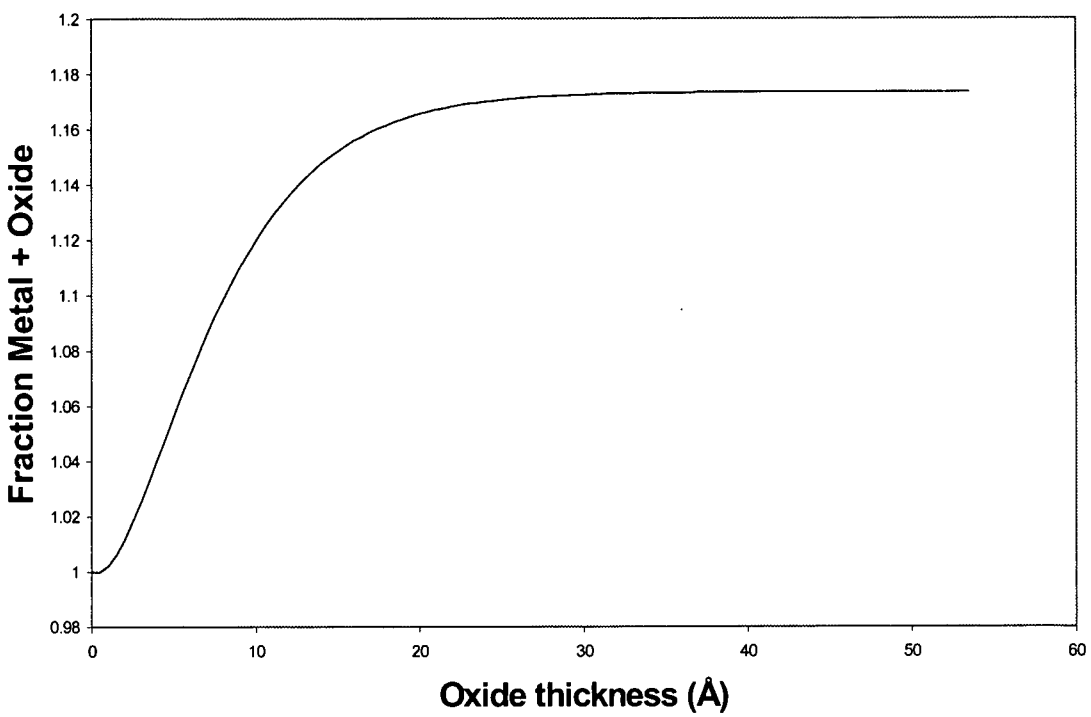

Figure 4.2: Change in the sum of the fractions of the pure metal and metal oxide as a function of coverage using equation (4.24) and the parameters in section 4.3 and 4.4.

4.7. Data processing procedure

The procedure for using the low energy Fe peak to determine the thickness of the oxide as a function of oxygen exposure would be:

- Record the low energy region (20 – 70 eV) as a function of exposure using, for instance, a multiplexer capable of storing the peak shapes.
- Record standard spectra (under the same experimental conditions as the previous step) of the species involved in the oxide formation for example Fe and Fe oxide.
- Use the linear least squares method to determine the fractions of the pure Fe and iron oxide, contributing to the measured spectrum, as a function of exposure.
- Calculate the inelastic mean free path using equation (4.4)
- Calculate the backscattering using equation (4.10)
- Use equation (4.21), the fraction of iron in the measured peak and the escape depth of the low energy Auger electrons of the Fe in the iron oxide to determine the oxide thickness.
- The same equation (4.21) and a high energy Auger electron signal from the substrate can be used to calculate the thickness.
- The linear least squares method also yields the fractions of the iron oxide. Using this information and equation (4.23) the oxide thickness as function of the exposure is known.

Chapter 5

Experimental results and discussion

5.1. Introduction

The oxidation behaviour of Fe(100) can be used as a point of reference to determine the influence of the alloy elements on the oxidation behaviour of the Fe(100)-3.5wt%Mo-N sample. The oxidation behaviour of the Fe(100) and the Mo(100) will first be presented and discussed in this chapter and the discussion on the oxidation behaviour of the Fe(100)-3.5wt%Mo-N, with and without the segregated MoN layer, will follow from that.

5.2. Fe(100) oxygen exposures

5.2.1. Room temperature oxygen exposure

Before the sample was exposed to the oxygen environment it was sputter cleaned using the parameters in Table 3.1. The Auger spectrum taken before the sputter cleaning indicates the presence of contamination of oxygen on the sample surface. After sputter cleaning there were no contaminants on the surface of the sample. The AES spectra are illustrated in Figure 5.1. After the oxygen exposure the change in the low energy Fe AES peak is visible as well as a definite increase in the O peak.

Whilst sputtering, the oxygen was leaked into the system to the required pressure. The procedures are set out in more detail in chapter 3. Once the pressure was stable, the multiplexer was started and sputtering stopped. The energy intervals for O and Fe, as tabulated in Table 3.2, were used for multiplexing the Auger peak-to-peak heights (APPH). The sample was exposed to the oxygen for several hours.

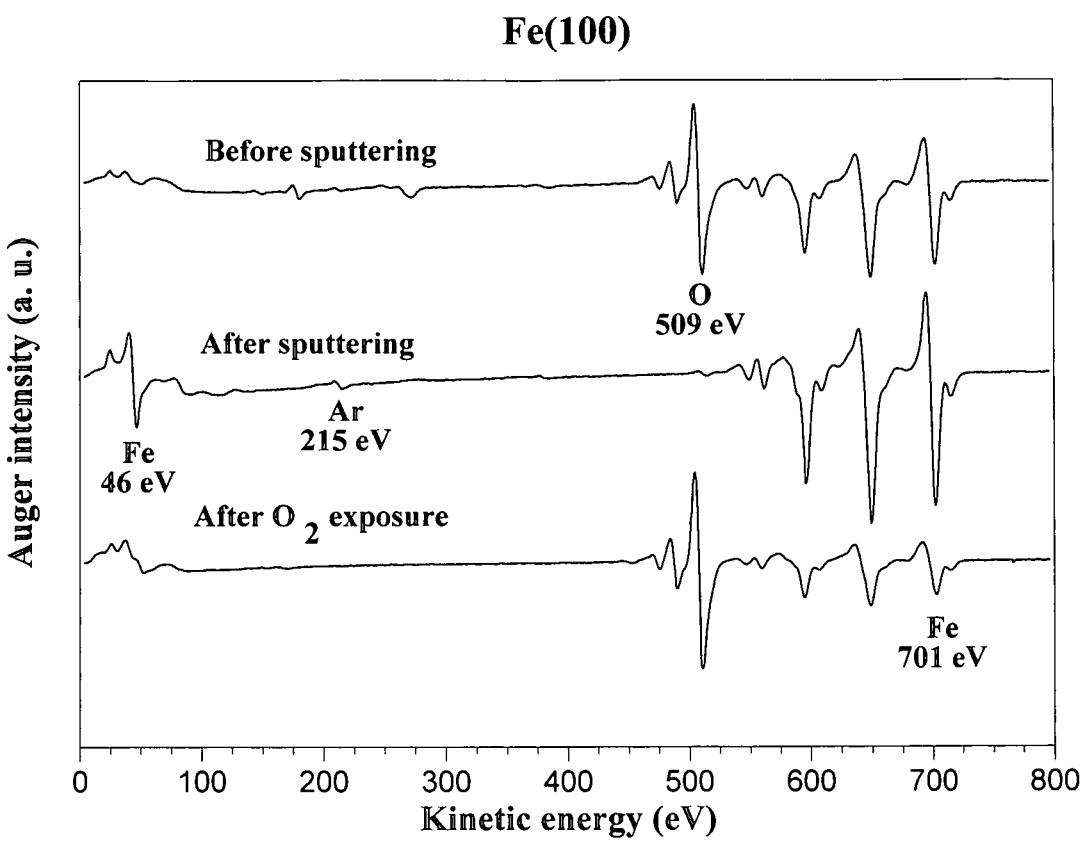

Figure 5.1: The AES spectra of the Fe(100) sample before and after sputtering as well as the spectrum taken after oxygen exposure.

The profile of the APPH for the relevant elements as a function of the exposure is illustrated in Figure 5.2. The oxygen exposure time is described by the term Langmuir (L) where 1L = 1 x 10^{-6} torr O_2.s. The profile indicates a sharp rise in the O APPH up to 1 L exposure where the O APPH reaches a maximum value. Further exposure results in a slow decline of the O APPH as seen in the profile. The 46 eV Fe APPH values drop sharply up to 0.25 L exposure. Further exposure results in a plateaux for the APPH values for the 46 eV Fe. The high energy Fe (701 eV) APPH values also decrease sharply up to

0.25 L exposure and continue to decrease slowly with further exposure.

At room temperature the Fe surface reacts rapidly with the oxygen atmosphere. The reaction follows a logarithmic rate. The chemical reaction between the O and Fe is evident from the change in the shape of the low energy Fe peak, in accordance with literature [36][37].

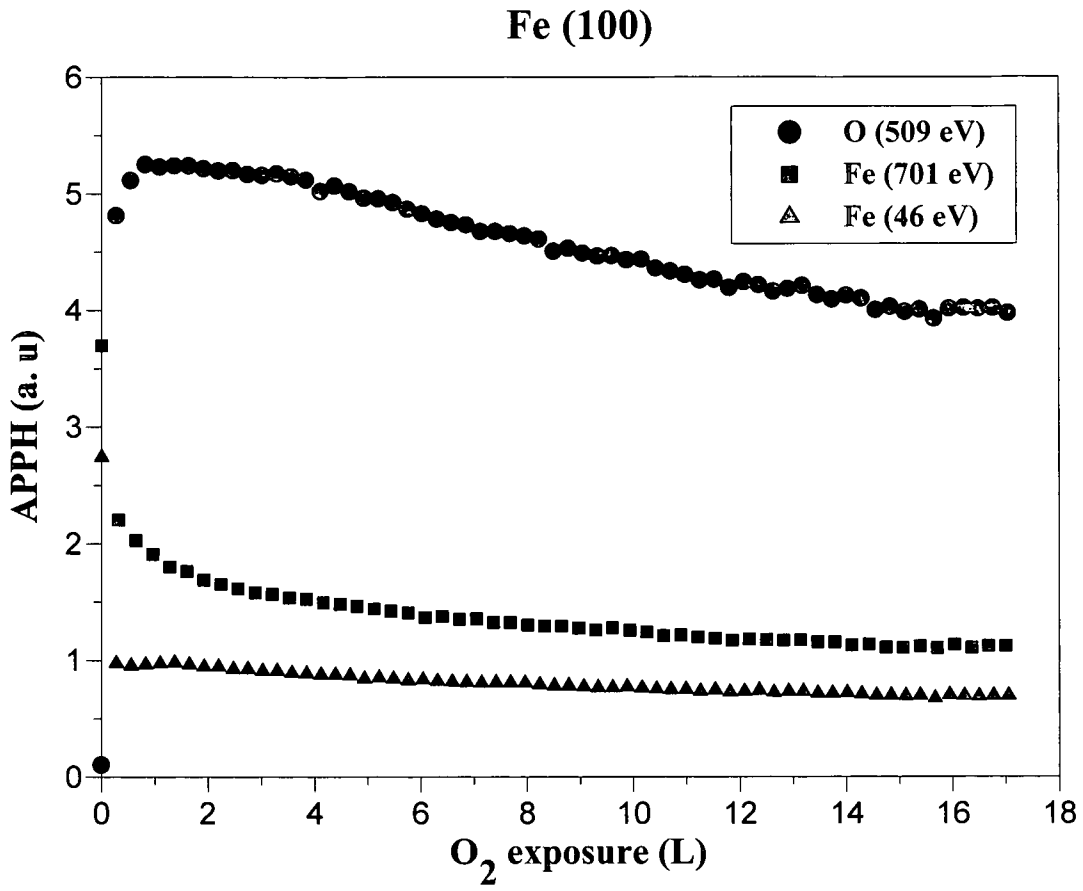

Figure 5.2: The APPH of Fe(701 eV), Fe(46 eV) and O(509 eV) vs. oxygen exposure for Fe(100) at room temperature.

The pure Fe has a low energy (M_{23} M_{45} M_{45}) peak at 46 eV while the iron oxide, Fe_2O_3, has two peaks at 42 eV and 52 eV respectively. The change in the 46 eV Fe peak to the dual peaks at 42 eV and 52 eV is characteristic of iron oxide formation. A close look at the low energy Fe peaks at different exposures, illustrated in Figure 5.3, clearly indicates the oxide formation.

The Auger spectrum taken after the oxidation (shown in Figure 5.1) indicated that there were no other elements contributing to the surface reaction. The electron beam did have a small influence in the oxidation of the Fe(100) sample. The coverage of the O on the surface of the sample was higher with the electron beam on than with the electron beam off.

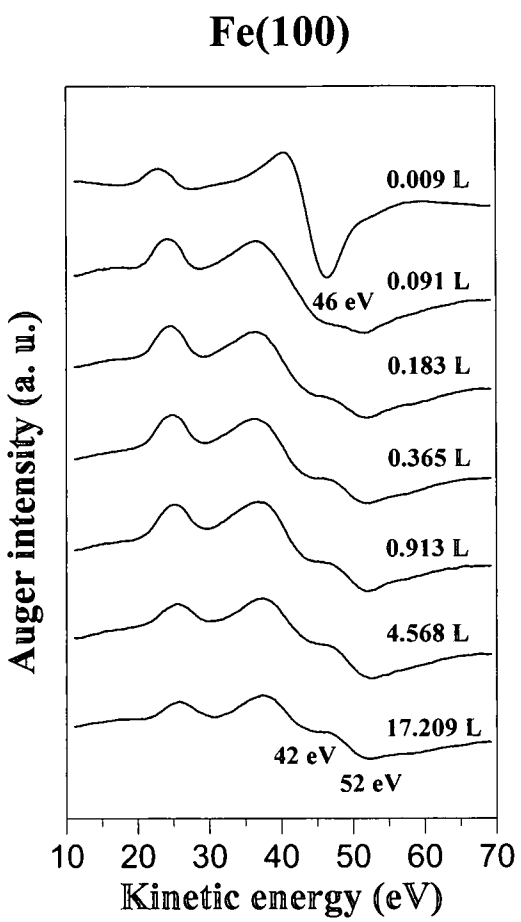

Figure 5.3: The changes in peak shape of the low energy Fe(46 eV) peak with oxygen exposure. For exposures above 0.09 L, the spectra were magnified to ease comparison.

The difference in the O APPH was approximately 10%. The higher coverage is attributed to the electron beam's contribution to dissociate the O_2 molecule. The higher reactivity of the O radicals leads to an accelerated surface reaction. Even though the electron beam has an influence in the rate and extent of the reaction it is not the sole cause of the reaction, in other words the reaction proceeds even in the absence of the electron beam.

Consider the decrease of the APPH values for the different elements in Figure 5.2. From equation 4.1 in chapter 4 it is clear that the Auger peak intensity for an element is determined by the concentration, backscattering and the escape depth of the electrons. If the assumption is made that the oxide layer increases in thickness with an increase in exposure, then the O peak height is expected to increase with an increase in oxide thickness, provided that the backscattering term stays constant.

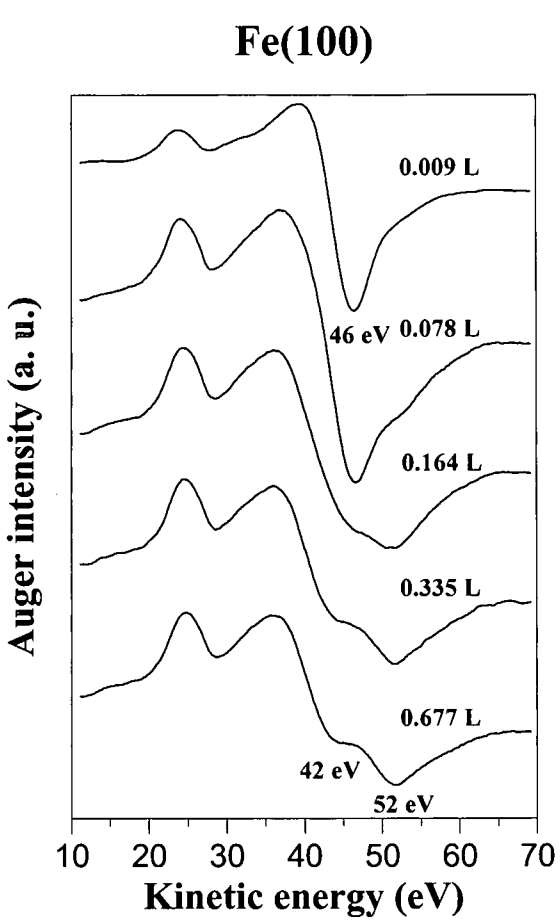

Figure 5.4: The change in the low energy AES Fe peak as a result of the oxygen exposure at 100°C. The peaks above 0.07 L exposures have been magnified with a factor two, for ease in the comparison.

The electron backscattering from the Fe substrate has a large contribution to the O peak intensity at low exposures. As the overlayer thickens, the overlayer will influence the total backscattering term. It has been shown in the calculations in chapter 4 that the backscattering for the oxide layer is less than for the Fe substrate. The contribution of the oxide to the backscattering and the O peak intensity will be more than the contribution of the Fe substrate for higher exposures. As the overlayer thickens, its contribution to the backscattering will increase, resulting in a decrease of the total backscattering term. At high exposures, the O peak intensity will thus be smaller than the peak measured at low exposures.

For the change in the APPH of the low energy Fe peak the same reasoning may be followed as for the O in the previous paragraph. The low energy Fe Auger electrons from the substrate do not contribute to the peak at high exposures due to the surface sensitivity of these electrons. At a certain overlayer thickness, the low energy Fe

Auger peak will only be generated by the Fe in the overlayer. In the profile this is indicated by the plateaux region of the low energy Fe APPH values. Another important consideration of this peak is the shape change that occurs with oxide formation. When the oxide forms, the peak shape changes, resulting in lower APPH measurements at high exposures.

The profile in Figure 5.2 also shows a decrease in value of the high energy Fe APPH. The high energy Fe electrons experience attenuation by the thickening overlayer at high exposures. Consequently, there will be fewer of the high energy Fe electrons that can pass through the overlayer to contribute to the APPH value.

5.2.2. Oxygen exposure of Fe(100) at various temperatures

The oxidations performed at 100°C and 200°C also resulted in oxide formation on the sample surface. Once again, the sample was sputter cleaned before oxygen exposure to ensure that there were no contaminants on the surface that could influence the surface reactions.

The formation of oxide on the sample surface is evident from the change in the low energy AES Fe peak shape. Figure 5.4 and Figure 5.5 show the peak changes before and after oxygen exposure for the 100°C and 200°C oxidations.

Comparison of the changes in the low energy Fe peak shapes for the 100°C and 200°C oxygen exposure clearly indicates that the rate of oxidation is higher at 100°C. It seems that the surface temperature influences the reaction. The following paragraphs describe the behaviour of the Fe(100) sample exposed to oxygen at temperatures above 200°C.

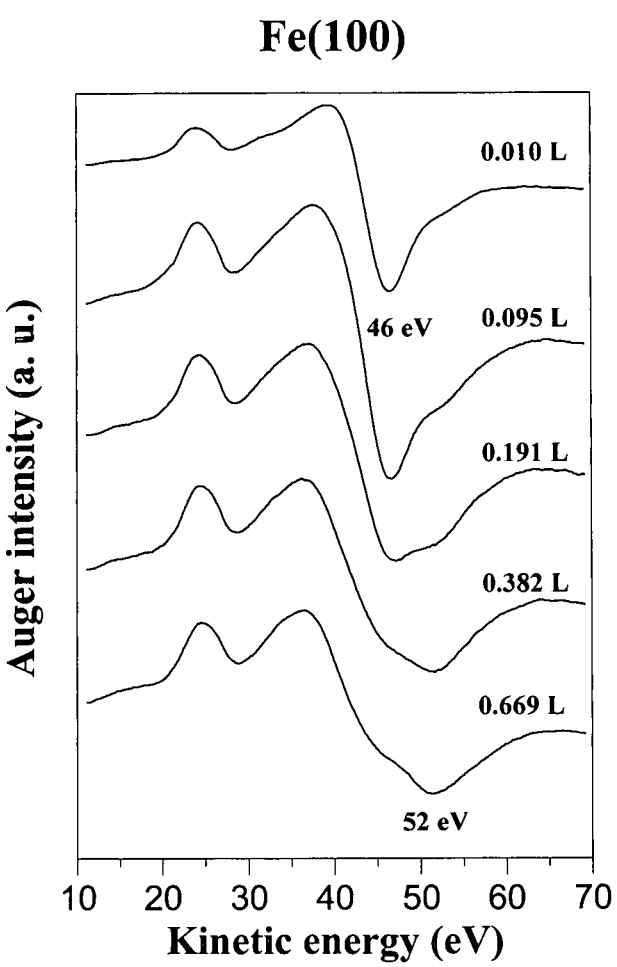

Figure 5.5: The low energy AES Fe peak changes as a result of oxygen exposure at 200°C. Peaks above 0.09 L exposures have been magnified.

Before the sample surface was exposed to the oxygen environment at 500°C it was sputter cleaned until the surface was free of contaminants. The Auger spectrum taken after sputter cleaning is illustrated in Figure 5.6. The small amount of N on the sample surface was due to the presence of nitrogen in the residual gases and not a contaminant in the bulk of the sample.

The APPH for the relevant peaks vs. exposure, for the oxygen exposure at 500°C, is illustrated in Figure 5.7. The graph indicates rapid adsorption of the O on the sample surface, but with lower surface coverage than for the room temperature exposure. Figure 5.8 illustrates the peak shape of the low energy Fe peak at various exposures. There was no change in the peak shape and thus it can be concluded that there was no oxide formation on the sample surface.

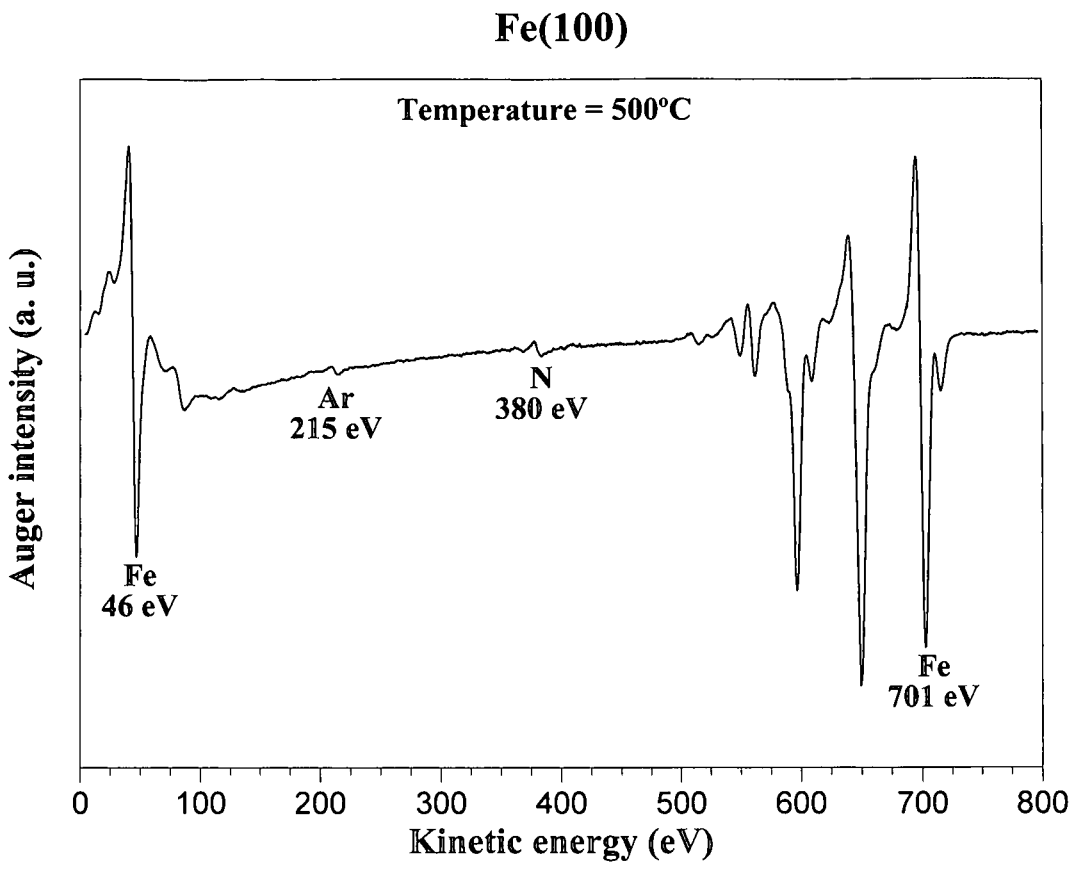

Figure 5.6: The AES spectra of the Fe(100) sample taken after sputter cleaning at 500°C.

The oxygen exposures performed at temperatures above 300°C all showed the same behaviour as described above for the 500°C oxidation. A plot of the surface coverage versus temperature, given in Figure 5.9, indicates the influence of temperature on the oxygen coverage for the Fe(100) sample after 0.5 L oxygen exposure.

The oxygen coverage is a function of the oxygen sticking coefficient as described in chapter 2. The sticking coefficient, however, is a function of temperature and decreases with an increase in temperature. It is thus expected that the temperature will have an influence on the oxygen coverage of the sample surface.

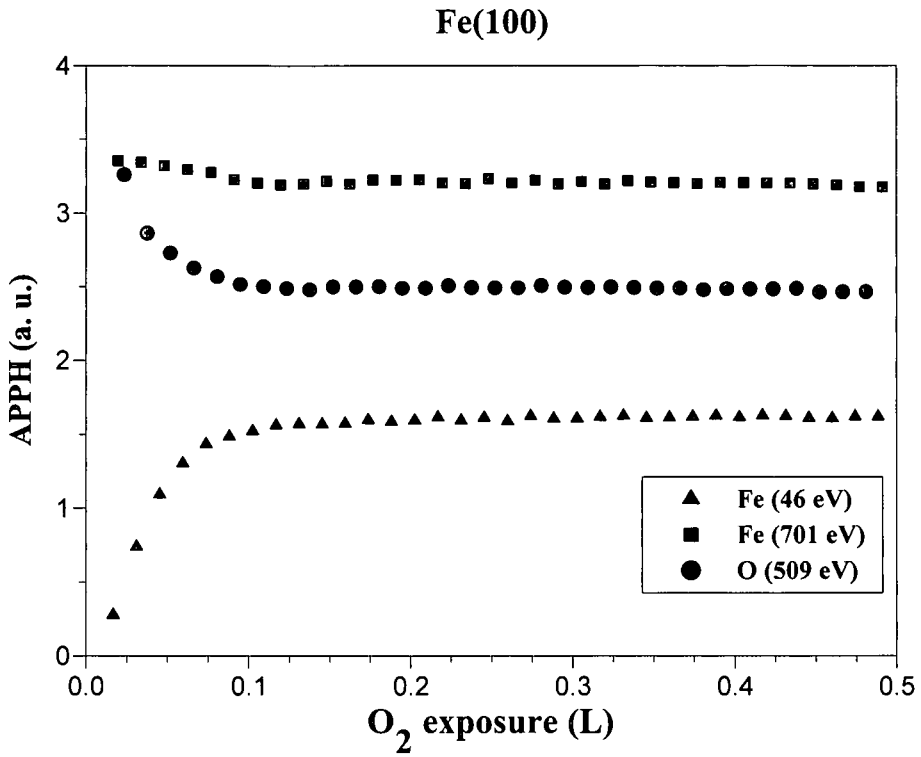

Figure 5.7: The APPH of the Fe(46 eV), Fe(701 eV) and O(509 eV) peaks vs. oxygen exposure for the Fe(100) sample at 500°C

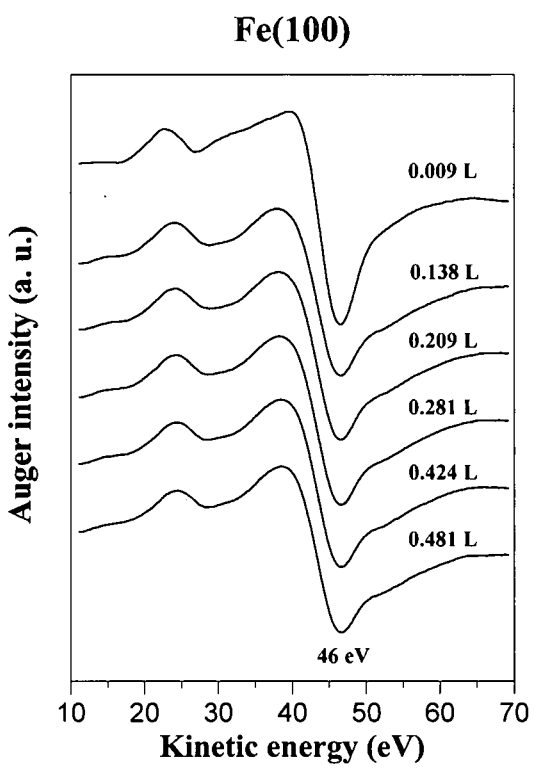

Figure 5.8: The low energy AES Fe peak for various oxygen exposures at 500°C. Although there was a change in intensity of the peaks there were no changes in the peak shapes to indicate oxide formation.

The higher surface temperature results in a decrease of the sticking coefficient of the oxygen on the sample surface. The O will not remain on the surface long enough to react chemically with the Fe before desorption. The plateaux region of the O in Figure 5.7 indicates equilibrium between the adsorption and desorption of O on the sample surface.

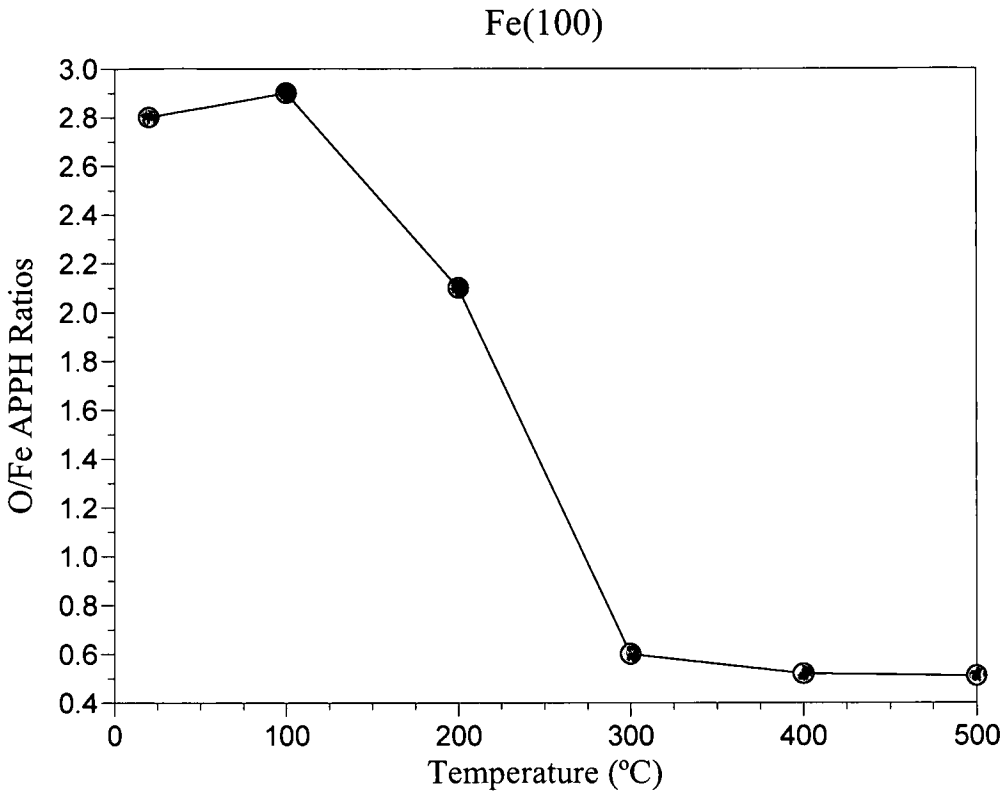

Figure 5.9: The effect of temperature on oxygen surface coverage after 0.55 L oxygen exposure of the Fe(100) sample.

5.2.3. A summary of the oxidation behaviour of Fe(100)

The Fe(100) sample reacts rapidly with the oxygen environment at room temperature to form an iron oxide surface compound. Associated with the oxide thickening is a decrease in the O APPH because of the difference in the backscattering terms of the Fe substrate and the oxide overlayer. The low energy Fe APPH reaches a plateaux after 0.25 L exposure, the electrons that primarily contribute to this peak originate from the oxide layer and not from the substrate. The low energy Fe peak has a change in shape associated with the oxide formation. The Fe peak with 46 eV kinetic energy changes upon oxide formation to form two peaks at 42 eV and 52 eV respectively.

The high energy Fe electrons experience attenuation by the oxide overlayer causing the steady decline in the APPH values for the Fe(701 eV) peak with further exposure.

At 100°C and 200°C there is also oxide formation, but the extent of the oxide formation decreases with an increase in temperature. At temperatures above 300°C there is no oxide formation and an equilibrium between the adsorption and desorption of O on the sample surface is reached after 0.1 L oxygen exposure.

The surface coverage is a function of the sticking coefficient and consequently also a function of the temperature. The similarities in the exposures of the sample above 300°C can be attributed to the relation between the oxygen coverage and the temperature.

5.3. Mo(100) oxygen exposure

The Mo(100) sample was exposed to the oxygen environment at room temperature to determine the oxidation behaviour of the Mo. An Auger spectrum, illustrated in Figure 5.10, taken after sputter cleaning the sample indicated that there were no contaminants on the surface before oxygen exposure.

The APPH of the relevant elements as a function of exposure, given in Figure 5.11, showed low O surface coverage compared to the coverage obtained with the Fe(100) sample at room temperature. The Mo peaks also reflect the chemical environment of the Mo. If the Mo reacts chemically with the O environment the shift and shape changes in the Mo AES peaks will reflect the change in the chemical environment of the Mo [12]. The Mo AES peaks did not undergo any shifts or shape changes, as illustrated in Figure 5.12, indicating that there was no change in the chemical environment of the Mo. The Mo is thus inert to the oxygen environment at room temperature and the O that is detected on the sample surface is simply adsorbed on the surface.

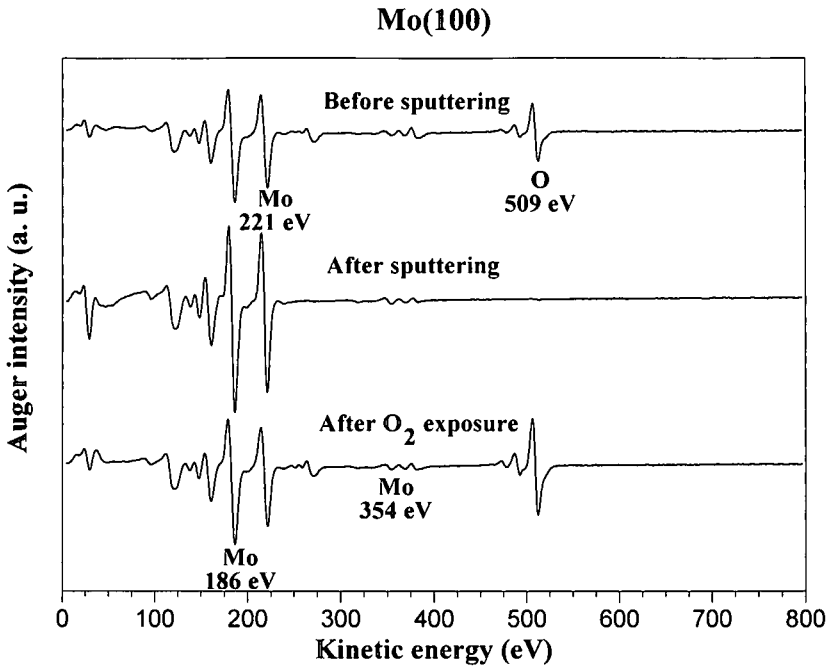

Figure 5.10: The AES spectra of Mo(100) taken before and after sputter cleaning and after oxygen exposure.

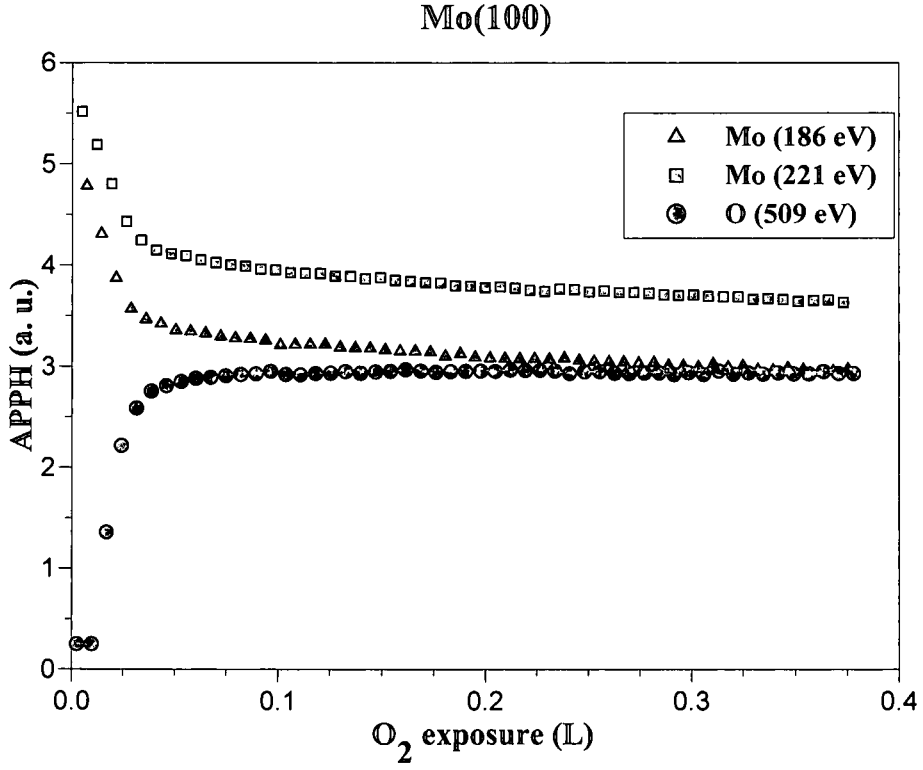

Figure 5.11: The APPH of the Mo(25 eV), Mo(221 eV) and the O(509 eV) vs. exposure for Mo(100) at room temperature.

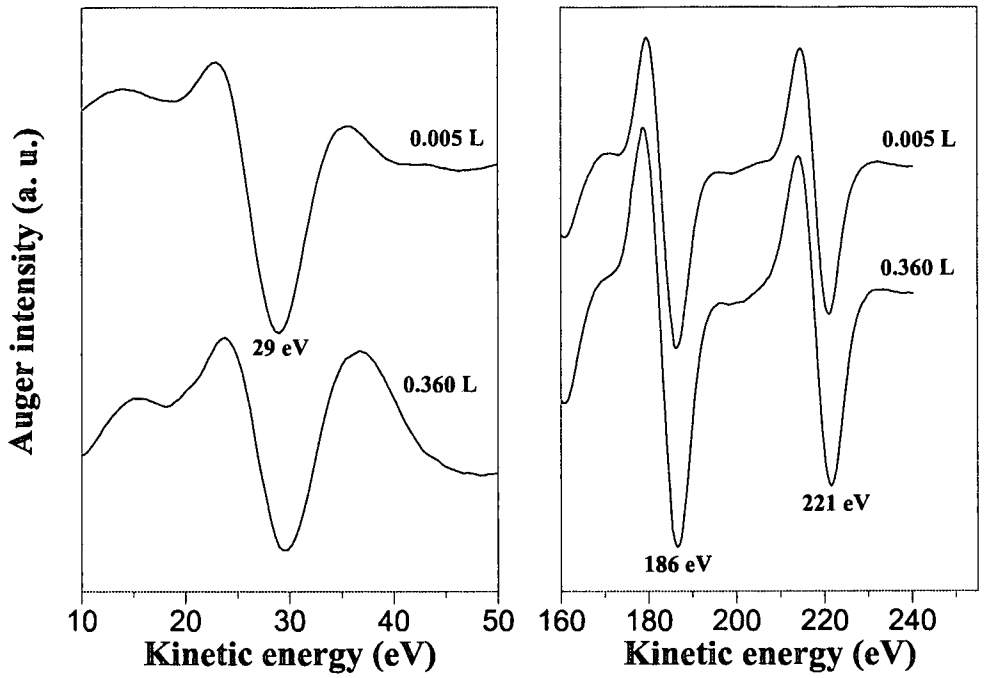

Figure 5.12: The Mo(100) peaks taken before and after oxidation.

5.4. Fe(100)-3.5wt% Mo-N oxygen exposure

5.4.1. Room temperature oxygen exposure

Before the sample was exposed to the oxygen environment it was sputter cleaned to remove surface contaminants. The AES spectrum, given in Figure 5.13, was taken before and after sputter cleaning the sample and also indicates the spectrum taken after oxygen exposure.

After sputter cleaning only a small quantity of Mo was detected on the sample surface. There was also a very small quantity of O and N detected on the sample surface. Apart from the Fe, Mo, N and O there were no other elements detected on the sample surface.

After the sputter cleaning the sample was exposed to the oxygen environment at room temperature for several hours.

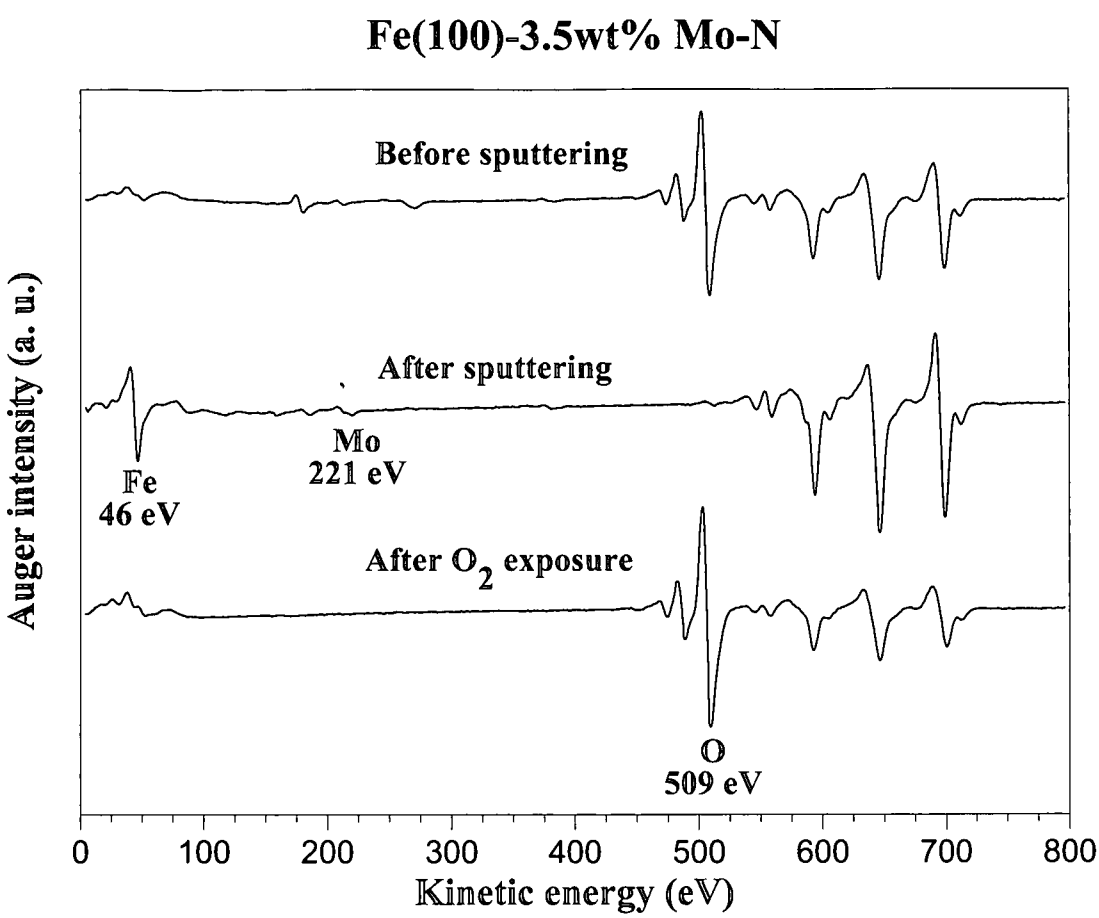

Figure 5.13: The AES spectra of the Fe(100)-3.5wt% Mo-N sample taken before and after sputter cleaning as well as the spectrum taken after O_2 exposure.

The APPH for the relevant peaks as a function of the exposure, given in Figure 5.14, shows the same oxidation trend as for the Fe(100) sample. The first 1 L exposure is characterised by a sharp increase in the O APPH and a sudden decrease in both the high and low energy Fe APPH values. The O APPH reaches a maximum value at 1 L and with further exposure the APPH values for the O declines steadily. A similar decline is seen in the APPH values for the high energy Fe, whereas the low energy Fe APPH values reach a plateaux after 1 L exposure. The reasons for these occurrences are the same as for the Fe(100) sample, as described in subsection 5.2.1.

The Fe that is exposed to the oxygen reacts readily to form iron oxide. This is clearly indicated by the changes in the low energy AES Fe peak illustrated in Figure 5.15.

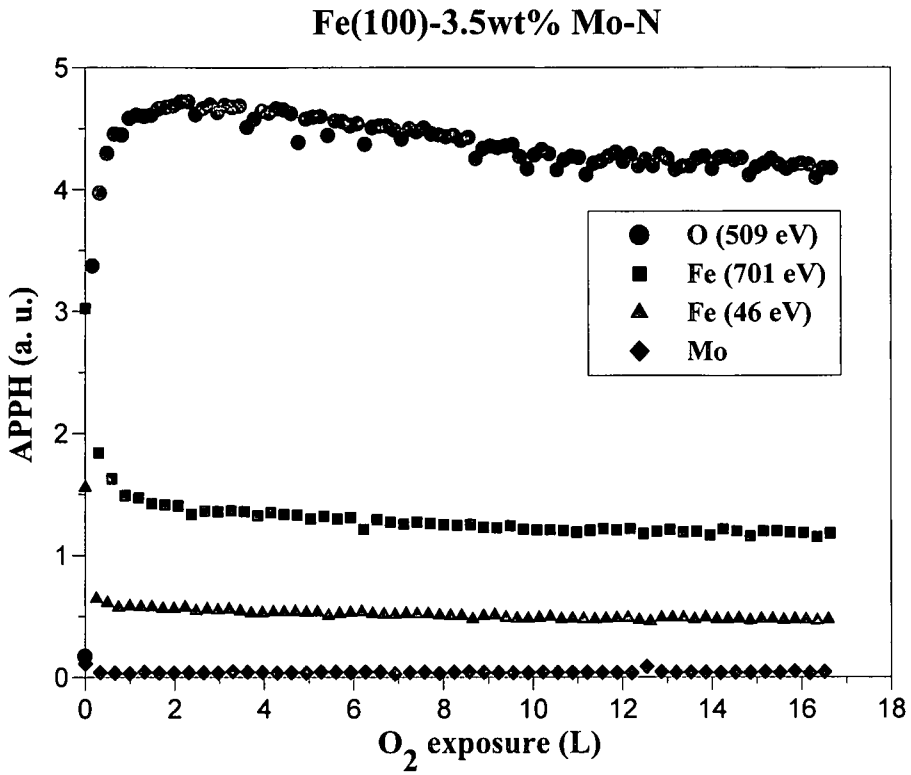

Figure 5.14: The APPH of the Fe(46 eV), Fe(701 eV), O(509 eV) and the Mo(186 eV) vs. oxygen exposure for Fe(100)- 3.5 wt% Mo-N alloy at room temperature.

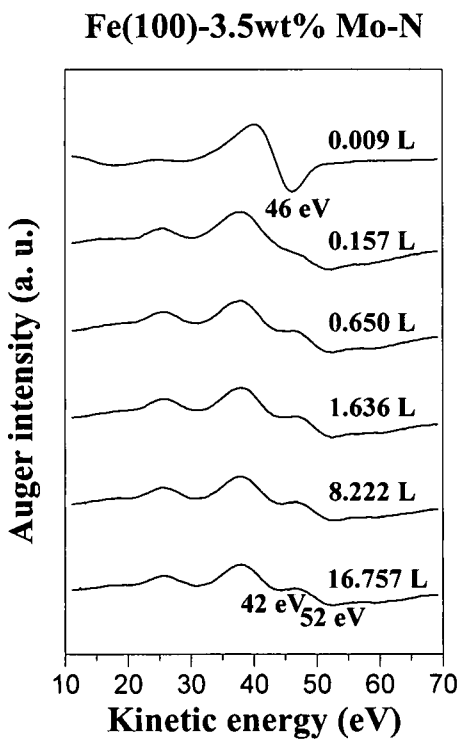

Figure 5.15: The changes in the low energy Fe peak during oxidation. For exposures above 0.157 L the peaks were magnified to ease the comparisons.

At room temperature the electron beam, as with the Fe(100) sample, had an influence on the oxidation of the sample. As with the Fe(100) oxidation the electron beam did not initiate the reaction although it did accelerate it.

5.4.2. Oxygen exposure at various temperatures

The sample was sputter cleaned before oxygen exposure to remove surface contaminants as for the previous exposures. The oxygen exposures performed at 100°C and 200°C showed a difference in oxidation behaviour. The respective profiles are illustrated in Figure 5.16 and 5.17.

There is a clear difference in the APPH of O for the 100°C and 200°C O_2 exposures. The exposure at 100°C has the same increase in O APPH and decrease in the high energy Fe APPH as for the room temperature exposure. The O surface coverage obtained at 100°C is noticeably less than the coverage for the room temperature exposure as reflected by the maximum O APPH values.

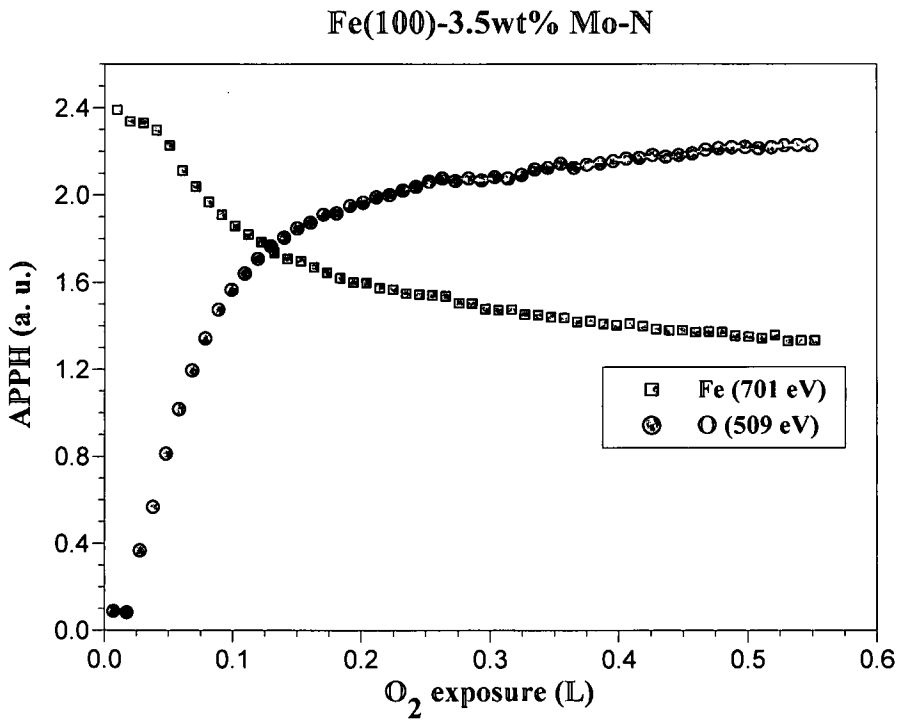

Figure 5.16. The APPH vs. exposure for Fe(100)-3.5wt% Mo-N at 100°C.

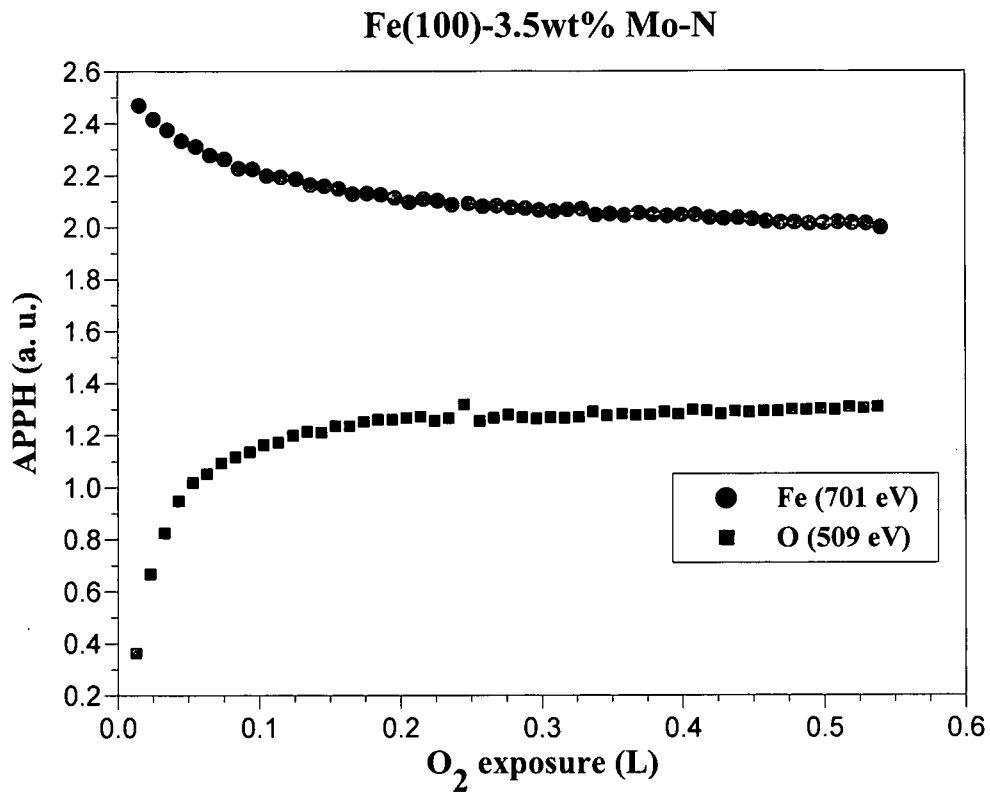

Figure 5.17. The APPH vs. exposure for Fe(100)-3.5wt% Mo-N at 200°C.

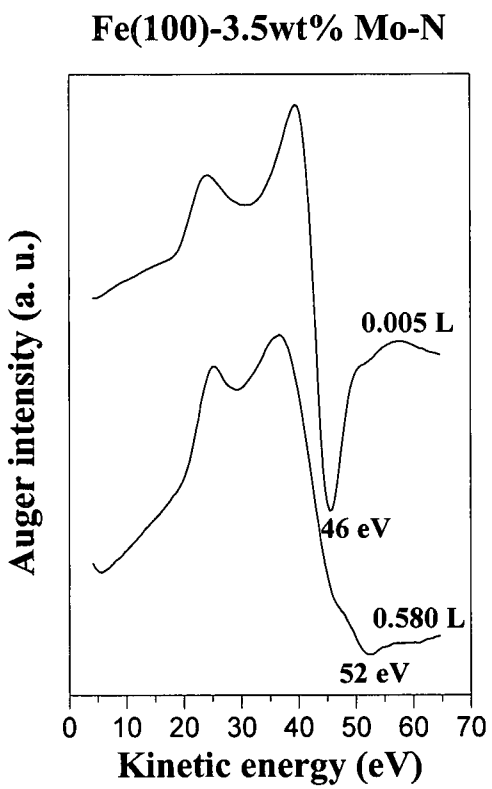

Figure 5.18. The peak changes of the low energy AES Fe peak for the 100°C oxygen exposure. The peak taken at 0.580 L was magnified.

At 200°C there is an even lower surface coverage compared to the exposure performed at 100°C. The coverage reaches a maximum value after 0.18 L exposure. The exposure up to 0.18 L is characterised by an increase in the O APPH and a decrease in the high energy Fe APPH. After the 0.18 L exposure there is no further change in the rate at which the O APPH increases or the Fe APPH decreases. The decrease in the high energy Fe APPH can be attributed to attenuation of the intensity of the high energy Fe Auger electrons that escape from the sample, by the overlayer.

A closer look at the peak changes for the low energy AES Fe peak for the 100°C exposure indicates that there is some oxide formation at 100°C. Compared to the peak changes for room temperature exposure the extent of oxidation is less at the elevated temperature. For the 200°C exposure there is only a small shift in the low energy Fe peak, indicating that there was no oxide formation. The alloy elements thus have a definite influence on the oxidation behaviour of the Fe.

The oxygen exposure of the Fe(100) sample at 200°C showed some oxide formation while the alloy had no oxide formation at the same temperature.

Figure 5.20 illustrates the low energy Fe Auger peak before and after the oxygen exposure at 300°C. Again, there was no change in the shape of the peak to indicate oxide formation.

The oxygen exposures performed at temperatures above 200°C all showed the same behaviour. There was a lower O coverage on the sample surface at the elevated temperatures compared to the oxidation performed at room temperature. At temperatures above 200°C there was no oxide formation only O adsorption.

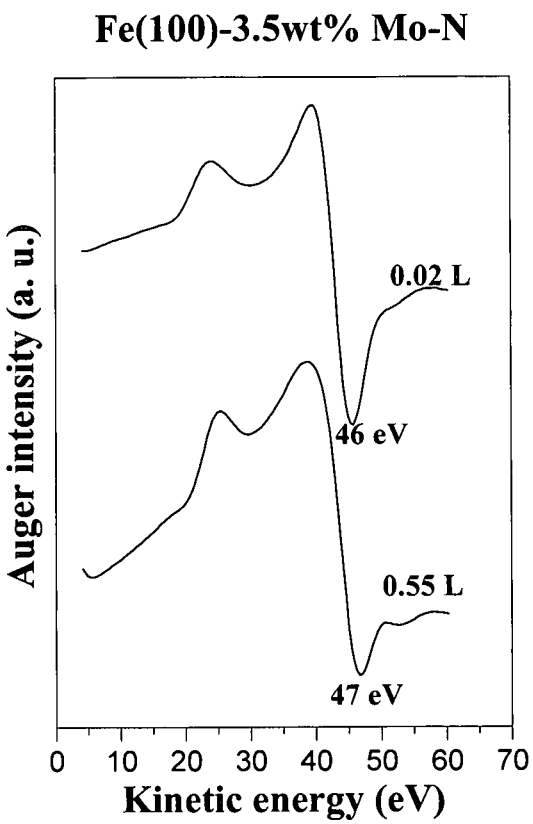

Figure 5.19. The peak changes of the low energy AES Fe peak for the 200°C oxygen exposure.

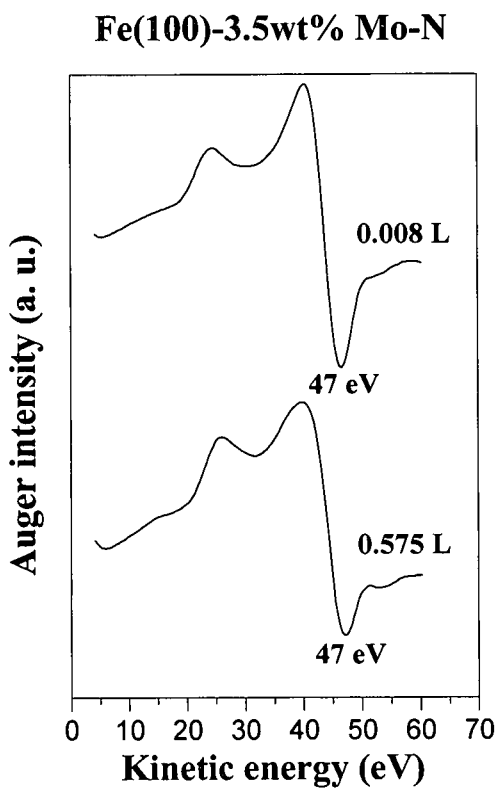

Figure 5.20: The low energy AES Fe peak before and after oxygen exposure at 300°C.

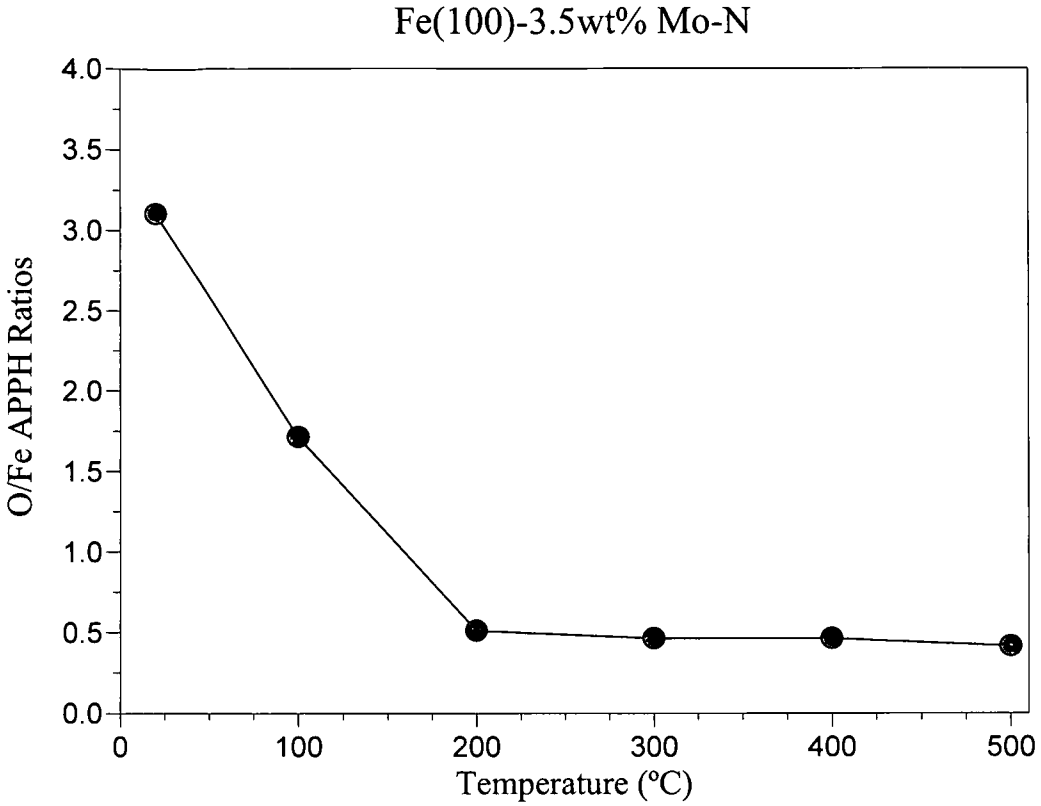

Figure 5.21: The influence of temperature on the O/Fe ratios at equilibrium.

5.4.3. A summary of the Fe(100)-3.5wt%Mo-N oxidation behaviour

The Fe(100)-3.5wt%Mo-N sample reacts readily with the oxygen environment at room temperature to form an iron oxide on the sample surface. The surface O coverage at 1 L exposure is less for the alloy than for the Fe(100) sample as a result of the alloy elements in the sample. The general trend for the alloy oxidation, however, is similar to the Fe(100) oxidation.

For the alloy a more significant influence on the surface reactions was noticed for elevated temperatures than for the Fe(100) sample. At temperatures of 200°C and above no oxide formation was detected.

5.5. The oxygen exposure of the segregated MoN layer

5.5.1. LTR segregation of Mo and N

Before the segregation was initiated the sample was sputter cleaned to remove surface contaminants. Figure 5.22 illustrates the AES spectrum taken after sputter cleaning.

LTR segregation, as described in chapter 3, was performed to form the stable MoN layer on the surface of the sample. Along with the Mo and N, there was also C segregation. It is clear from the APPH vs. temperature profile, given in Figure 5.23, that the C segregation did not prohibit the segregation of the Mo and N. The AES spectra of the N peak at various temperatures inserted in Figure 5.23 does not prove the formation of the MoN. The Mo also has a small peak at 354 eV that starts to contribute to the N APPH after 400°C. This results in the continued increase in the N APPH as the Mo starts to segregate and thus contributes more to the N APPH.

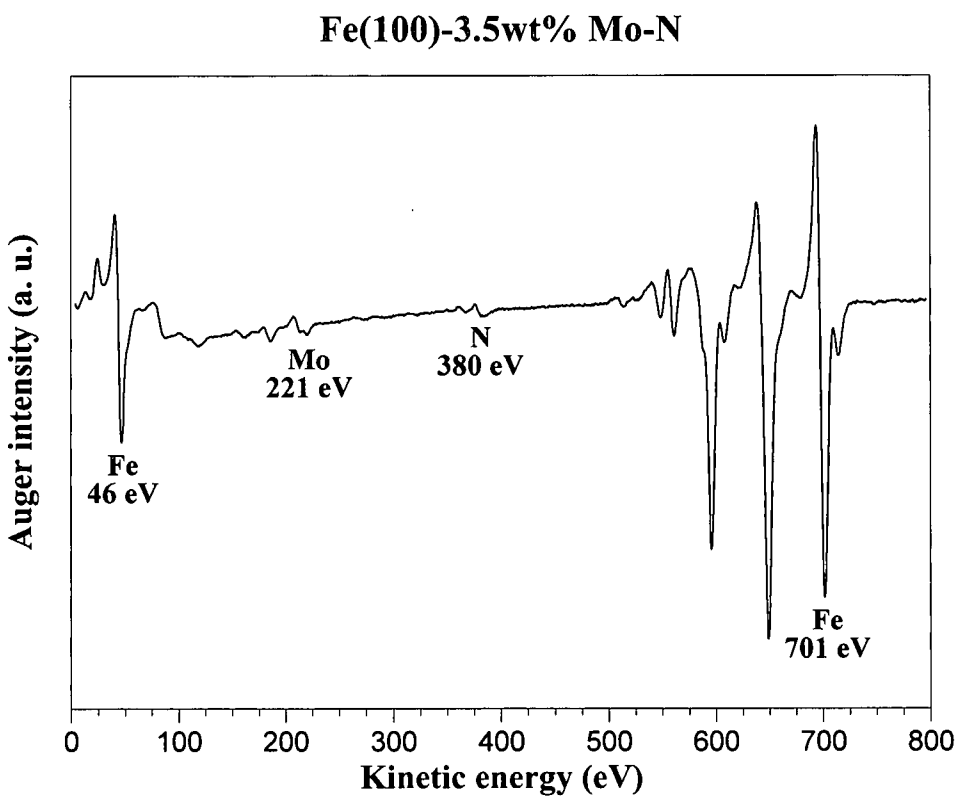

Figure 5.22: The AES spectrum taken after sputter cleaning.

The AES spectrum, shown in Figure 5.24,taken after the segregation indicates the increase of the Mo, N, and C on the sample surface. A comparison of this spectrum with one taken of the Mo_2N powder sample, as illustrated in Figure 5.24, indicates that the Mo and N that segregated to the surface do not form an Mo_2N compound as the relative height of the Mo and N peaks in the segregated compound is different to those for the Mo_2N sample. There is more N in the segregated specie than in the Mo_2N standard. It is thus assumed that the surface compound is MoN in accordance with other research groups [2].

The MoN surface compound was stable with an increase in temperature up to 550°C and when cooled to room temperature.

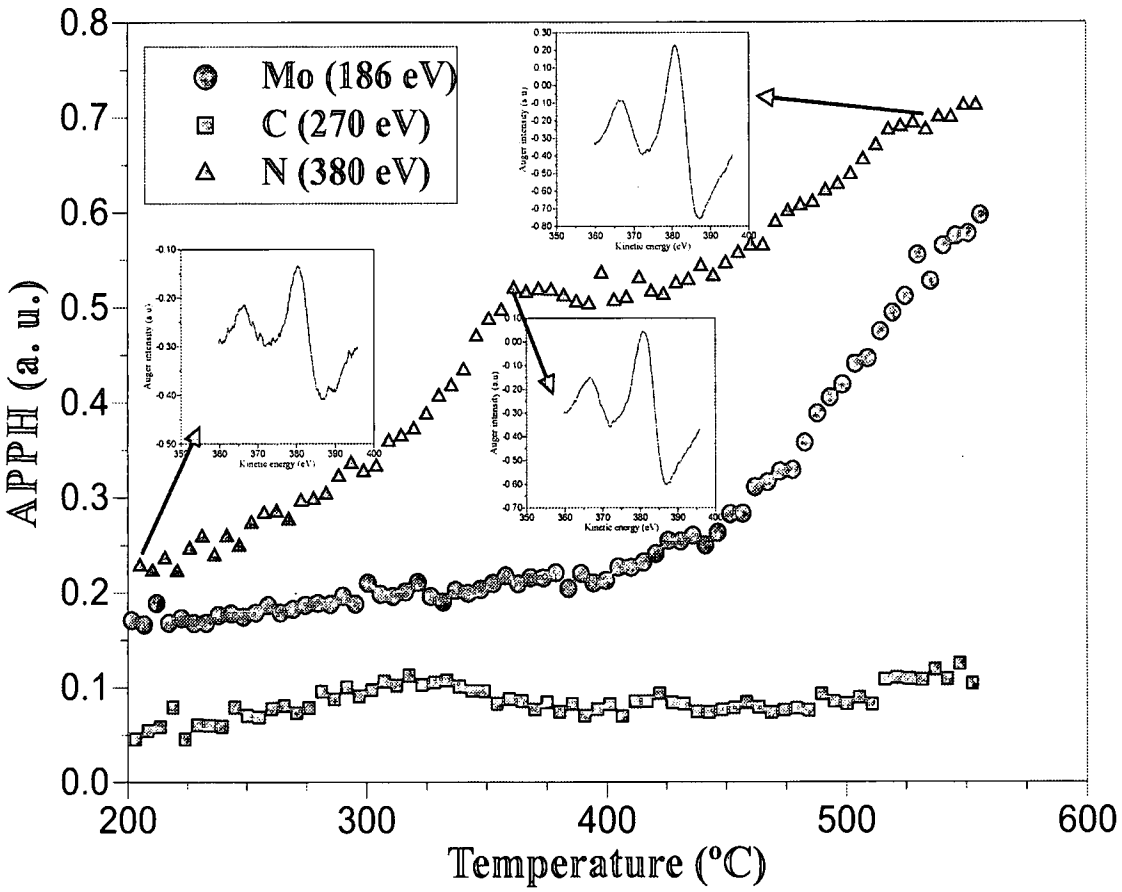

Figure 5.23: The APPH as a function of temperature for the LTR segregation of the Fe(100)-3.5wt%Mo-N sample.

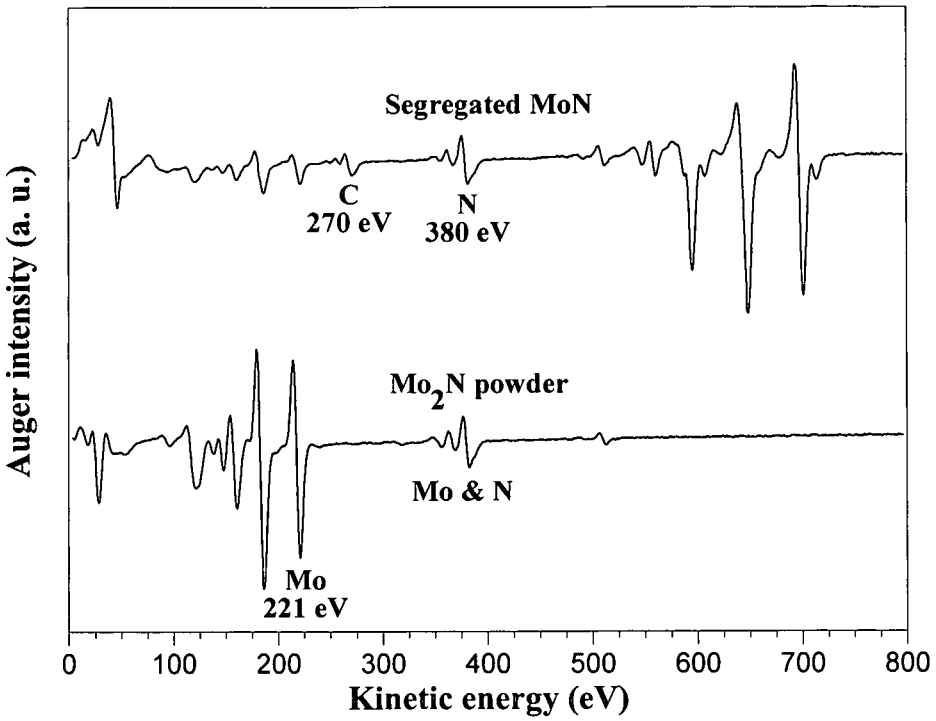

Figure 5.24: The AES spectrum of the segregated MoN and the Mo_2N standard.

5.5.2. Oxygen exposure at various temperatures

After each LTR segregation the sample was exposed to oxygen at various temperatures. The APPH for the relative peaks as a function of the exposure for the 100°C exposure is illustrated in Figure 5.25. The characteristic decrease in the Fe APPH values with exposure and the increase in the O APPH values is, once again, a result of the overlayer thickening. At 100°C the O coverage on the sample surface after exposure was considerably less than for the Fe(100)-3.5wt% Mo-N sample. The segregated layer therefore has an inhibiting effect on the surface reaction. The APPH values for the Mo, N and C decrease rapidly as the sample surface is exposed to the O. Figure 5.26 illustrates the low energy AES Fe peak before and after the oxidation of the segregated layer. There was more iron oxide formation after oxygen exposure on the Fe(100) and the Fe(100)- 3.5wt% Mo-N samples at 100°C than on the segregated layer at 100°C as is evident from the oxide to metal ratio in Figure 5.4 and Figure 5.18.

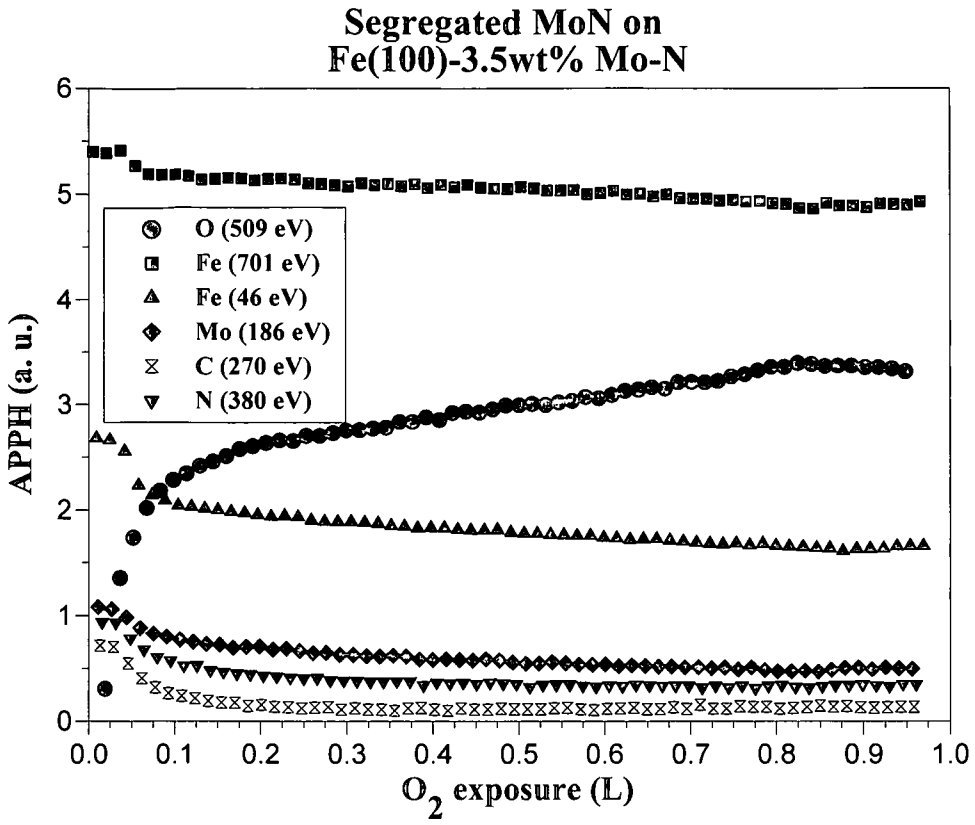

Figure 5.25: Oxygen exposure of the segregated layer at 100°C.

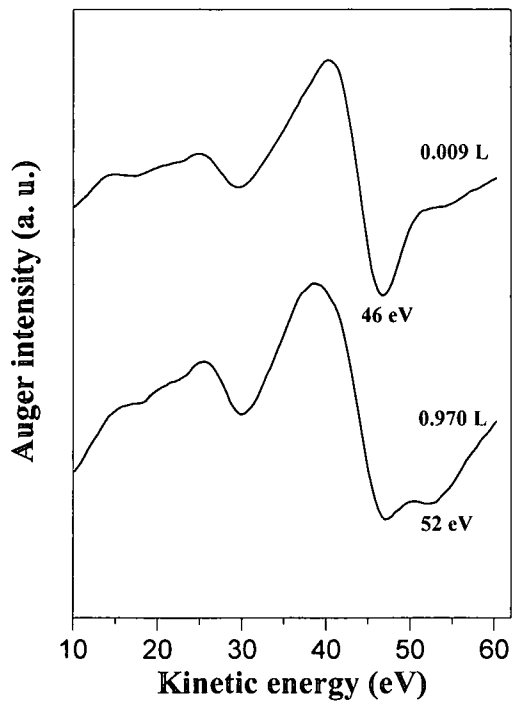

Figure 5.26: The low energy AES Fe peak before and after the oxygen exposure of the segregated MoN layer at 100°C.

The surface exposure at 200°C resulted in a lower O surface coverage compared to the 100°C exposure. The APPH for the different peaks as a function of the exposure is illustrated in Figure 5.27. Compare the changes in the low energy Fe AES peaks for the 100°C and 200°C exposures. The peak changes for the 200°C exposure indicate that there was less oxide formation at 200°C. The low energy Fe peak, for the 200°C oxygen exposure, taken before and after the oxygen exposure is illustrated in Figure 5.28. The oxygen exposure at 300°C showed similar behaviour as the exposure at 200°C.

There were no differences in the behaviour of the segregated layer to the oxygen exposures at 400°C and 500°C. At these temperatures there was no significant change in the shape of the low energy Fe peak, illustrated in Figure 5.29, indicating that there was very little or no chemical reaction between the Fe and adsorbed O. At the elevated temperatures equilibrium between adsorption and desorption of oxygen on the sample surface was attained rapidly.

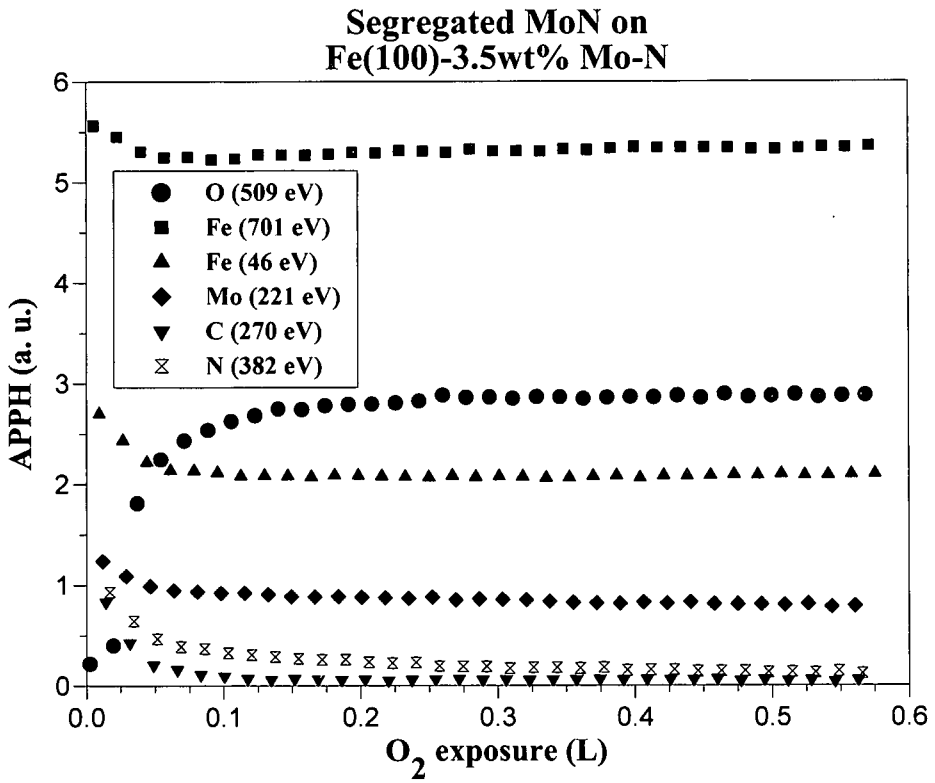

Figure 5.27: The APPH for the various elements vs. oxygen exposure for the oxygen exposure of the segregated layer at 200°C.

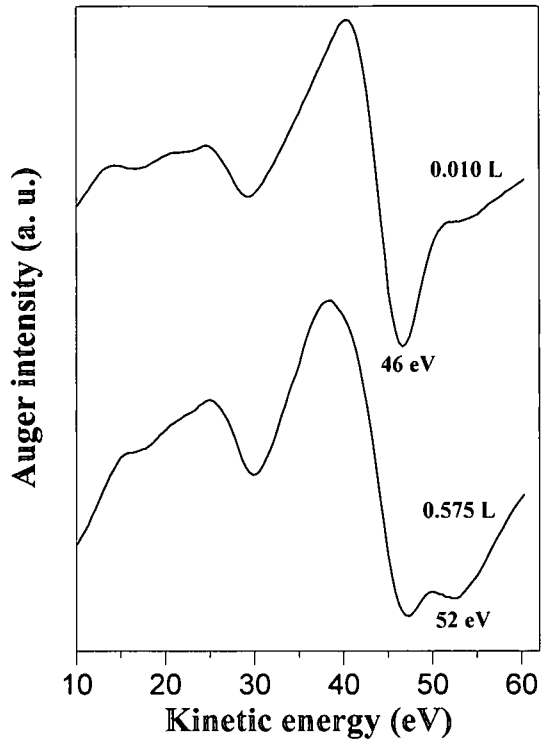

Figure 5.28: The low energy AES Fe peak before and after oxygen exposure at 200°C.

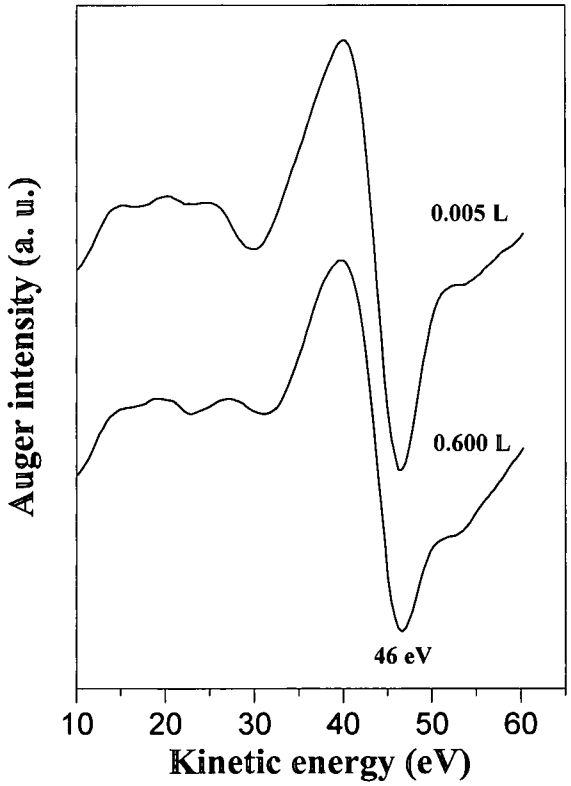

Figure 5.29: The low energy Fe peak before and after oxygen exposure at 500°C.

5.5.3. Room temperature oxygen exposure

As with the other oxygen exposures the sample surface was sputter cleaned before the LTR segregation to remove surface contaminants. The LTR segregation resulted in a stable MoN surface layer. The sample was exposed to the oxygen environment for several hours. Figure 5.30 illustrates the AES spectra taken after the LTR segregation and after the oxidation, while Figure 5.31 illustrates the relative APPH for the various peaks as a function of the exposure.

The oxidation behaviour of the segregated layer differs considerably from the behaviour of the Fe(100) sample and the Fe(100)-3.5wt%Mo-N sample. The O APPH vs. oxygen exposure for the Fe(100) and for the Fe(100)-3.5wt% Mo-N samples were logarithmic but the O APPH vs. exposure for the segregated layer clearly shows non-logarithmic behaviour.

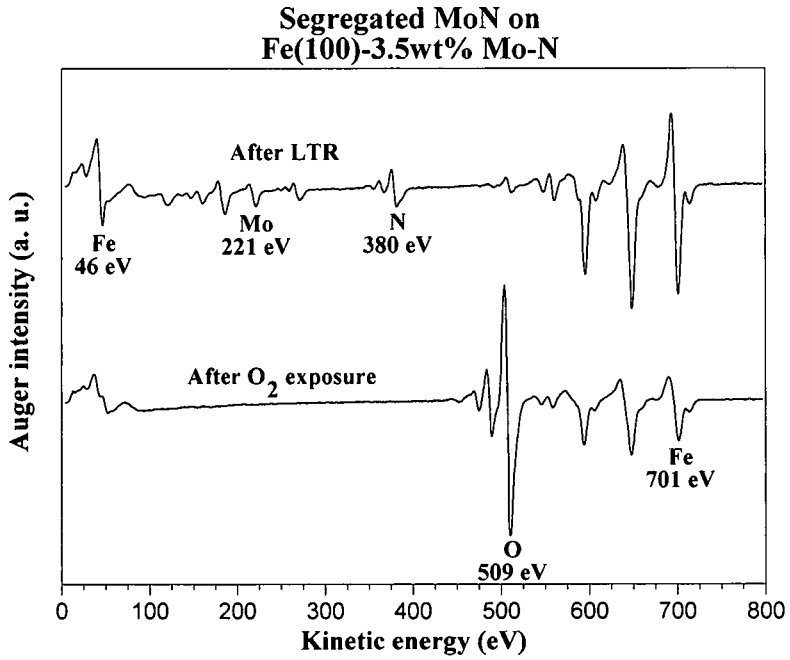

Figure 5.30: The AES spectra taken after LTR segregation and after the room temperature oxygen exposure.

The APPH vs. oxygen exposure for the segregated MoN layer can be divided into three sections, A (0 - 0.4 L), B (0.4 – 3.5 L) and C (3.5 – 13 L). In section A, there is a sharp increase in the O APPH values and a related decrease in the APPH values for

the low and high energy Fe peaks and also for the Mo, N and C APPH values. Initially the O that is detected on the sample surface is in the adsorbed state. The low energy AES Fe peak, illustrated in Figure 5.32(a), indicates that there is some oxide formation detectable after 0.24 L exposure.

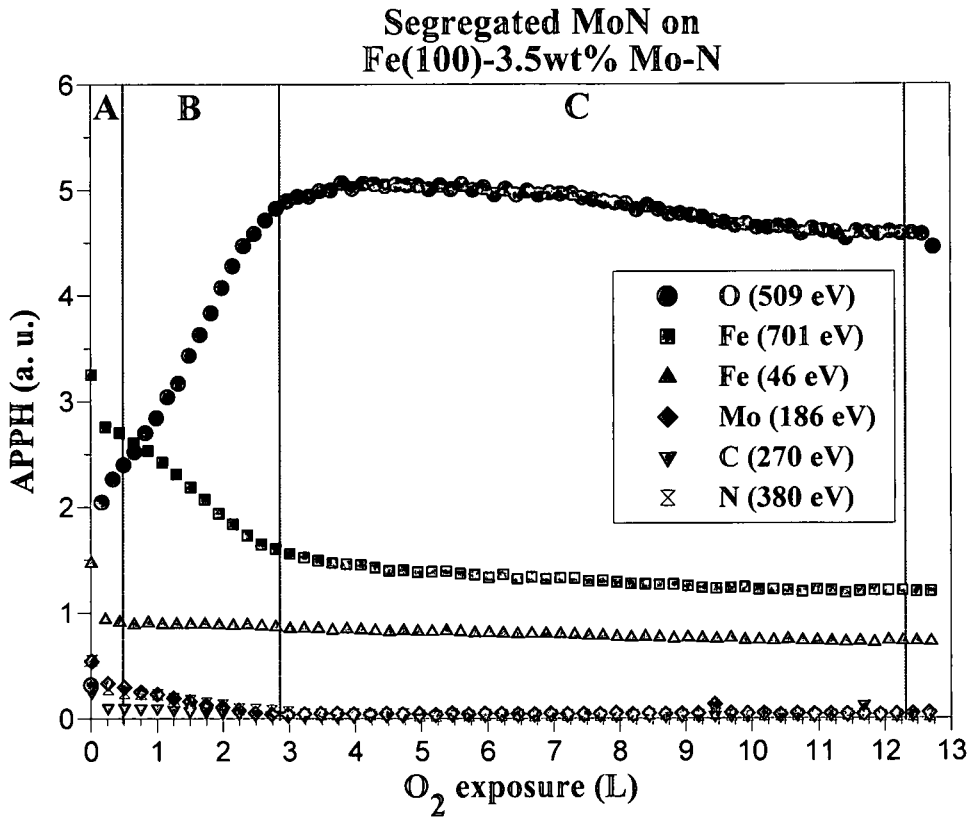

Figure 5.31: The APPH of the various elements vs. oxygen exposure for the segregated MoN layer at room temperature.

Section B shows a decrease in the rate at which O APPH values increases. This rate is maintained up to 2.75 L oxygen exposure. The APPH values for the low energy Fe peak remain constant above 0.5 L oxygen exposure. The APPH values for the high energy Fe decrease rapidly up to 2.75 L oxygen exposure. Above 2.75 L oxygen exposure the rate of decrease for the high energy Fe APPH values changes to a steady decline. The low energy Fe peak shape continues to change in section B indicating the continued formation of iron oxide in this section. The change in the low energy Fe peak is illustrated in Figure 5.32(b).

The oxygen exposures higher than 2.75 L are depicted by section C. Initially there is a sharp increase in the O APPH values in section A changing to a decrease in the APPH values in section C with an increase in the oxygen exposure. Above 2.75 L exposure

the O APPH values follow the same trend as for the Fe(100) and Fe(100)-3.5wt% Mo-N samples. As in the other samples there is a steady decline in the O APPH values with an increase in the oxygen exposure. The reason for this decline is due to the increase in the oxide thickness as described in subsection 5.2.1. The shape of the low energy Fe peak continues to change, as illustrated in Figure 5.32(b), and this indicates the continued oxide formation with further oxygen exposure.

It is clear from the experimental results that the segregated layer has a significant influence on the oxidation behaviour of the sample. The formulation of a hypothesis is utilised to interpret the experimental results. The hypothesis is illustrated in Figure 5.33

Assume that the MoN layer that forms on the sample via the LTR segregation is a perforated layer. Due to the perforated nature of the layer there is still some exposed Fe on the sample surface. Upon oxygen exposure the oxygen adsorbs on the exposed Fe on the sample surface. The Fe thus acts as active sites on the sample surface. This occurs in section A in Figure 5.31.

With continued exposure, depicted by section B in Figure 5.31, the Fe reacts chemically with the adsorbed oxygen to form iron oxide. The iron oxide grows rapidly to form MoN–oxide boundaries. Following the formation of boundaries the rate of O adsorption will change resulting in a change in the O APPH with exposure. The O that adsorbs on the MoN on the sample surface remains inactive when adsorbed in low quantities, because of the relative inert nature of the Mo as seen in the oxidation of the Mo(100) sample. With further exposure the O coverage on the MoN grains increases. The higher O coverage on the MoN results in the dissociation of the MoN. The N and O react to form a volatile N_xO_y compound that desorbs from the surface, in agreement with previous studies [5]. Further increase in the O surface coverage, most probably leads to the formation of volatile MoO_3, which also desorbs from the surface. The Mo-O phase diagram in chapter 2 confirms the formation of the volatile MoO_3, at high O surface coverage. Upon desorption of the N_xO_y and the MoO_3, the Fe underneath the MoN layer will be exposed to the oxygen and the exposed Fe will react readily with the oxygen environment.

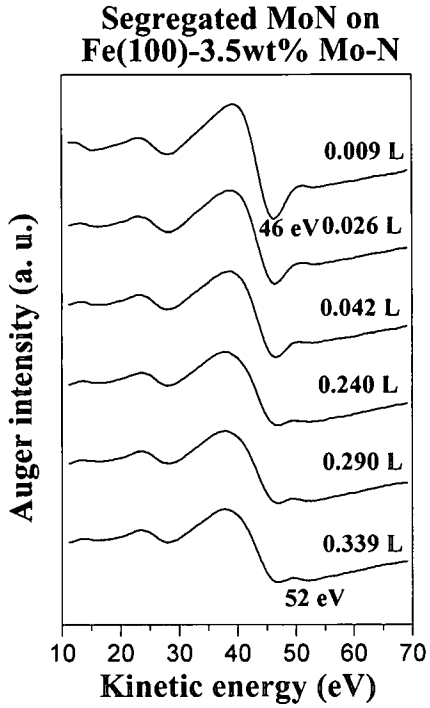

Figure 5.32 (a): The low energy AES Fe peak changes during oxidation at room temperature for section A in Figure 5.31.

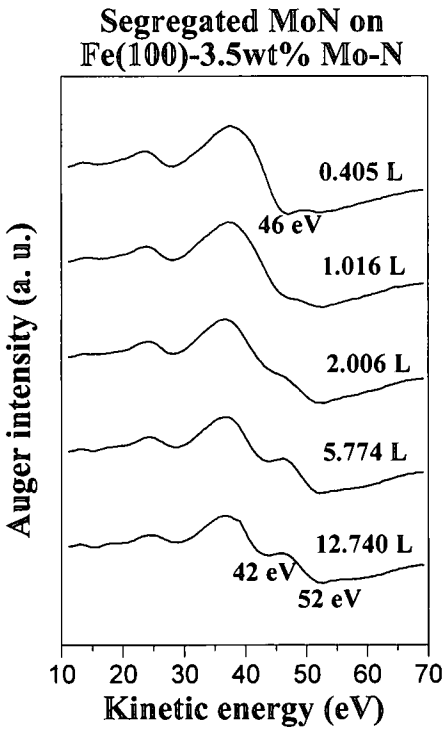

Figure 5.32(b): The low energy AES Fe peak changes during oxidation at room temperature for sections B and C in Figure 5.31.

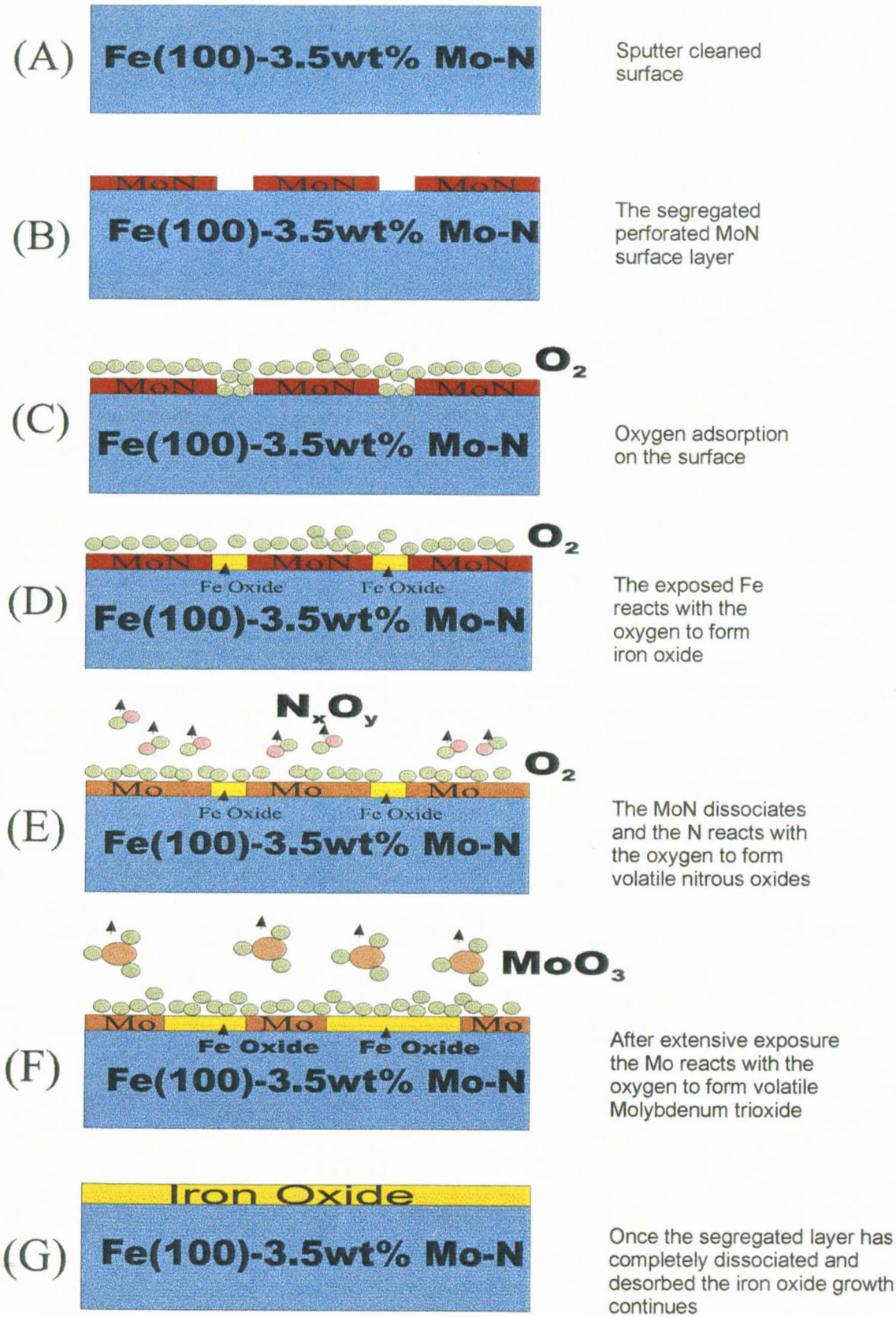

Figure 5.33: A schematic representation of the hypothesis.

The rate of iron oxide formation will be dependent on the rate at which the MoN dissociates, and the reaction time for the formation of the volatile species. The O APPH values in section B will only be a reflection of the O that adsorbs and reacts with the Fe since the oxygen that reacts with the N and the Mo will desorb as compounds from the sample surface. This is indicated by the linear increase of the O APPH values with exposure in section B. The MoN layer will have dissociated and desorbed completely after 2.75 L oxygen exposure. In section C there is no more MoN on the sample surface and the iron oxide will continue to grow in thickness resulting in the steady decline of the O APPH values with further exposure. The decline of the O APPH values after 2.75 L exposure is due to the thickening of the oxide layer as seen for both the Fe(100) and the Fe(100)-3.5wt% Mo-N samples.

After 24 hours exposure to the oxygen environment a depth profile, as described in chapter 3, was taken. This profile is illustrated in Figure 5.34.

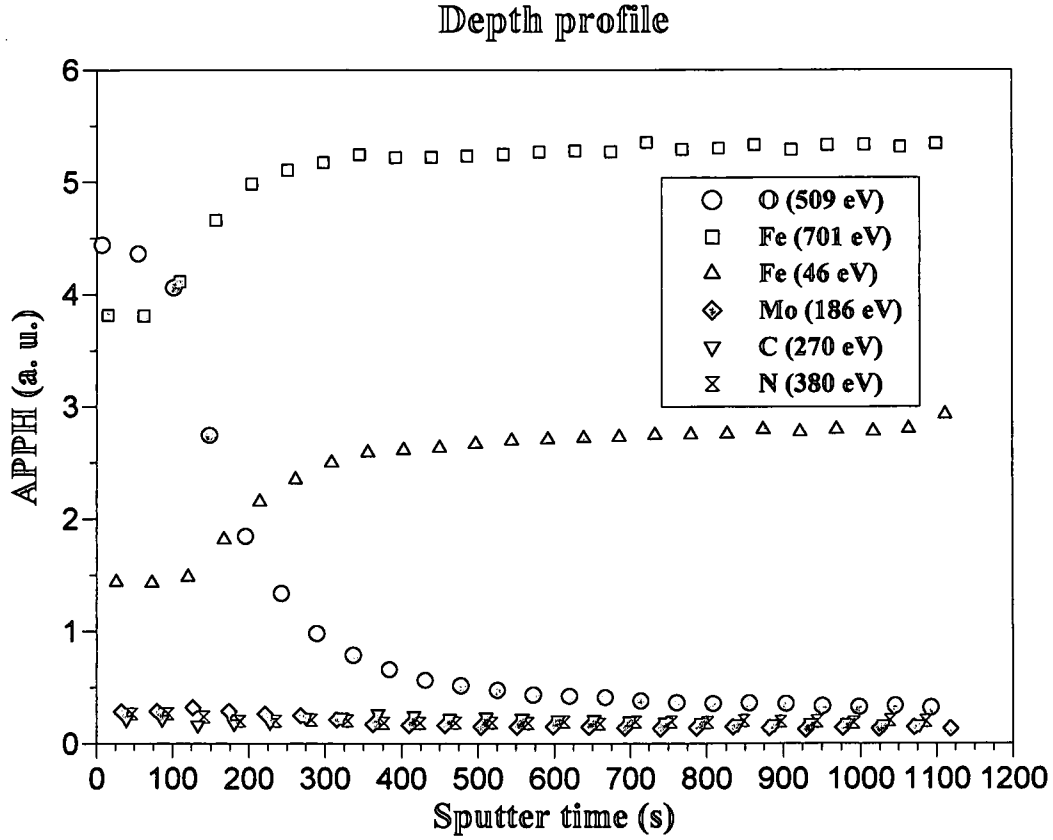

Figure 5.34: The depth profile of the oxidised MoN layer on the Fe(100)-3.5wt% Mo-N specimen taken after 24 hours oxygen exposure.

There is no Mo or N enrichment detected underneath the oxide on the sample surface. This supports the hypothesis that the Mo and N desorb as oxygen compounds from the sample surface.

Figure 5.35 illustrates the desorption profile that was taken during the first stages of oxygen exposure of the segregated layer. As the oxygen is leaked into the chamber the partial pressure of the O_2 increases. The inlet of the O_2 results in an increase in the partial pressures of the background gasses. The increase is attributed to the inlet of background gasses along with the O_2 and the collision of the O_2 with the walls of the chamber resulting in desorption of the adsorbed residual gasses. There is no significant change in the partial pressure of the nitrous oxides (N_xO_y) or the Molybdenum trioxide. Although there were no gaseous Mo or N compounds detected it does not eliminate the possibility of their formation.

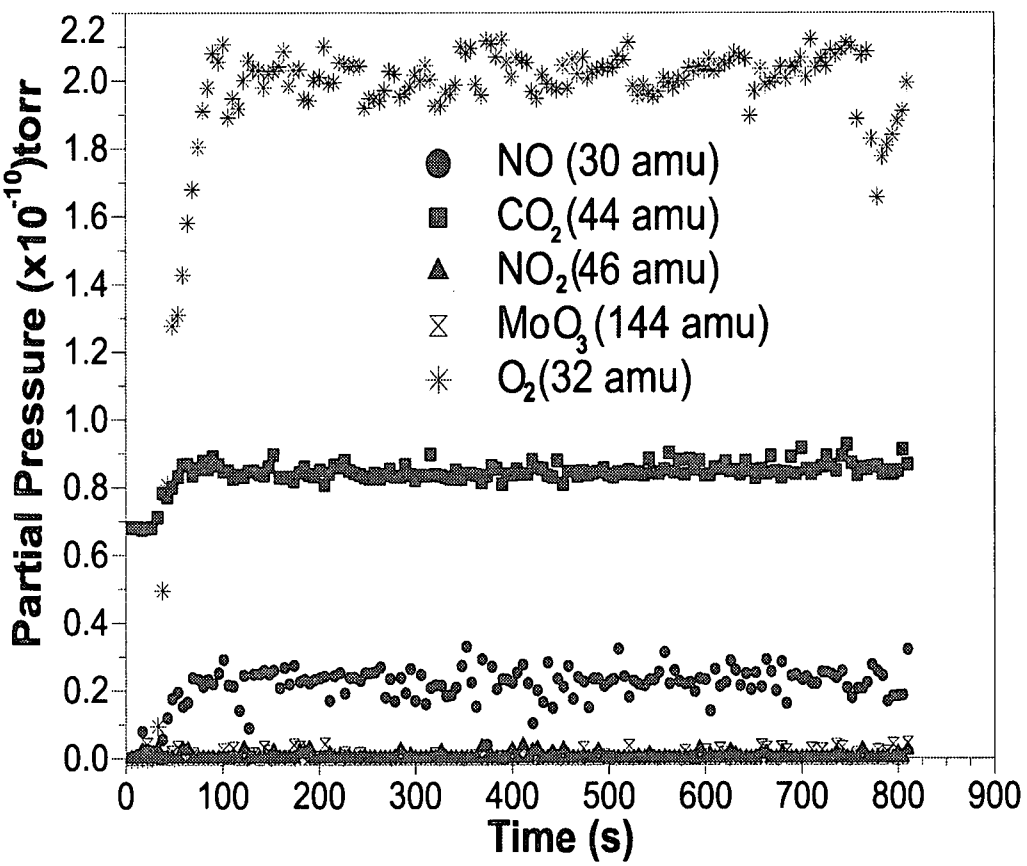

Figure 5.35: The desorption profile taken during the initial stages of oxygen exposure of the segregated layer.

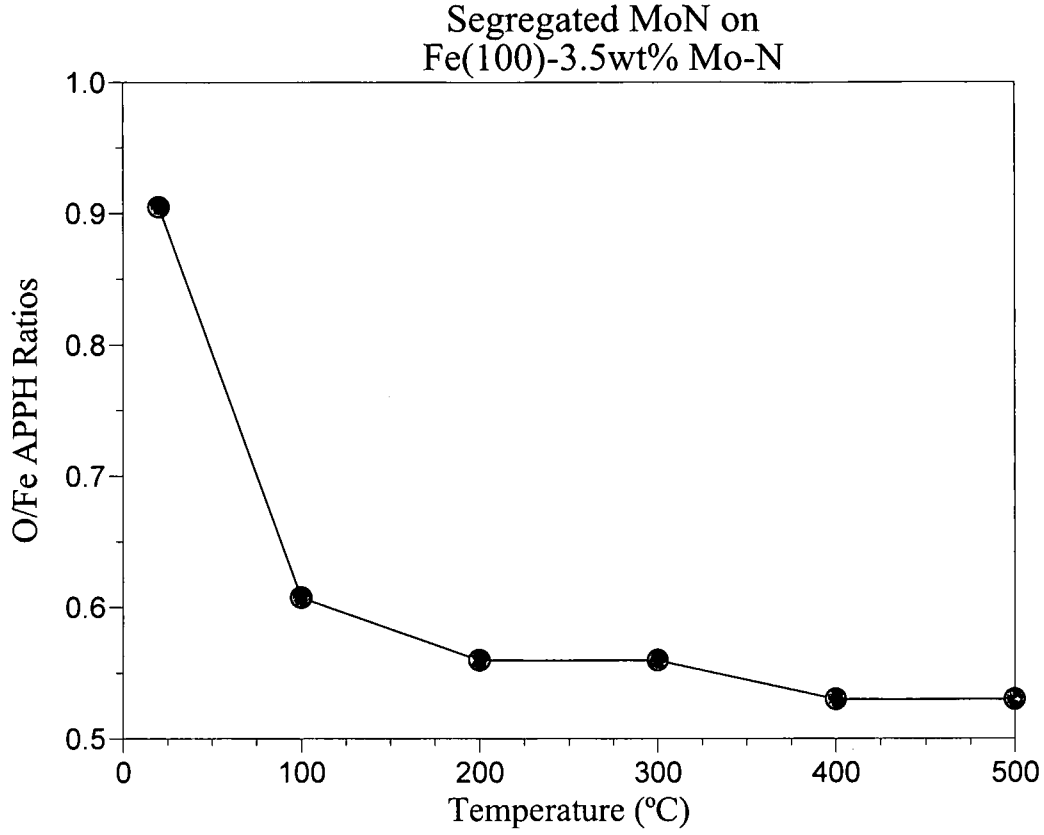

F

igure 5.36: The effect of temperature on the oxygen surface coverage for 0.55L oxygen exposure of the segregated MoN layer on the Fe(100)-3.5wt% Mo-N specimen.

5.5.4. A summary of the oxidation behaviour of the segregated MoN layer on the Fe(100)-3.5wt%Mo-N sample

At room temperature the segregated layer had a significant influence on the oxidation of the sample surface. It is evident from the experimental results that the segregated layer has an inhibiting effect on the rate of the surface reaction. The perforated MoN layer that forms on the surface dissociates with extensive exposure to form volatile MoO_3 and N_xO_y compounds. With an increase in the surface temperature there is also a decrease in the O surface coverage. At 100°C the extent of the oxidation is less and the O surface coverage is less than for the room temperature oxidation. Oxygen exposure of the sample at 200°C and 300°C showed similar behaviour. For these temperatures there is a lower surface coverage, compared to the 100°C and room temperature exposures and there is less oxide formation.

The oxygen exposure at 400°C and 500°C showed similar behaviour. At these temperatures there is a lower surface coverage compared to 200°C exposure and there is no oxide formation.

Figure 5.36 illustrates the influence of temperature on the surface coverage. As with the other specimens the O/Fe ratios decrease with an increase in the temperature.

5.6. Summary of the room temperature oxygen exposures

- The Fe(100) sample reacts rapidly with the oxygen environment at room temperature. The reaction rate is logarithmic. After 1 L exposure the O APPH values decline steadily as a result of the thickening of the iron oxide surface layer. The formation of iron oxide is confirmed by the change in the low energy Fe peak shape.
- The Mo(100) sample does not react chemically with the oxygen environment and the increase in the O APPH values with exposure is due to O adsorption on the sample surface.
- The Fe(100)-3.5wt% Mo-N sample shows similar behaviour to the oxygen environment as the Fe(100) sample. The primary difference is in the O APPH values after 1 L exposure. The O APPH values on the Fe(100) sample are higher than the O APPH values on the Fe(100)-3.5wt% Mo-N sample. As in the Fe(100) sample the change in the low energy Fe peak indicates the formation of iron oxide.
- The MoN layer on the Fe(100)-3.5wt% Mo-N sample influences the rate at which the Fe reacts with the oxygen environment. Although the layer decreases the rate of the iron oxide formation it does not affect the maximum O surface coverage.

The next chapter will focus on the oxidation behaviour of the Fe(100) sample and the Fe(100)-3.5wt% Mo-N sample with and without the segregated MoN layer at room temperature.

Chapter 6

Mathematical analysis of experimental results

6.1. Introduction

The room temperature oxygen exposures of the Fe(100) and the Fe(100)-3.5wt% Mo-N specimen with and without the segregated MoN layer proved particularly interesting. The calculations discussed in chapter 4 can be applied to the experimental results and these calculations will be presented and interpreted in this chapter.

6.2. Linear Least Squares Method

It has been shown that the low energy AES Fe (46 eV) peak undergoes shape changes when the Fe reacts chemically with oxygen to form iron oxide. The iron oxide has two characteristic peaks at 42 eV and 52 eV respectively. The linear least squares method, described in chapter 4, can be utilised to calculate the fraction metal and oxide contributing to a measured peak. By applying this method to all the low energy AES Fe peaks measured to obtain the APPH vs. oxygen exposure graphs, it is possible to determine the oxide formation as a function of the exposure time.

The linear least squares method makes use of a Fe and an oxide standard to perform the fits. The standard is defined as the peak measured at an infinite thickness. For the Fe standard the peak measured at 0 L exposure is used. The oxide standard, however, is more complicated. Since it is not known when the oxide layer is of "infinite" thickness, it was necessary to normalise the measured peaks. The last peak measured in the exposure run was taken and the intensity of the peak was normalised to the calculated $\frac{R_{ox}}{R_{Fe}}$ backscattering ratios. The normalised peak was used as the oxide standard. Due to possible instrumentation variance each of the oxidations had its own set of standards.

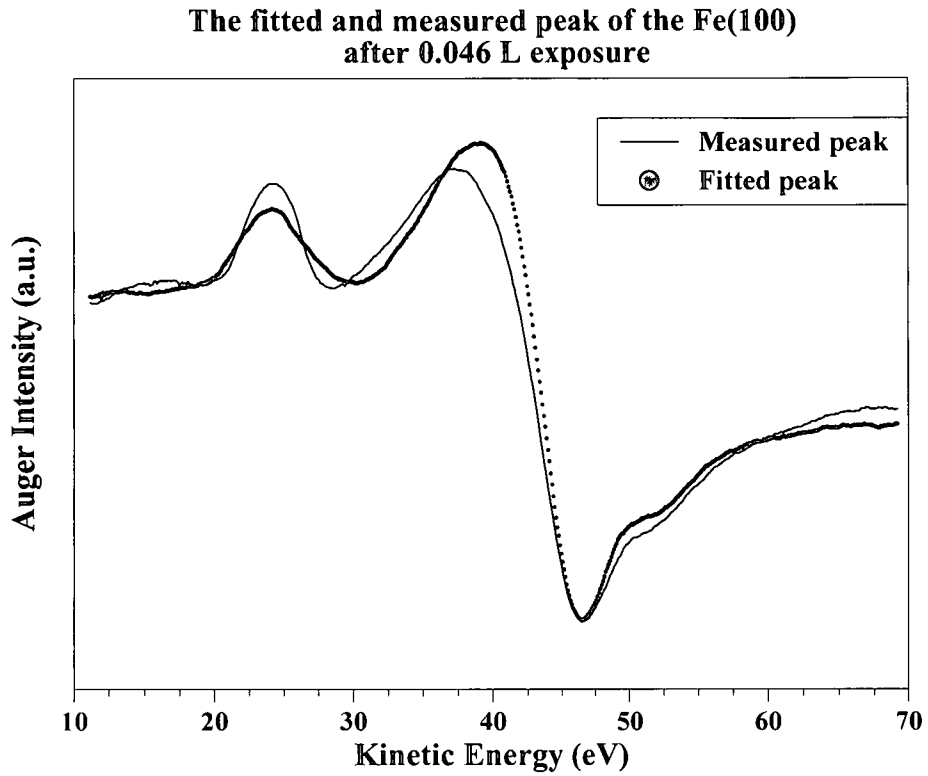

Figure 6.1: The measured and fitted peak for the Fe(100) sample after 0.046 L exposure.

6.2.1. Fe(100)

The linear least squares method is applied to determine the fraction oxide and metal contributing to the measured peaks. The peaks measured at 0.046 L and 5.025 L exposure are analysed using the linear least square method. The fraction metal and oxide in the peak is extracted and Figure 6.1 and Figure 6.2 show the calculated and the measured peaks for the two exposures.

The error for the two fits is shown in Figure 6.3 and Figure 6.4. From these graphs it is clear that there is one unique combination of oxide and metal that fit the measured peak with the smallest error.

The linear least squares method can be applied to all the peaks measured during the oxygen exposure to give the oxide formation as a function of the exposure time. Figure 6.5 illustrates the oxide formation as a function of the exposure time.

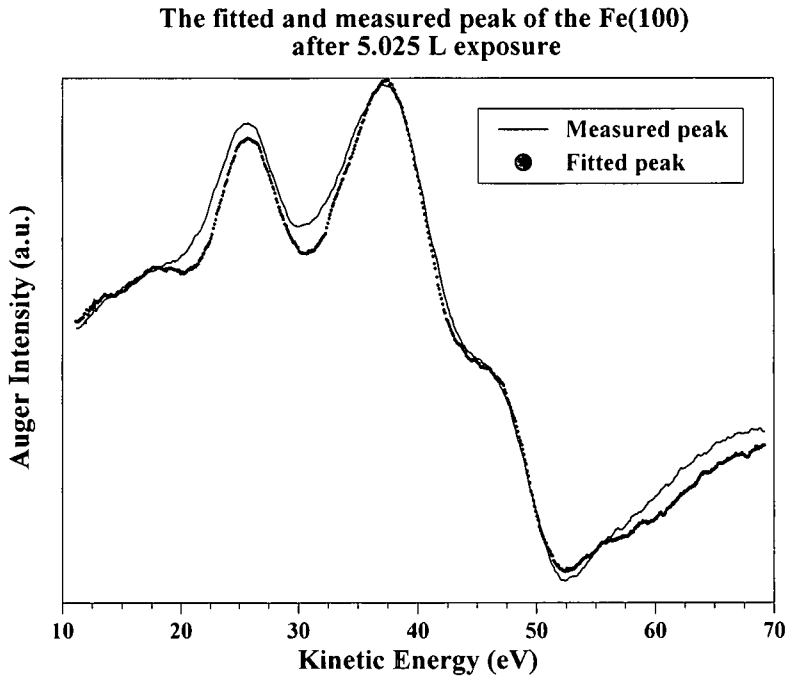

Figure 6.2: The measured and fitted peak for the Fe(100) sample after 5.025 L exposure.

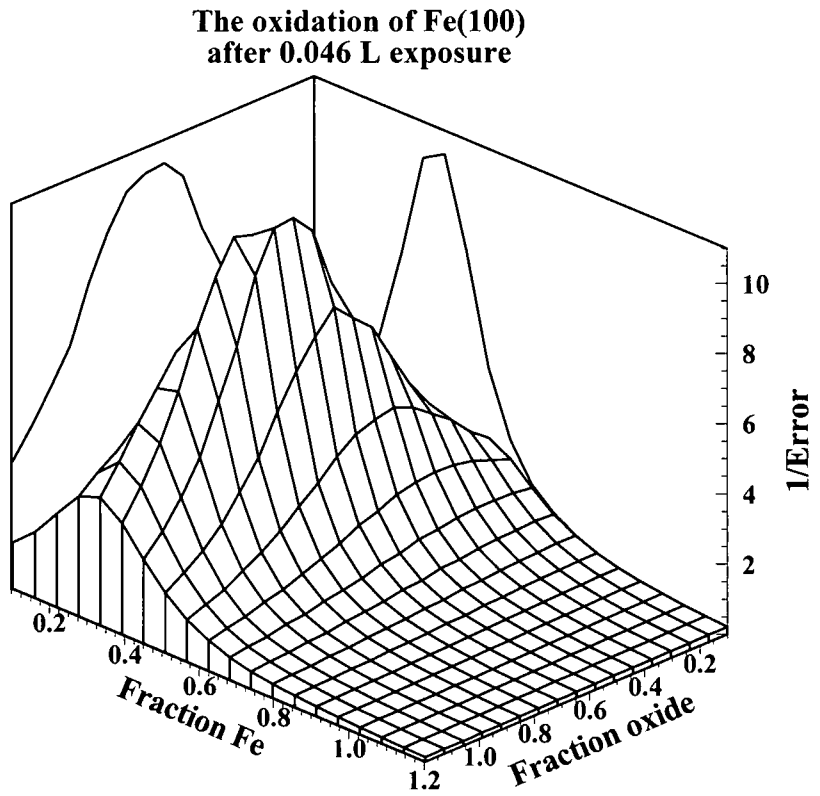

Figure 6.3: The various combinations of the standards and the error in the combinations for the Fe(100) oxidation after 0.046 L exposure. The combination resulting in the smallest error is used for the fits.

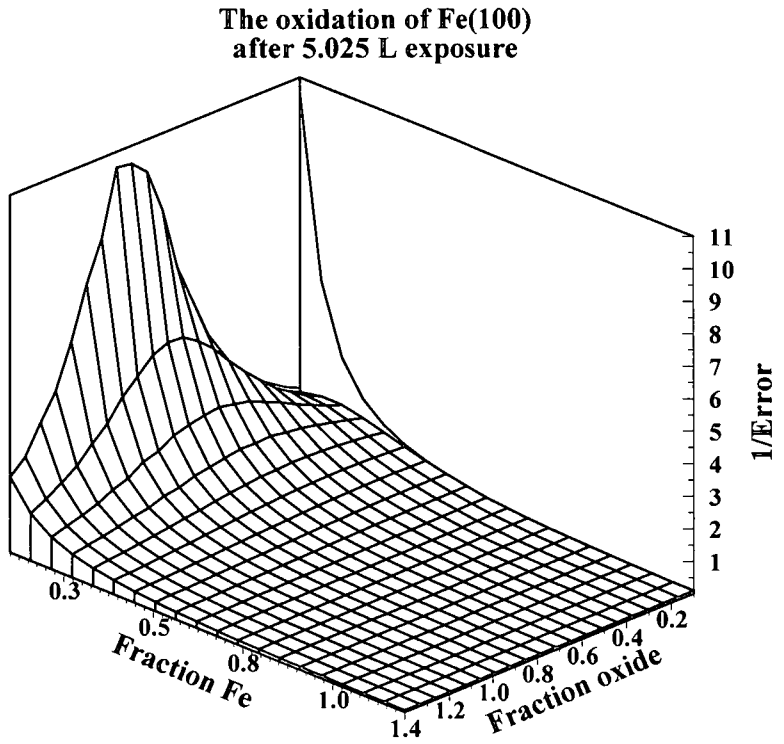

Figure 6.4: The various combinations of the standards and the error in the combinations for the Fe(100) oxidation after 5.025 L exposure. The combination resulting in the smallest error is used for the fits.

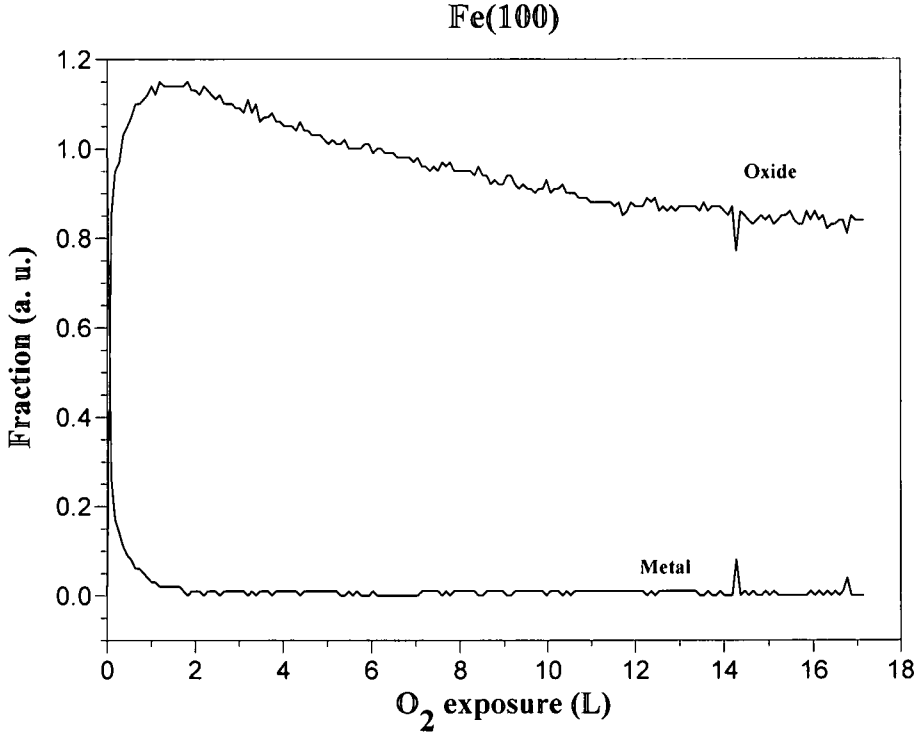

Figure 6.5: The fraction oxide and metal as a function of the oxygen exposure time as calculated using the linear least squares method.

6.2.2. Fe(100)-3.5wt% Mo-N

The fraction oxide and metal contributing to the measured peak for the oxygen exposure of the Fe(100)-3.5 wt% Mo-N specimen is performed in the same way as for the Fe(100) specimen. Again the linear least squares method is applied to determine the combination of oxide and metal that will fit the measured peak with the smallest error. The measured and fitted peaks for the 0.32 L, 0.81 L and 6.57 L exposures is illustrated in Figure 6.6, Figure 6.7 and Figure 6.8. The errors for these three fits are illustrated in Figure 6.9, Figure 6.10 and Figure 6.11. Again, it is clear that there is a unique combination of the standards that have the smallest error and thus is the best fit of the measured peak. The linear least squares method can be applied to all the peaks measured during the oxygen exposure to give the oxide formation as a function of the exposure time. Figure 6.12 illustrates the oxide formation as a function of the exposure time.

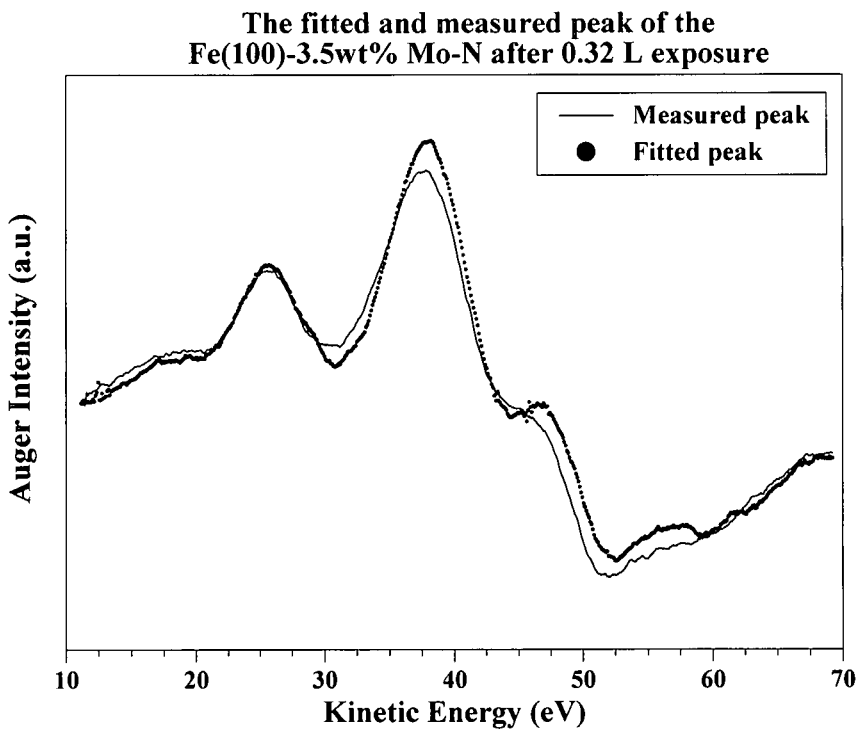

Figure 6.6: The measured and fitted low energy AES Fe peak for the Fe(100)-3.5wt% Mo-N oxidation after 0.32 L exposure.

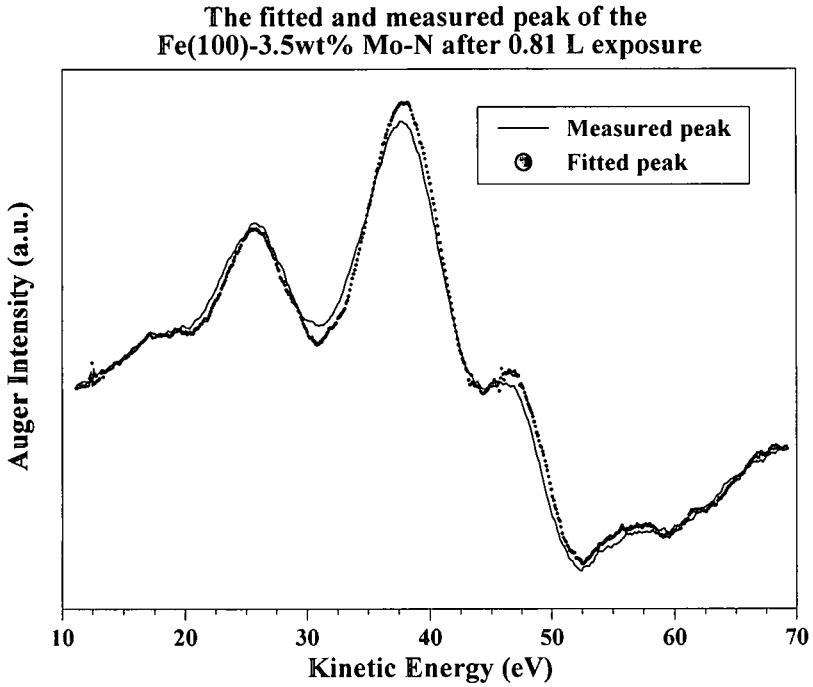

Figure 6.7: The measured and fitted low energy AES Fe peak for the Fe(100)-3.5wt% Mo-N oxidation after 0.81 L exposure.

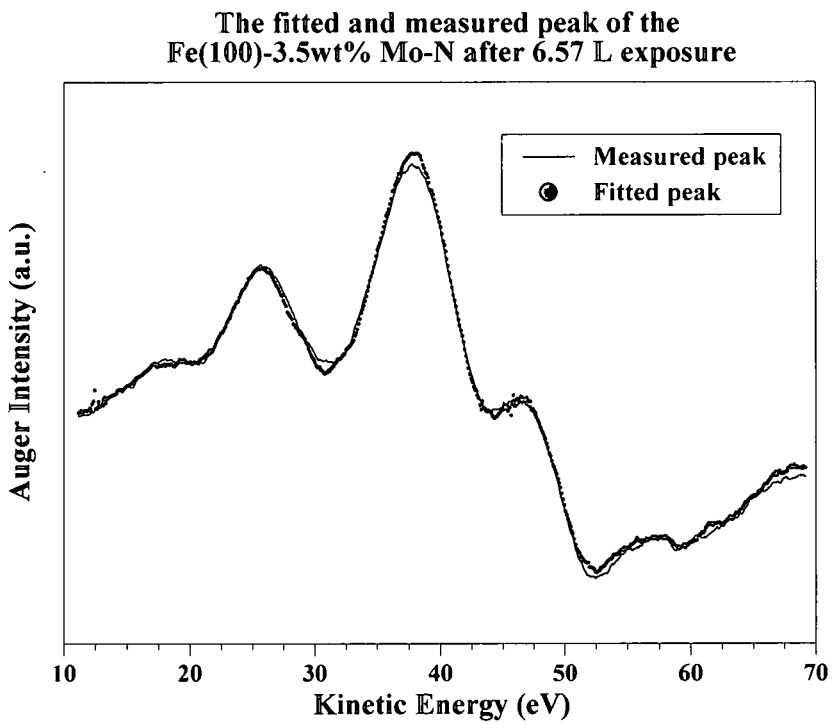

Figure 6.8: The measured and fitted low energy AES Fe peak for the Fe(100)-3.5wt% Mo-N oxidation after 6.57 L exposure.

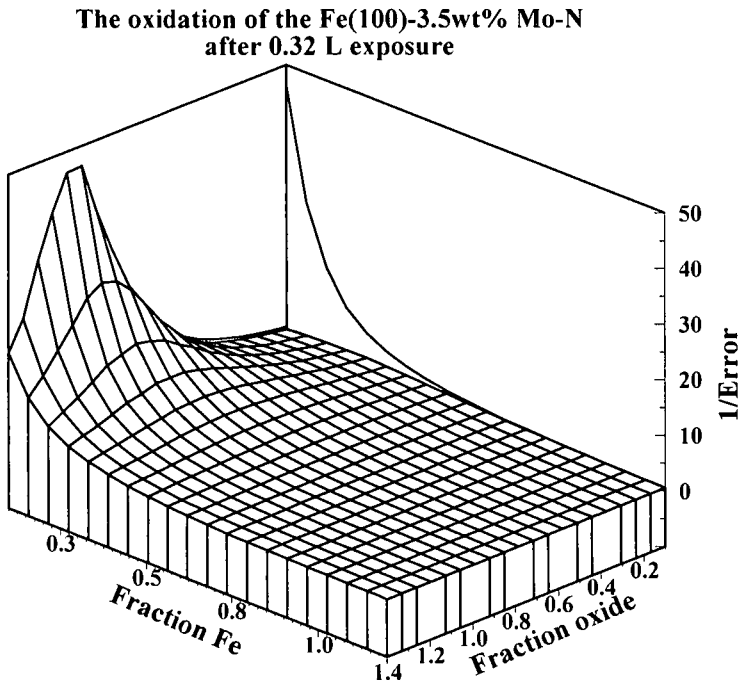

Figure 6.9: The various combinations of the standards and the error in the combinations for the Fe(100)-3.5wt% Mo-N oxidation after 0.32 L exposure. The combination resulting in the smallest error is used for the fits.

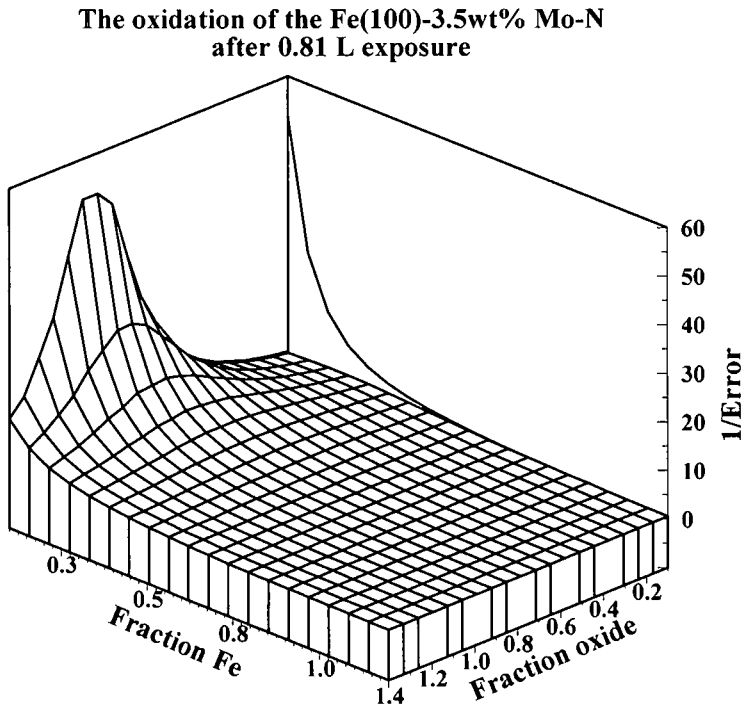

Figure 6.10: The various combinations of the standards and the error in the combinations for the Fe(100)-3.5wt% Mo-N oxidation after 0.81 L exposure. The combination resulting in the smallest error is used for the fits.

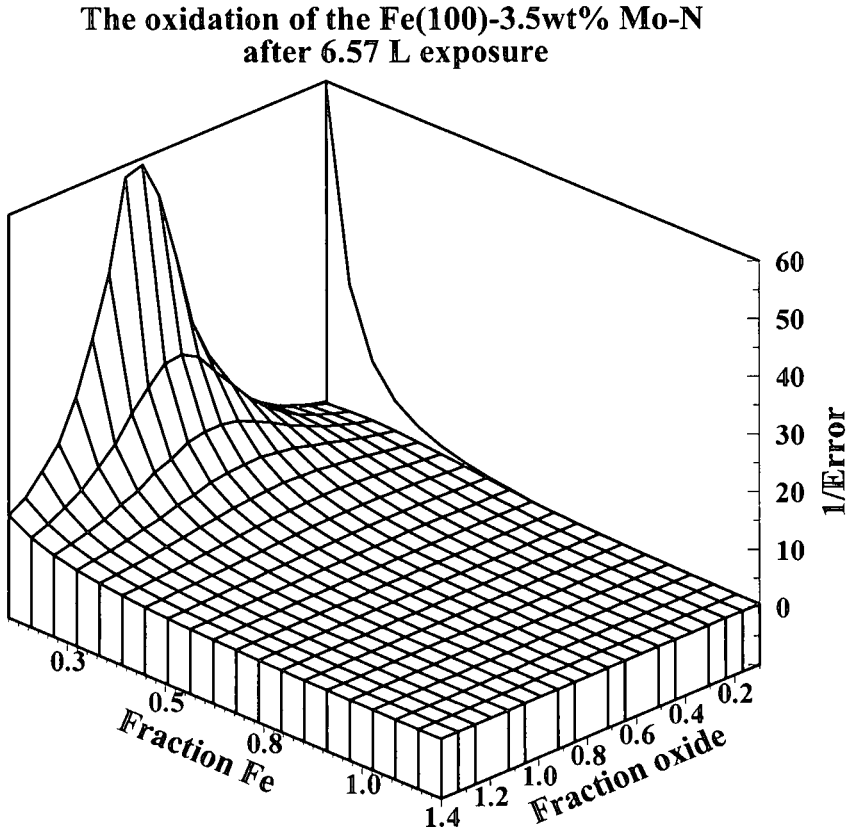

Figure 6.11: The various combinations of the standards and the error in the combinations for the Fe(100)-3.5wt% Mo-N oxidation after 6.57 L exposure. The combination resulting in the smallest error is used for the fits.

6.2.3. Segregated MoN layer on the Fe(100)-3.5wt% Mo-N

The linear least squares method, as applied for the previous specimens, was used to determine the fraction metal and oxide as a function of the oxygen exposure time for the oxygen exposure of the segregated MoN layer on the Fe(100)-3.5wt%Mo-N specimen. The measured and fitted peaks for the 0.32 L, 1.66 L and the 6.60 L exposures are illustrated in Figure 6.13, Figure 6.14 and Figure 6.15.

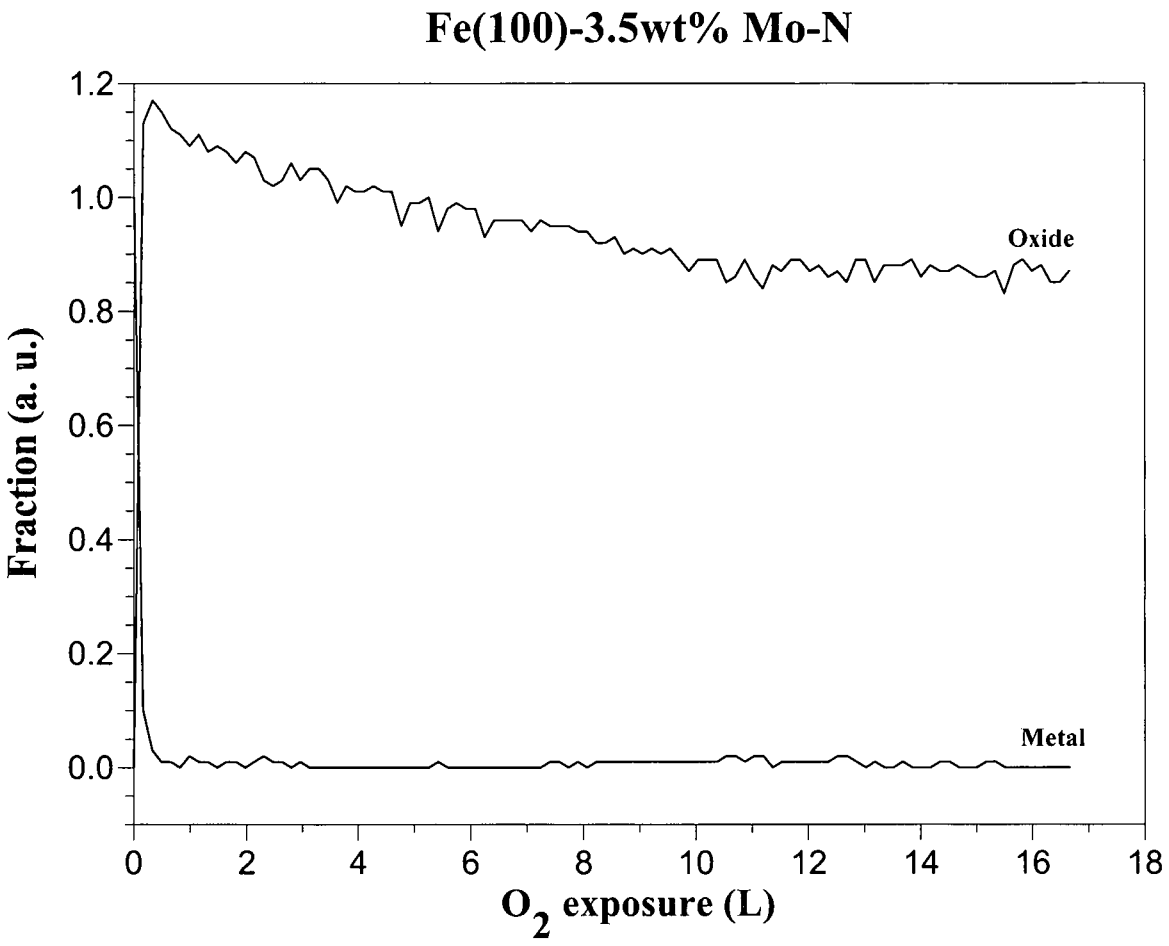

Figure 6.12: The fraction metal and oxide as a function of the exposure time calculated using the linear least squares method for the oxygen exposure of the Fe(100)-3.5wt%Mo-N specimen

The errors for these three fits are illustrated in Figure 6.16, Figure 6.17 and Figure 6.18. Again, it is clear that there is a unique combination of the standards that have the smallest error and thus is the best fit of the measured peak. Applying the linear least squares method to all the low energy Fe peaks measured during the oxygen exposure will give the fraction oxide and metal as a function of the exposure time. These results are illustrated in Figure 6.19.

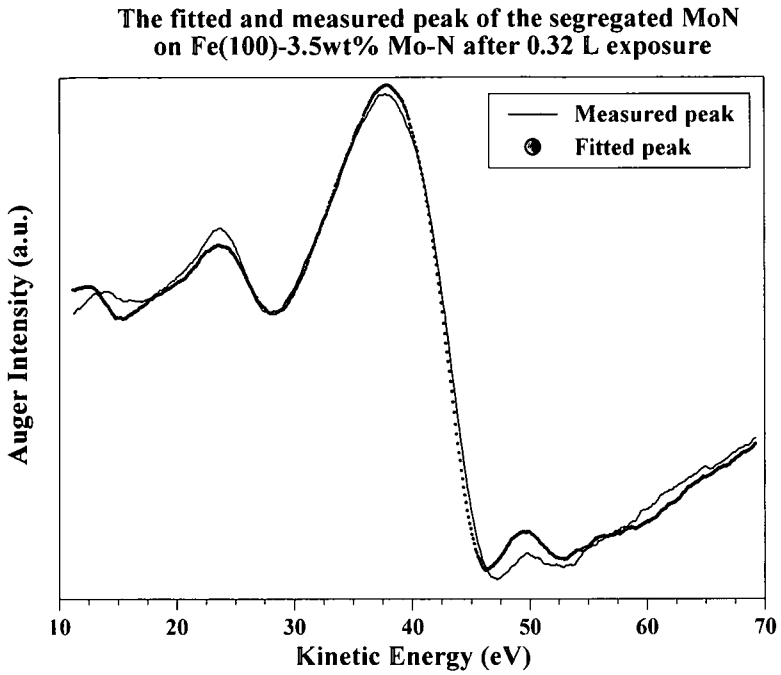

Figure 6.13: The measured and fitted low energy AES Fe peak for the oxidation of the segregated MoN layer on the Fe(100)-3.5wt% Mo-N oxidation after 0.32 L exposure.

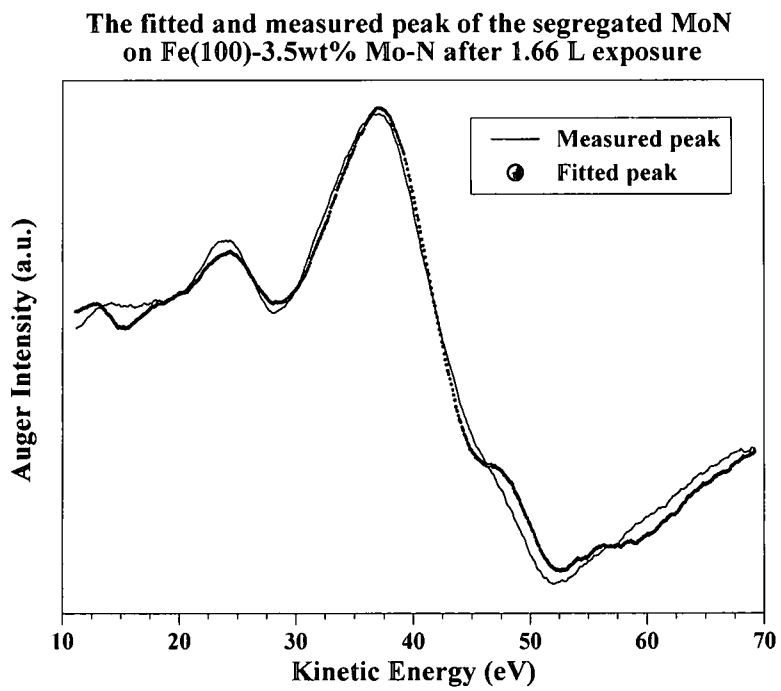

Figure 6.14: The measured and fitted low energy AES Fe peak for the oxidation of the segregated MoN layer on the Fe(100)-3.5wt% Mo-N oxidation after 1.66 L exposure.

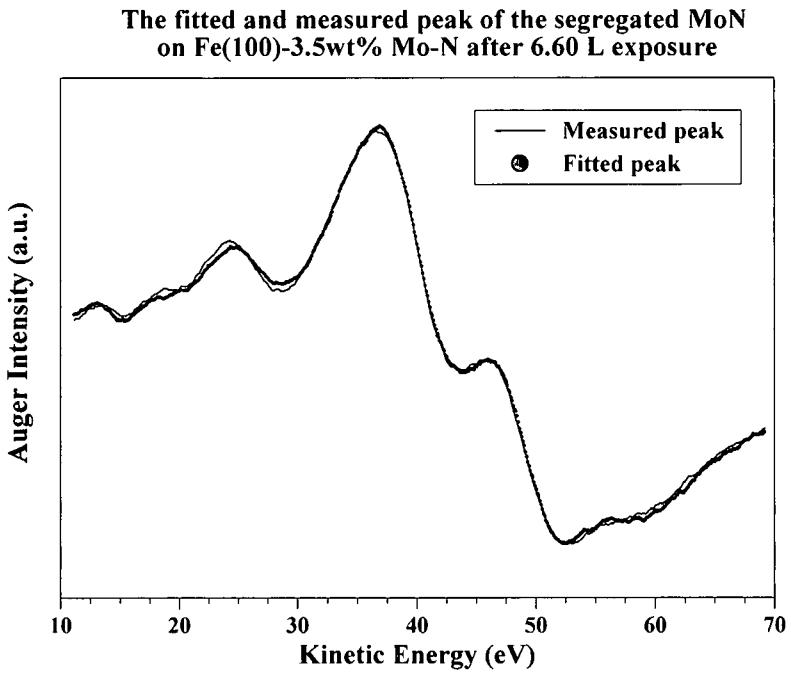

Figure 6.15: The measured and fitted low energy AES Fe peak for the oxidation of the segregated MoN layer on the Fe(100)-3.5wt% Mo-N oxidation after 6.60 L exposure.

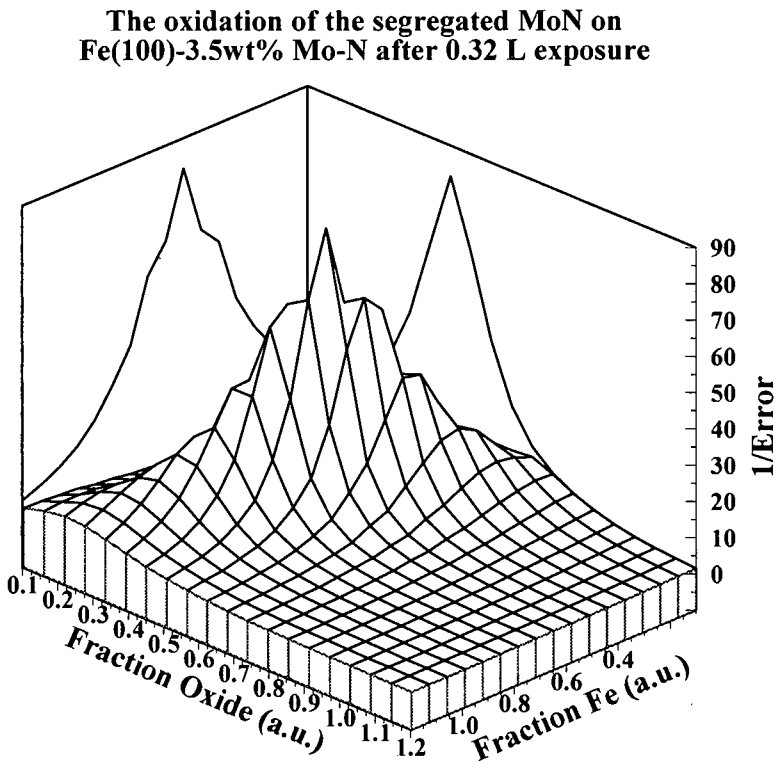

Figure 6.16: The various combinations of the standards and the error in the combinations for the oxidation of the segregated MoN layer on the Fe(100)-3.5wt% Mo-N after 0.32 L exposure. The combination resulting in the smallest error is used for the fits.

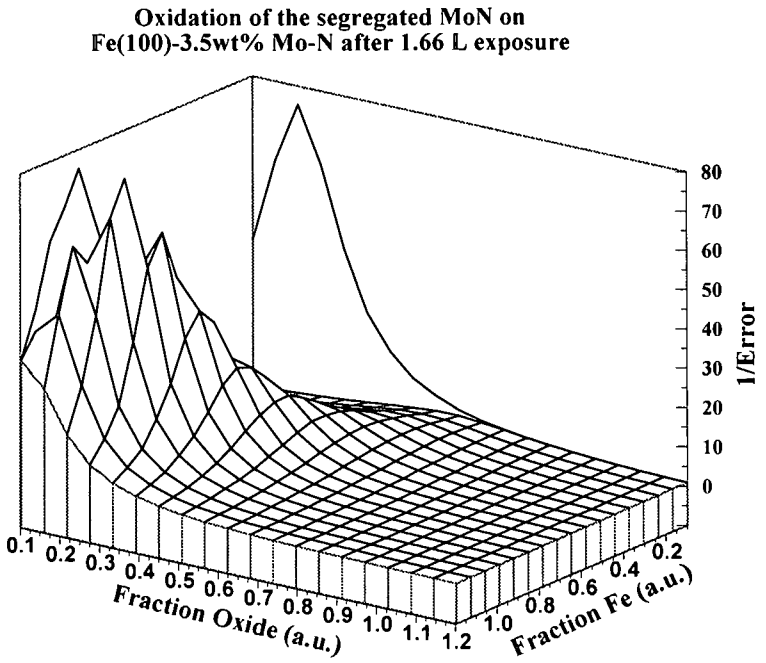

Figure 6.17: The various combinations of the standards and the error in the combinations for the oxidation of the segregated MoN layer on the Fe(100)-3.5wt% Mo-N after 1.66 L exposure. The combination resulting in the smallest error is used for the fits.

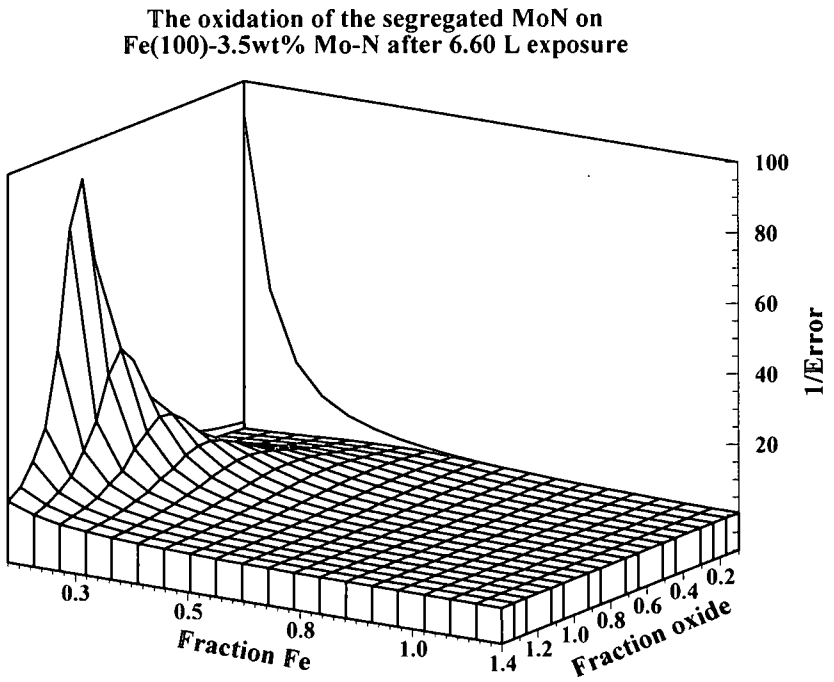

Figure 6.18: The various combinations of the standards and the error in the combinations for the oxidation of the segregated MoN layer on the Fe(100)-3.5wt% Mo-N after 6.60 L exposure. The combination resulting in the smallest error is used for the fits.

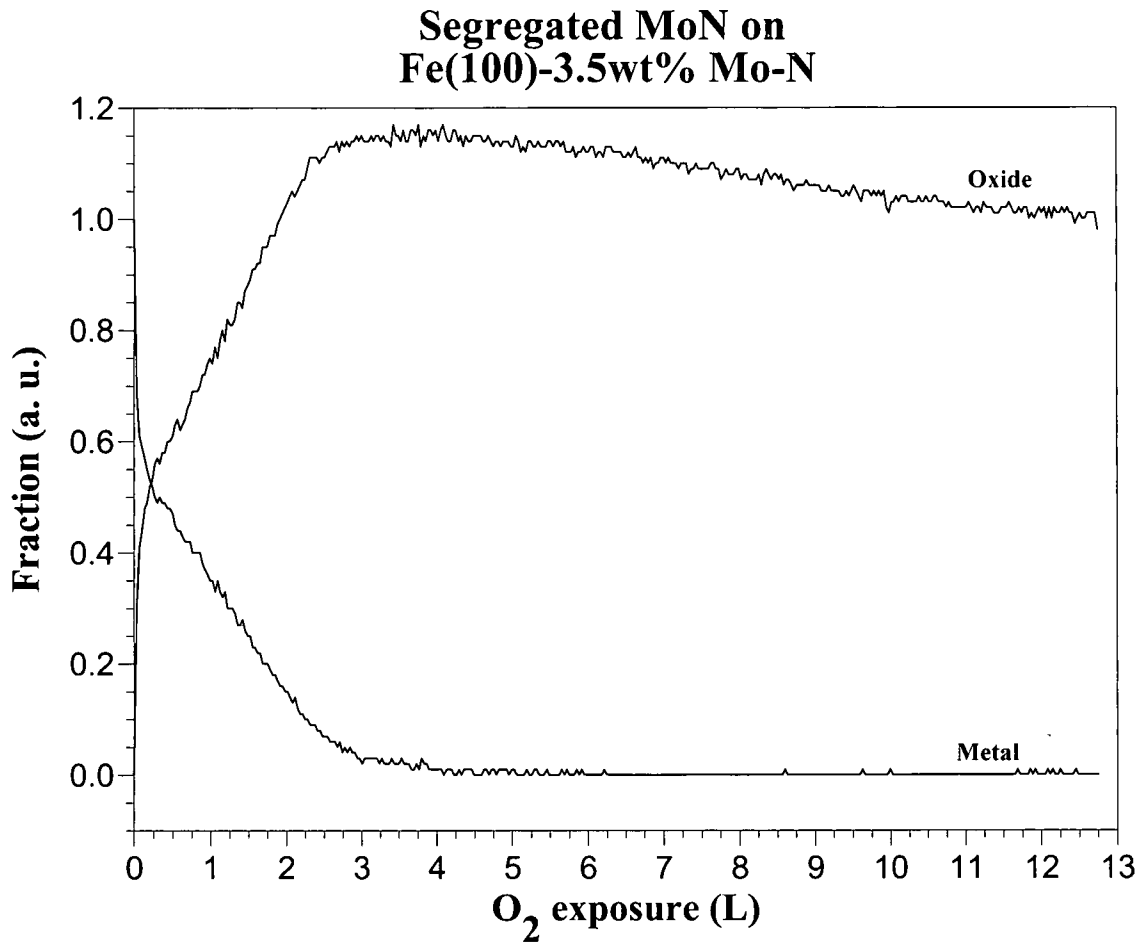

Figure 6.19: The fraction metal and oxide as a function of the oxygen exposure time calculated using the linear least squares method for the oxygen exposure of the segregated MoN layer on the Fe(100)-3.5wt% Mo-N specimen.

6.2.4. Comparison

Comparing Figure 6.5, 6.12 and 6.19, it is clear that the Fe(100) and Fe(100)-3.5wt%Mo-N specimens show similar oxidation behaviour. The maximum fraction oxide for the Fe(100) specimen is 1.15 and for the Fe(100)-3.5wt%Mo-N it is 1.18. The difference is within an acceptable experimental error. The oxide formation for the segregated layer on the Fe(100)-3.5wt%Mo-N specimen is clearly different compared to the Fe(100) and Fe(100)-3.5wt%Mo-N specimens. Although the behaviour differs the maximum fraction oxide for the segregated layer on the Fe(100)-3.5wt%Mo-N specimen is also 1.15.

Another similarity for all three the specimens is the slow decline in the oxide fraction for high exposures. This decline will be discussed in the following paragraph as it influences the thickness calculations.

6.3. Thickness calculations

It has been shown in chapter 4 that the oxide thickness can be calculated using the change in the relative AES peak intensities. From Figure 4.2 it is clear that the fraction oxide increases with an increase in the overlayer thickness. Theoretically, the fraction oxide reaches a maximum value at a certain overlayer thickness and will remain constant with further increase in the overlayer thickness. Keeping the calculations from chapter 4 in mind, consider the experimental results.

6.3.1. Segregated MoN layer on Fe(100)-3.5wt% Mo-N

When applying equation 4.23 on the experimental results for the low energy AES Fe peak and assuming that the backscattering value is constant gives unrealistic results. The calculated values indicate a decline in the oxide thickness with an increase in the exposure. It is, however, expected that the oxide layer will increase in thickness with an increase in the exposure. Figure 6.20 shows the calculated oxide thickness for the oxygen exposure of the segregated layer on the Fe(100)-3.5wt%Mo-N specimen using equation 4.23 and assuming the backscattering to be constant.

Initially the increase of the oxide layer with exposure is expected, but the decrease in the oxide thickness at high exposures is illogical. The behaviour of the iron oxide Auger peak intensity is influenced by the backscattering term. Thus, for a higher backscattering term the peak intensity will be higher and obviously then for a lower backscattering term the peak intensity will be lower. The composition of the oxide and the substrate vary and thus the backscattering term associated with the oxide and the substrate will also differ.

Consequently, as the oxide overlayer thickens the contribution of the oxide's backscattering to the total backscattering will increase. Because the backscattering of the oxide is less than the backscattering of the substrate the peak intensity will decrease at high exposures. The decrease observed in Figure 5.30 is thus not due to a change in the experimental conditions but as a result of the change in the backscattering.

In order to compensate for the change in the backscattering term in the calculation of the overlayer thickness it is necessary to take the following into account:

- At zero oxide thickness the backscattering is due to the substrate, thus $R=R_{Fe}$
- For an infinitely thick oxide layer the backscattering is due to the oxide, thus $R=R_{Ox}$

To incorporate the change in the backscattering assume, for a first approximation, that the change in the backscattering to be linear with the exposure time, thus:

$$R(t) = kt + R_{Fe} \tag{6.1}$$

and

$$k = \frac{(R_{Ox} - R_{Fe})}{t`} \tag{6.2}$$

where t' is the exposure time where the last AES peak was measured, and $R(t)$ is the total backscattering.

Applying this correction to the backscattering term in the calculation for the oxide thickness gives more realistic results, as illustrated in Figure 6.21. The correction for the backscattering term, although it is a first approximation is clearly a step in the right direction. In Figure 6.21 the oxide thickness increases, as expected, with an increase in the exposure time.

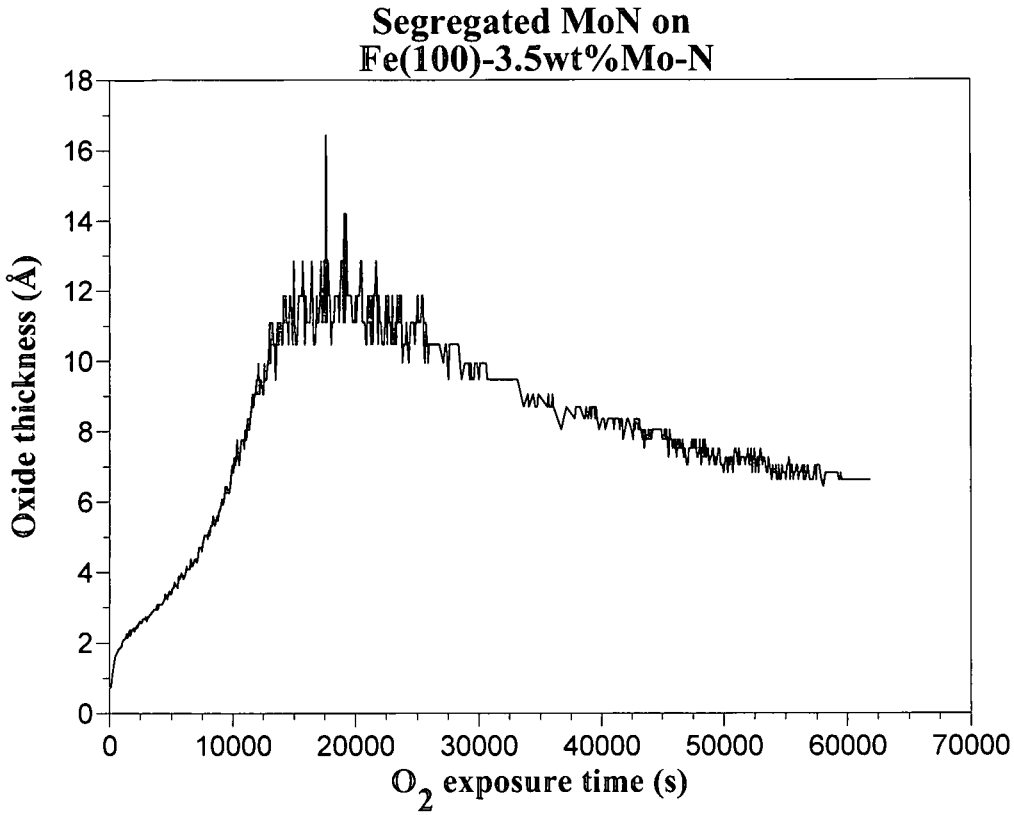

Figure 6.20: The calculated oxide thickness for the oxygen exposure of the segregated MoN layer on the Fe(100)-3.5wt% Mo-N specimen assuming that the backscattering is constant.

The thickness of the overlayer, or in this case the oxide, can also be calculated from the change in the intensity of the high energy AES Fe peak. When using equation 4.21 for the calculation of the oxide thickness, it is assumed that the intensity of the high energy Fe peak is due to the substrate. Since there is also a contribution to this peak from the Fe in the oxide layer the calculations are expected to show an overcompensation for the oxide thickness. Figure 6.22 illustrates the oxide thickness calculated from the high energy Fe peak. Comparing the thickness of the oxide from Figure 6.21 and Figure 6.22, it is clear that the rate of increase above 4 L is the same, but that the thickness after 12 L differs. The calculated oxide thickness using the high energy Fe peak is higher compared to the calculated oxide thickness using the low energy Fe peak with the corrected backscattering. The expected overcompensation is thus confirmed.

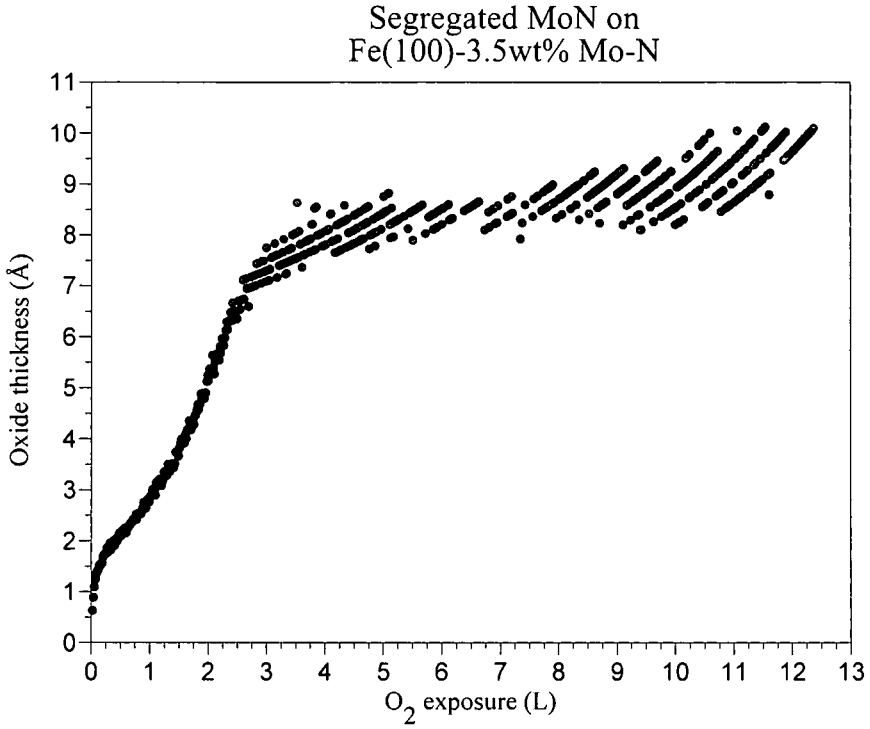

Figure 6.21: The oxide thickness calculated with the backscattering correction for the oxygen exposure of the segregated MoN layer on the Fe(100)-3.5wt% Mo-N specimen.

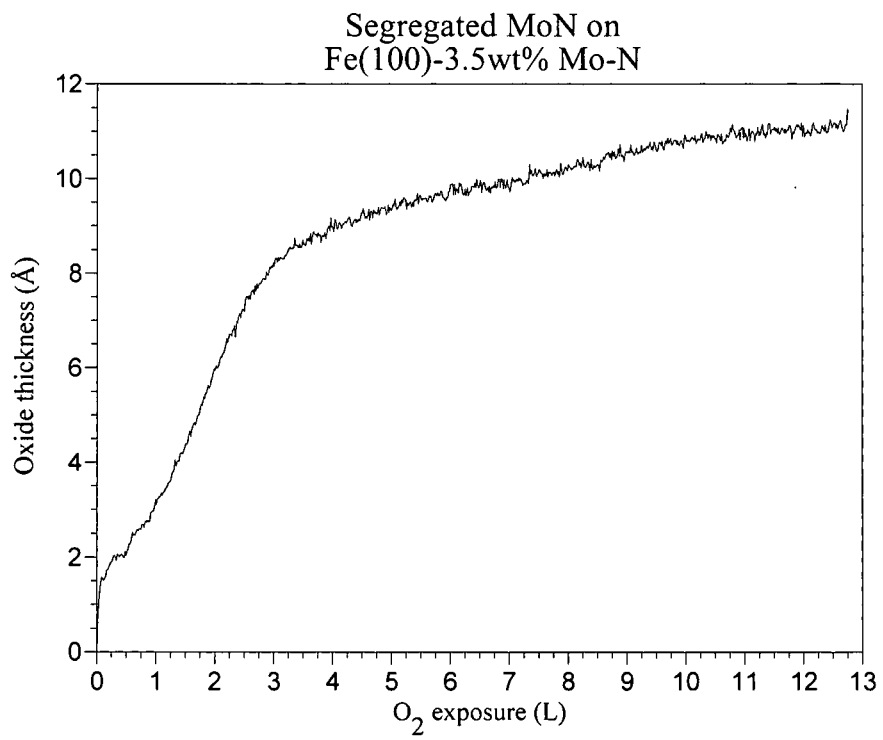

Figure 6.22: The oxide thickness calculated using the high energy Fe peak.

6.3.2. Fe(100)-3.5wt% Mo-N

The oxide thickness calculation for the alloy was more complicated than for the segregated layer. As seen in Figure 6.12 the oxide fraction shows a decline at higher oxygen exposures. The decline, as for the previous section, is attributed to the change in the backscattering term with exposure time. In this case, however, the change in the backscattering term was not linear.

The thickness can also be calculated from the change in the high energy Fe AES peak intensity using equation 4.21 where the calculations are independent from the backscattering term. The calculated oxide thickness using this equation is illustrated in Figure 6.23. The thickness calculations from the change in the low energy Fe AES peak shape is dependent on the backscattering terms, as shown in the previous sections. The change in the backscattering terms for this specimen does not show a linear trend, but an exponential change. The change in the backscattering terms are more thus complicated and the first approximation can not be applied.

From these preliminary thickness values the backscattering term can be investigated using equation 4.23. With the oxide thickness known and the R_{Ox} equal to 1.63, from the calculations in chapter 4, equation 4.23 can be re-written to give the R_{Fe} value as a function of the exposure time. As for the exposure of the segregated MoN layer the R_{Fe} value in the equation is replaced by $R(t)$. Figure 6.24 illustrates the change in the backscattering term, $R(t)$, as a function of the exposure time.

The R_{Fe} value, from Figure 6.24, is equal to 2.31. The deviation of this value from the calculated value in chapter 4 is attributed to the crystal orientation and the sensitivity of the backscattering term to the incident angle of the primary electrons. From Figure 6.24 it is clear that the change in the backscattering term is not linear. The first approximation used for the thickness calculations of the oxide on the segregated MoN layer can clearly

not be applied for the calculation of the oxide thickness on the Fe(100)-3.5wt% Mo-N specimen. The calculation using the high energy Fe AES peak will therefore be used for further calculations. It is accepted that the overcompensation for the thickness is within an acceptable degree of error.

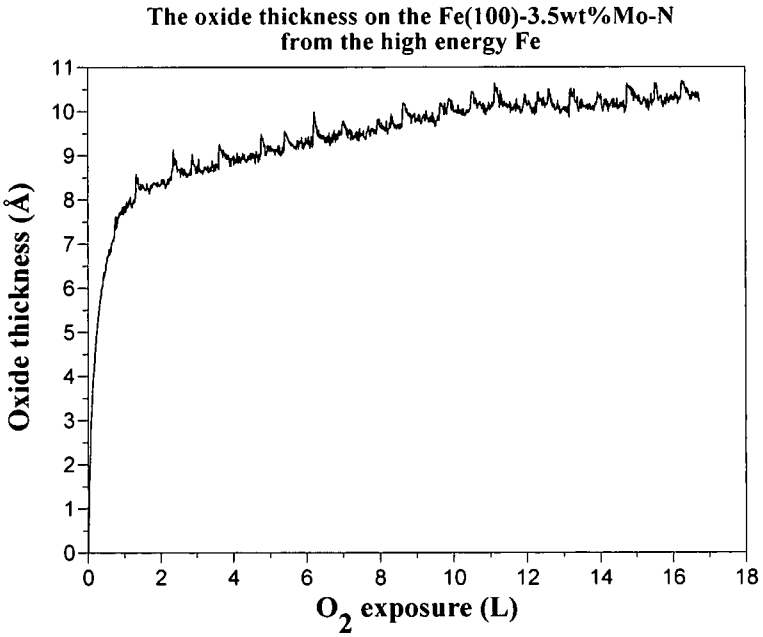

Figure 6.23: The oxide thickness formed on the Fe(100)-3.5wt% Mo-N specimen calculated from the change in the high energy Fe AES peak.

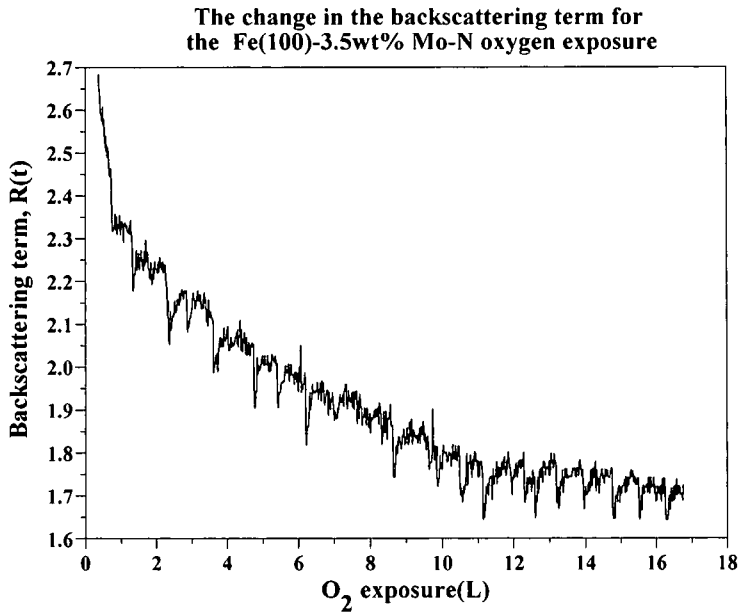

Figure 6.24: The backscattering term as a function of the exposure time.

6.3.3. Fe(100)

The oxide thickness illustrated in Figure 6.5 shows the same decline as for the previous two samples and it is accepted that the decline is also as a result of the changing backscattering term. Similarly to the Fe(100)-3.5wt% Mo-N specimen the backscattering term for the Fe(100) specimen also showed non linear decline. Once again equation 4.21 can be used to calculate the oxide thickness from the change in high energy Fe AES peak intensity. The calculated thickness values are illustrated in Figure 6.25.

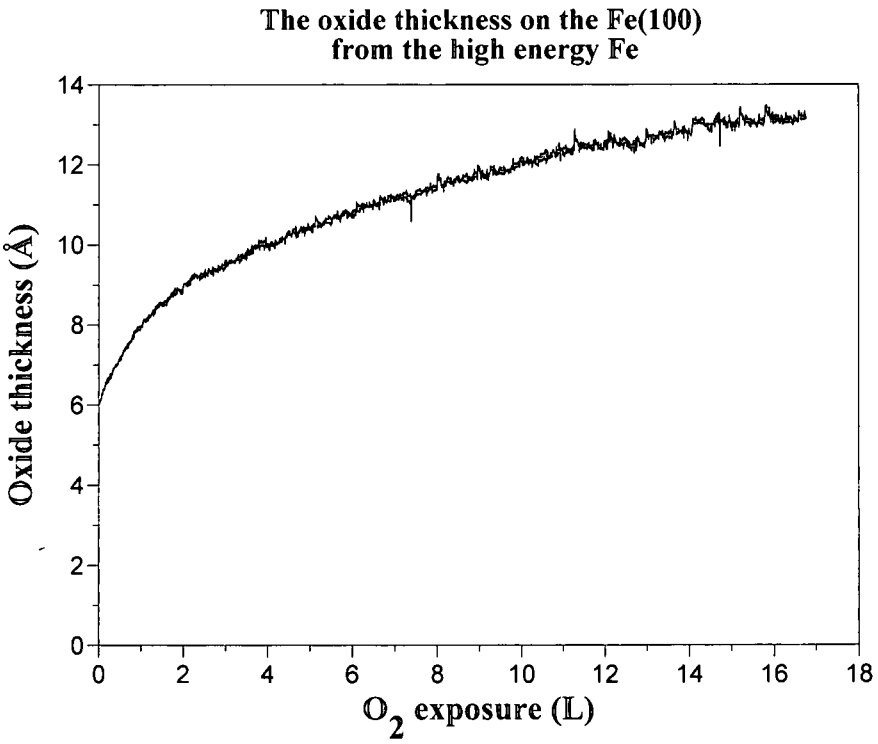

Figure 6.25: The calculated oxide thickness on the Fe(100) specimen from the high energy Fe AES peak.

The calculated oxide thickness values are used to investigate the decline of the backscattering values in the same way as for the Fe(100)-3.5wt% Mo-N specimen. Using the same method as described in the previous section the *R(t)* values are calculated and illustrated in Figure 6.26.

The R_{Fe} from Figure 6.26 is equal to 2.79. Again the deviation from the calculated value in chapter 4 is attributed to the crystal orientation and angle of incidence of the primary electrons. From Figure 6.26 it is also clear that the backscattering term does not decline linearly and therefore the thickness calculations illustrated in Figure 6.25 are used for further calculations.

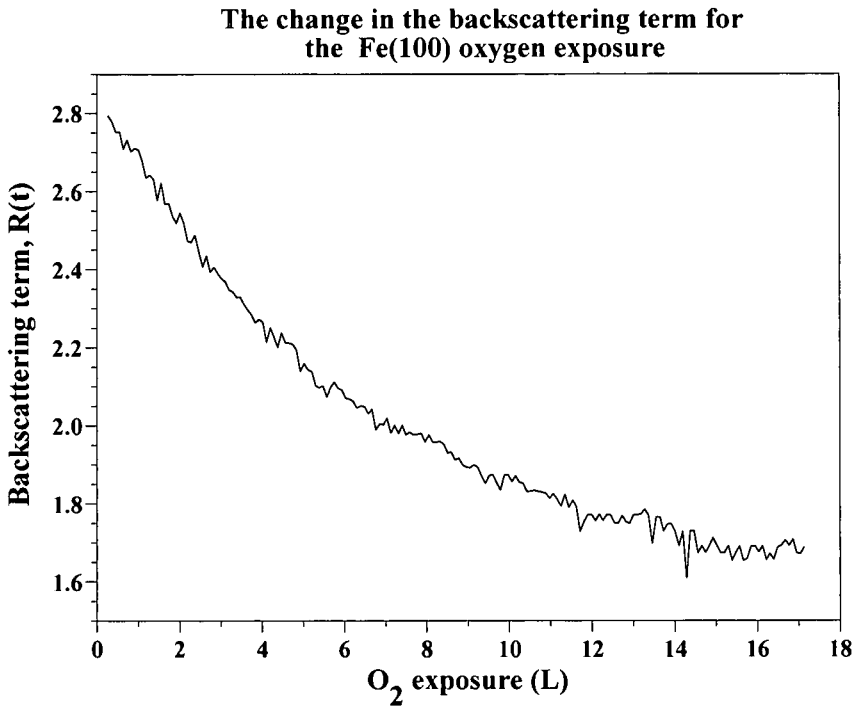

Figure 6.26: The backscattering term, *R(t)*, as a function of the exposure time.

6.4. The sticking coefficient

It has been shown in chapter 2 that the sticking coefficient is a function of the surface coverage. The surface coverage is proportional to the O APPH values. The sticking coefficient will therefore change with the exposure time. The rate at which the O APPH values increase as a function of the exposure time is therefore an indication of the change in the sticking coefficient. Figure 6.27 illustrates the change in the relative sticking coefficient with the O_2 exposure time for the room temperature O_2 exposure of the segregated MoN layer on the Fe(100)-3.5wt% Mo-N specimen and for the room temperature O_2 exposure of the Fe(100) specimen.

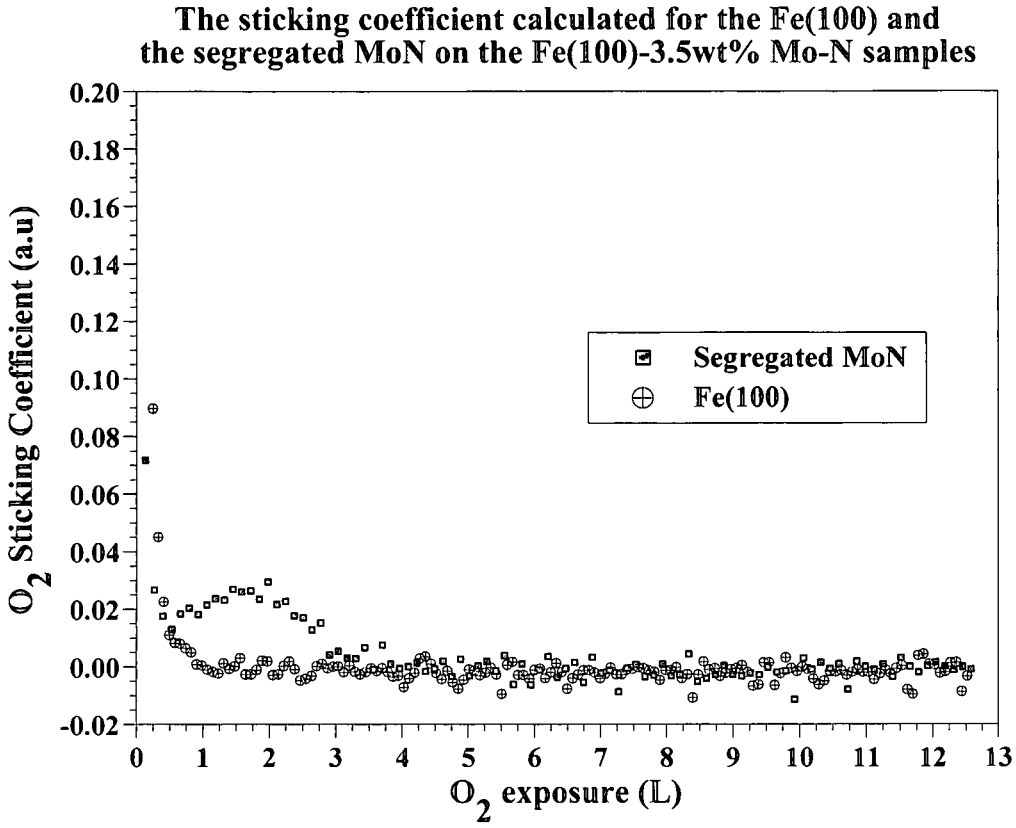

Figure 6.27: The oxygen sticking coefficient calculated for the Fe(100) specimen and the segregated MoN on the Fe(100)-3.5wt% Mo-N samples.

There is a clear difference in the change of the sticking coefficient for the two specimens. The increase in the sticking coefficient in Figure 6.27 is attributed to the effect of the dissociation and desorption of the MoN layer on the adsorption of the oxygen.

6.5. Summary

In this chapter the experimental results for the room temperature oxygen exposures, that were presented and discussed in chapter 5, were analysed using the calculations discussed in chapter 4. The linear least squares method was successfully applied to the low energy Fe AES peaks to obtain the fraction metal and oxide as a function of the exposure time. It was shown that equation 4.23 is only applicable for low oxide coverage as the backscattering term is also a function of the exposure time. A first approximation was proposed to incorporate the change in the backscattering with time to the thickness

calculations. Although the first approximation worked well for the oxide formation on the segregated MoN layer the decline in the backscattering terms for the Fe(100)-3.5wt% Mo-N and Fe(100) specimens were not linear, and therefore the proposed correction could not be applied. The oxide thicknesses were calculated using equation 4.21.

The O APPH values as functions of the oxygen exposure time were used to investigate the change in the oxygen sticking coefficient as a function of the oxygen exposure time. There was a clear difference in the oxygen sticking coefficients between the Fe(100) specimen and the segregated MoN layer on the Fe(100)-3.5wt% Mo-N specimen.

Chapter 7

Summary and Conclusions

7.1. Summary

The aim of this study was to investigate the oxidation behaviour of a segregated MoN layer on an Fe(100)-3.5wt% Mo-N specimen. The segregation of the Mo and N to the surface of the sample resulted in the formation of a MoN surface layer. It was shown that the surface layer was, in agreement with other studies, not Mo_2N but indeed MoN.

It was shown that the alloy elements in the Fe(100)-3.5wt% Mo-N had virtually no influence on the oxidation behaviour of the Fe(100), although the inter-diffusion coefficients differ. For both these specimens there was oxide formation up to 200°C and no oxide formation detected above 300°C.

For the room temperature exposures there were striking differences in the oxidation behaviour of the segregated MoN layer compared to the other specimens. The hypothesis formulated suggested the dissociation of the MoN layer and the formation of volatile MoO_3 and N_xO_y compounds. After the oxidation of the MoN layer there was no Mo or N enrichment detected underneath the oxide layer and the oxide formed on the surface was iron oxide.

The low energy Fe AES peak shape changed upon oxide formation. These changes were used to calculate the fraction oxide and metal as functions of the exposure time by utilising the linear least squares method. The thickness of the oxide layer can be calculated from the fraction oxide or from the change in the intensity of the high energy

Fe AES peaks. The former is dependent upon the backscattering terms. It was shown that the backscattering terms were not constant but were also functions of the exposure time. A first approximation suggested that there was a linear decrease in the backscattering term. This approximation did however not apply to all the samples. The thickness calculations using the high energy Fe AES peaks resulted in overcompensated values as there was some Fe in the oxide layer that also contributed to the peak intensity.

The oxygen sticking coefficient was also calculated from the rate of change of the O APPH with the exposure time. There were no differences in the calculated oxygen sticking coefficient values for the Fe(100) and Fe(100)-3.5wt% Mo-N samples. There was a distinct difference for the oxygen sticking coefficient for the segregated MoN layer compared to the values calculated for the other specimens.

This study clearly indicates the importance of the surface of the specimens in the oxidation process. Relatively small disturbances or changes of the surface can markedly alter the properties of the specimens.

7.2. Future work

There are a number of other surface study techniques that could be used to build a more complete model of the oxidation behaviour of the segregated MoN layer.

- X-ray photoelectron spectroscopy (XPS) studies would confirm the chemical composition of the MoN layer and the oxide that forms on the sample surface
- Ion scattering spectroscopy is a more surface sensitive technique and can be used to monitor the topmost surface layers. This technique can therefore be applied to monitor the segregation, dissociation and oxidation that occur on the sample surface.

- A scanning tunnelling microscope can also be used to trace the surface reactions and would prove especially useful for monitoring the retarded oxidation of the segregated MoN layer.

Apart from these experimental techniques there is also some theoretical work to be done. It was shown that the backscattering term for the single crystals varies somewhat from the calculated values. The empirical formulae used, had been formulated for polycrystalline specimens with a 30° incident primary electron beam. There are still no empirical formulae for the single crystals of various orientations. There is also a change in the backscattering term with the exposure time that requires some investigation.

7.3. Research presentations

The research project has been presented at several conferences, both national and international. The various presentations are listed here.

1. R. Conradie, H.C. Swart and E.C. Viljoen, *An Oxidation Study of a Segregated MoN Surface Layer*, South African Institute of Physics, Port Elizabeth, South Africa, 1999.
2. R. Conradie, H.C. Swart and E.C. Viljoen, *Segregation Engineering: The Catalytic Properties of a stable MoN Layer*, Second International Workshop on Surface and Grain Boundary Segregation, Rottach-Egern, Germany, 1999.
3. R. Conradie, G.N. van Wyk, H.C. Swart and E.C. Viljoen, *The Initial Oxidation of a Segregated MoN-layer on a Fe(100)3.5% Mo substrate*, ECOSS, Vienna, Austria, 1999.
4. R. Conradie, H.C. Swart and W.D. Roos, *Room Temperature Oxidation of Segregated Mo and N on an Fe(100)-3.5wt% Mo-N Specimen* , South African Institute of Physics, Durban, South Africa, 2001.

5. R. Conradie, H.C. Swart and W.D. Roos, *Determining the thickness of an oxide layer on Fe(100)-Mo-N using Auger electron spectroscopy*, South African Institute of Physics, Durban, South Africa, 2001.

Bibliography

1. Viljoen, E.C. and Uebing, C., Surface Science, 1998, **410**, 123
2. Eltester, B. and Uebing, C., Surface Science, 1996, **347**, 39
3. Baraldi, A., Brena, B., Comelli, G., Lizzit, S., Paolucci, G., Baumann, P.,Scheuch, V. and Uebing, C., Vacuum, 1997, **48**, 3, 351
4. Viljoen, E., Jordaan, W.A., Uebing, C. and du Plessis, J., Materials Science Forum, 1999, **294-296**, 461
5. Hille, V.,Viljoen, E.C. and Uebing, C., Surface Science, 1997, **388**, L1092
6. Roberson, S.L., Finello, D. and Davis, R.F., Thin Solid Films, 1998, **324**, 30
7. Mudholkar, M.S. and Thompson, L.T., Journal of Applied Physics, 1995, **77**, 10, 5138
8. Demczyk, B.G., Choi, J.-G. and Thompson, L.T., Applied Surface Science, 1994, **78**, 63
9. Mathieu, H.J. and Landolt, D., Corrosion Science, 1986, **26**, 7, 547
10. Scully, J.C., The Fundamentals of Corrosion, Second Edition, Pergamon Press, Oxford, 1975
11. Hofmann, S. ,Thin Solid Films, 1990, **193/194,** 648
12. Swart, H.C., 'n AES- en RBS-studie van die oksidasie en verstuiwing van yster- en terbiumsilisied, Bloemfontein (1992), Ph.D. Thesis.
13. Little, William, Fowler, H.W., Coulson, J., The shorter Oxford English Dictionary, Third Edition, Oxford University Press, Oxford, 1972.
14. Skoog, Douglas A., West, Donald M. and Holler, F. James, Fundamentals of Analytical Chemistry, Seventh Edition, Saunders College Publishing, Orlando,1996.
15. Gasser, R.P.H., An introduction to chemisorption and catalysis by metals, Clarendon Press, Oxford, 1985.
16. Blakely, J.M., Introduction to the properties of crystal surfaces, Pergamon Press, Oxford, 1973.
17. Benard, J., Adsorption on Metal Surfaces, An integrated approach, Elsevier, Scientific Publishing Company, Amsterdam, 1983.

18. Present, R.D., Kinetic Theory of Gases, McGraw-Hill Book Company, Inc., New York, 1958.
19. Hudson, John B., Surface Science, An introduction, Butterworths-Heinemann, Boston, 1991.
20. Bond, G.C., Heterogeneous Catalysis, Principles and applications, Clarendon Press, Oxford, 1974.
21. Campbell, Ian M., Catalysis at surfaces, Chapman and Hall, Cambridge, 1988.
22. Birks, N. and. Meier, G.H, Introduction to high temperature oxidation of metals, Edward Arnold Publishers Ltd., London, 1983.
23. Omar, M. Ali, Elementary Solid State Physics, Addison Wesley Publishing Company, Inc., Philippines, 1975.
24. Smith, William F., Principles of materials science and engineering, Third Edition, McGraw-Hill, Inc., New York, 1996.
25. Evans, Ulick R., The corrosion and Oxidation of metals, Edward Arnold Ltd.,London, 1960.
26. Massalski, T., Okamoto, H., Subramanian, P.R. and Kacprzak, L., Binary alloy phase diagrams, 2nd Edition, ASM International, 1990.
27. Briggs, D. and Seah, M.P., Practical Surface Analysis, John Wiley & Sons Ltd., Chichester, 1983.
28. Greeff, A.P., Die oksidasie van industriële FeCrMo staal, Bloemfontein (1999), M.Sc. thesis.
29. Terblans, J.J., Die ontwikkeling van 'n sagtewarepakket vir die beheer van en die dataverwerking vanaf 'n skandeeraugermikroskoop, Bloemfontein (1997), M.Sc. thesis.
30. Terblans, J.J., Modellering en eksperimentele ondersoek van Sb-oppervlak segregasie in Cu-enkelkristalle, Bloemfontein (2001), Ph.D. thesis.
31. Powell, C.J., Jablonski, A., Tilinin, I.S., Tanuma, S. and Penn, D.R., Journal of Electron Spectroscopy and Related Phenomena, 1999, **98-99**, 1
32. Shimizu, R., Japanese Journal of Applied Physics, 1983, **22**, 11,1631.
33. Ichimura, S., Shimizu, R. and Langeron, J.P., Surface Science Letters, 1983, **124**, L49
34. Ichimura, S.and Shimizu, R., Surface Science, 1981, **112**, 386

35. Roos, W.D., Optimale benutting van Augerelektronspektroskopie en lae energie ioonverstrooiingsspektroskopie vir die oppervlakkarakterisering van CuNi, PtPd en NiAl allooie, Bloemfontein (1996), Ph.D. thesis.
36. Van Staden, M.J. and le Roux, J.P., Applied Surface Science, 1990, **44**, 263
37. Zhang, C., van Hove, M.A. and Somorjai, G.A., Surface Science, 1985, **149**, 326